

**UTas BE(Hons) Thesis: The Use of Cell
Modelling of Lithium-ion Batteries for
Effective Balancing Control**

Alban. King 180423

June 2020



School of Engineering

*This thesis is submitted in partial fulfilment of the requirements for the degree of
Bachelor of Engineering with Honours, University of Tasmania.*

Declaration

This Thesis to the best of my knowledge and belief contains no material published or unpublished that was written by another person, nor any material that infringes copyright, nor any material that has been accepted for a degree or diploma by University of Tasmania or any other institution, except by way of background information and where due acknowledgement is made in the text of the Thesis.

This Thesis is the result of my own investigations, except where otherwise stated. Other sources are acknowledged in the text giving explicit references. A list of references is appended.

I hereby give consent for my Thesis to be available for photocopying, inter-library loan, electronic access to University of Tasmania staff and students via the University of Tasmania library, and for the title and summary to be made available to outside organisations, in accordance with the Copyright Act 1968.

Signed:

Dated: October 18, 2020

Abstract

Lithium-ion batteries have a dominant market share, due to their favourable characteristics [1]. This project looks at issues with use and management of Lithium-ion batteries, specifically safe operation and cell balancing techniques are investigated. A battery management system was produced with a novel cell measurement circuit and passive cell balancing algorithm. In order to improve the performance of the balancing algorithm, a cell modelling method from the literature was implemented and analysed [2]. This study found that using the cell modelling system improved the balancing algorithm's balancing and charging time by 12.6%. Additionally, to validate the results from the measurement and cell modelling systems, analyses of propagation of uncertainty were conducted. Future work may include broader testing conditions to better understand the positive affect of the cell modelling system on the balancing algorithm.

Acknowledgements

I would like to acknowledge my supervisors Sarah Lyden and Andrew Chan; university technical officers, Simon Hogwood and Jon Rodden; Edward King, Bernadette Welsh and Camilla Uhlbäck, for their assistance and support in completing this work.

Contents

Declaration	i
Abstract	ii
Acknowledgements	iii
Nomenclature	vii
1 Introduction	1
1.1 Project Background	1
1.2 Project Scope and Aims	2
1.3 Layout of the Report	2
2 Literature review	4
2.1 Introduction	4
2.2 Battery Technology	4
2.2.1 Lithium-ion Battery Chemistry	4
2.2.2 Battery Modelling	9
2.2.3 Cell Balancing	11
2.3 Battery Management Systems	14
2.4 Derived quantities	16
2.4.1 Real Time Impedance Estimation	18
2.5 Gaps in the knowledge	21
3 System Design	22
3.1 Design Requirements	22

3.2	Design Implementation	23
3.2.1	Microcontroller and Onboard Power	23
3.2.2	Measurement	24
3.2.3	Charging and Discharge Control and Safety	29
3.3	Measurement Calibration	33
3.4	Handling of Uncertainties	36
3.4.1	Propagation of Uncertainty	37
3.4.2	Sources of Uncertainty	37
3.4.3	Uncertainties of Derived Quantities	43
3.5	Function Validation	48
4	Cell Balancing System	53
4.1	Design and Implementation	53
4.1.1	Termination Balancing	55
4.2	Testing Methodology	55
4.3	Results	56
4.3.1	Test Procedure	57
4.3.2	Cross Sectional Tests	62
4.3.3	Replication Tests	68
5	Cell Modelling	70
5.1	Implementation	71
5.1.1	Original Implementation	71
5.1.2	Extensions to the Original System	71
5.2	Uncertainty in the Cell Model	72
5.3	Results	74
5.3.1	System Function	74
5.3.2	The Impact on Balancing Time from Lievre's Method	87
6	Discussion	91
6.1	System Design and Core Components	91
6.1.1	Measurement Systems	91
6.1.2	Safety Systems and Charging Control	92
6.2	Balancing System	93

6.2.1	Comparison to Algorithms in the Literature	93
6.2.2	Termination Balancing Function	95
6.3	Lievre's Method	96
6.3.1	System Performance	96
6.3.2	Self Induced Current Events	97
6.3.3	Selection of Weighting Parameters	98
7	Conclusions	99
References		101
Appendices		105
A	3D Least Squares Uncertainties	105
B	System Schematic	109

Nomenclature

<i>Cell</i>	A single electrochemical unit, with an anode and cathode
<i>Battery</i>	A combination of cells in parallel and/or series.
<i>SoC</i>	State of charge, charge remaining as a % of total charge. e.g. SOC = 100% represents a fully charged battery.
<i>B1, B2, B3, B4</i>	The labels assigned to each cell in this paper. Cell B1 is the cell which shares its negative terminal with ground. <i>B</i> is used rather than <i>C</i> so as to avoid confusion with capacitance and C rating.
<i>Battery Current</i>	The conventional current flowing out of the positive terminal of the battery. Denoted as I_{Bat} or IBat in code. Active sign convention is observed; during charging I_{Bat} is negative, during discharge I_{Bat} is positive.
<i>Open Circuit Voltage (OCV)</i>	The voltage of a battery at rest for a sufficient amount of time.
<i>Equivalent Circuit Model (ECM)</i>	A model of a battery in the electrical domain.
V_{CELL}	The voltage across the terminals of a cell.
<i>LSB</i>	Least Significant Bit.
<i>Lievre's Method</i>	The method for estimating R_i as proposed in [2] by Lievre et al.

Chapter 1

Introduction

Battery technology enables the portable electronics of the modern day. Lithium-ion batteries power smart phones, computers and electric cars, but they bring with them safety hazards and specific management requirements.

This project will identify the key considerations and implement a lithium-ion battery and battery management system for a robot platform. A particular challenge occurs in batteries comprised of multiple cells in series, the cells can become *unbalanced*, where some cells are more charged than others. Battery imbalance can, in turn, reduce the working life of a battery and even cause safety hazards. In an attempt to remedy this, a passive cell balancing system will be tested. A gap exists in the literature on control algorithms for passive balancing systems. In order to fill this gap, an algorithm controlling the balancing system will be developed and evaluated. Furthermore, a method for estimating the internal resistance and *open circuit voltage* of the cells to improve the balancing algorithm's performance, will be implemented from the literature and evaluated.

1.1 Project Background

The application for the proposed system is to fit the requirements of a separate project developing an autonomous robot platform for spatial mapping of mobile networks. The robot platform is designed to be charged at a base station from utility power. It is to autonomously traverse an area under battery power. Another requirement to keep in mind is that the onboard systems have a minimum voltage

requirement of 12V. As the system will operate without supervision, safety will have a high priority. Increasing the run time and decreasing the charging time improve the robot's cost effectiveness and will thus be of high importance in the planning.

1.2 Project Scope and Aims

The objectives and aims of this project are to design and build a battery system for the robot application detailed. The design of the system will cover identifying an appropriate structure to meet the application, and selection of components to implement that structure. The capabilities of the constructed system will be verified for the application system by uncertainty analysis and testing of the hardware.

The scope of this project will include the selection of battery cells and design and construction of the battery system, firmware and control algorithms. The charging system will also be considered, as it relates to the battery system. However, the power distribution onboard the robot application will not be examined.

1.3 Layout of the Report

This report will be structured around the three main chapters, *System Design* 3, *Cell Balancing System* 4 and *Cell Modelling* 5. Each of these chapters will include the design of the system in question, methods for evaluation, finishing with the results.

The main chapters will be preceded by the *Literature Review* 2, where considerations in designing a battery management system are identified, followed by a review of balancing methods and cell modelling techniques used in the field.

The chapter *System Design* 3 will look at designing of the hardware, the safety and charging control algorithms, and analysing the uncertainties in measured quantities.

In chapter *Cell Balancing System* 4 a passive balancing system will be chosen and implemented. Additionally, the algorithm for controlling the system will be designed and verification of the system presented.

The *Cell Modelling* 5 chapter will implement a method from the literature by Lievre et al. [2]. Their method will be extended to satisfy the project's application

and the selection of parameters analysed. Furthermore, the effect of cell modelling on the balancing system will be quantitatively analysed.

The chapters *Discussion 6* and *Conclusions 7* will provide an analysis and comparison of the results of the three main chapters.

Chapter 2

Literature review

2.1 Introduction

LiBs are used across a wide scale of applications: portable electronics, hybrid and fully electric vehicles (EVs), and in grid level energy storage. Due to their popularity, different areas of their function, management and applications have been studied and widely reported.

2.2 Battery Technology

2.2.1 Lithium-ion Battery Chemistry

Miao et al. [3] in their review *Current Li-Ion Battery Technologies in Electric Vehicles and Opportunities for Advancements* gives detail on the chemistry of LiBs, along with many considerations and factors which affect the suitability of different chemistries and implementations. The paper does not present new findings, but draws on current literature to give a top down account.

Hannan et al. [1] discuss the fundamental topics in battery selection and battery management system (BMS) design in their review *State-of-the-Art and Energy Management System of Lithium-Ion Batteries in Electric Vehicle Applications: Issues and Recommendations*. They discuss the fundamentals of LiBs and BMSs, and are cited by Miao et al [3].

There are many alternative battery technologies besides Lithium ion. The mod-

ern popularity of LiBs' is identified by [3] and [1] as the combination of their specific energy, cycle life, cost, self-discharge rate, and efficiency. Firstly, to compare the specific power and specific energy of popular battery chemistries, both papers reference a Ragone plot as seen in figure 2.2. The plot compares energy density and power density of battery technologies, showing Lithium based technologies surpassing older technologies in both categories. Many similar plots have been published by different authors demonstrating a similar trend [4]. Secondly, [3] use the common definition of cycle life as the number of discharge and charge cycles before a battery's capacity is diminished to 80% of its nominal capacity. In addition, LiBs are shown to have coulombic efficiency greater than 99%.

Understanding the properties and handling of LiBs is rooted in the chemical action within a cell. Many studies discussing LiBs and BMSs, [1, 3, 5, 6], support their arguments by examining the principals of a cell's action.

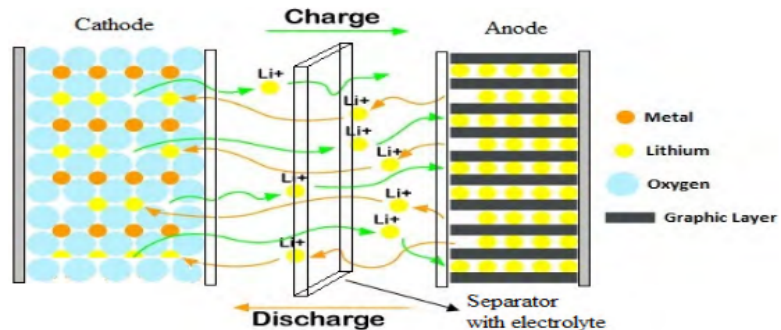


Figure 2.1: The movement of ions within a Lithium cell [1]

LiBs are composed of two electrodes: an anode connected to the negative terminal and a cathode connected to the positive terminal. The electrodes are separated by a permeable membrane saturated in an electrolyte. The cathode and anode are crystalline materials that contain Lithium atoms embedded, or *intercalated*, in their lattice. During the battery discharging, Lithium atoms are ionised and moved into the electrolyte from the anode. They are deionised, in turn, at the cathode where they reenter the lattice. This processes is called deintercalation and intercalation respectively. Similarly during battery charging, the process operates in reverse. Both processes can be seen in figure 2.1. [1, 3, 5, 6]

The NASA Aerospace Flight Battery Program, Volume II, Appendix B: Guide-

lines on Lithium-ion Battery Use in Space Applications, by Manzo et al. [5], provides a highly informative account on the considerations for the use of batteries in critical systems. The study discusses the major factors in selection and qualification of cells. They also perform their own tests and comparisons.

Liu et al. concisely describe the cathode, anode, and electrolyte as the most influential components of a battery's performance [6]. Anode and cathode materials dictate the cell voltage at rest and account for a significant portion of a cell's mass. The anode material used in LiBs is most often a synthetic graphite. Cathode material, on the other hand, has significantly more variety. Different cathodes have properties which make them more suitable for varying applications, such as lower fire risks, lower self discharge rates, specific power levels or specific energy levels, etc. [3, 6]

The electrolyte and membrane allow transport of Lithium ions between the two half reactions on the surfaces of the anode and cathode. Similarly to the variety of cathode material, there are an array of electrolytes in use today. The most common one is an electrolyte comprised of a Lithium salt in an organic solvent. Furthermore, there are a range of additives for electrolytes which alter their properties, such as their flammability or interactions on the surface of electrodes. It is the electrolyte that limits the upper voltage window of a LiB. If a high enough voltage is placed across a cell, the electrolyte will break down. This process, in turn, deposits lithium metal causing internal shorts; releases gasses causing internal pressure; deposits a passivation layer on electrodes, increasing internal resistance. Therefore it is critical that a nominal maximum voltage, typically 4.2V, is observed for safe operation of LiBs. [1, 3, 5, 6]

Six cathode materials are considered in [3] and [1] including: Lithium Nickel Cobalt Aluminum Oxide (NCA), Lithium Iron Phosphate (LFP) and Lithium Cobalt Oxide (LCO). They identify six key attributes for comparing the six cathode materials: specific energy, specific power, safety, performance, life span, and cost. The authors argue that there is no ideal battery composition, but that the choice should match the requirements of the application. The comparison of the components by both reviews is informative as an overview of the market, but their data is only ordinal. Relevant to this project, the authors of both reviews identify NCA, from the materials considered, as having maximum specific energy and high specific power.

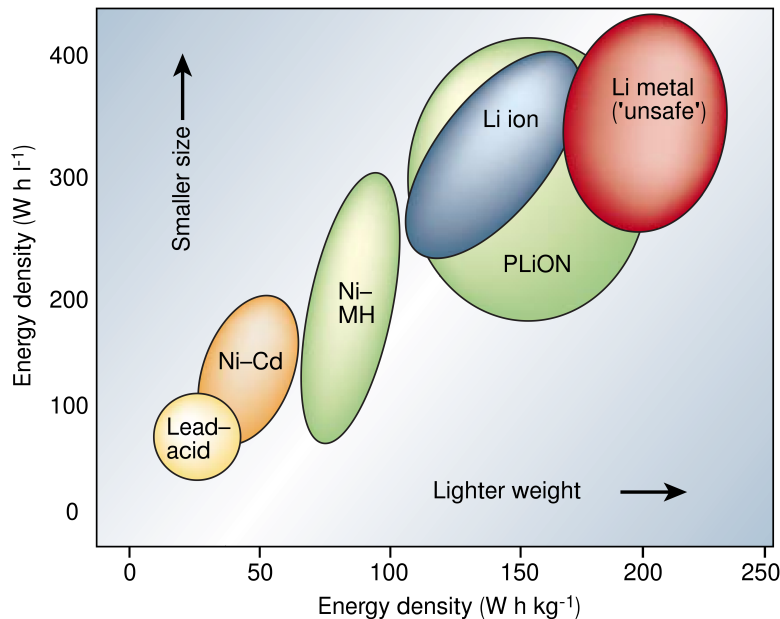


Figure 2.2: A Ragone plot comparing popular battery technologies [4]

The performance of a cell can degrade with improper use. Varied pathways towards degradation exist, from thermal runaway to buildup of passivation layers on the electrodes. Temperature is identified as a key factor [5], in the performance of LiBs. The optimal operating temperature range for a particular chemistry varies, but is commonly between 20°C and 40 °C [3, 5]. Chemical activity is heavily influenced by temperature. For example, lower temperature increases a cell's internal resistance, as seen in figure 2.3. The degradation issues are discussed and agreed upon by [3], [1] and [5]. All three studies list numerous ill effects of operating outside the recommended temperature, including anode plating at low temperatures and chemical breakdown at elevated temperatures. The influence on the cycle life by temperature is approximated in [1], as shown in Figure 2.4. In addition to the ambient temperature, high currents can also elevate a cell's temperature and cause serious damage.

The procedure for charging LiB is universally described as a *constant current - constant voltage* (CC-CV). First the battery is charged with a constant current, the cell voltage rises until the maximum voltage is reached when the voltage is controlled in the constant voltage phase. Charging is then terminated when the current falls

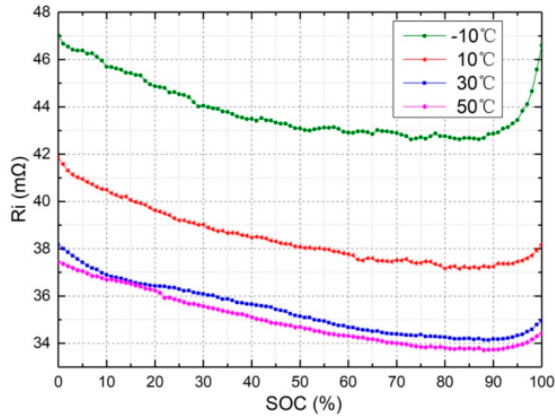


Figure 2.3: LiB internal resistance, R_i , over temperature and State of charge variation [7]

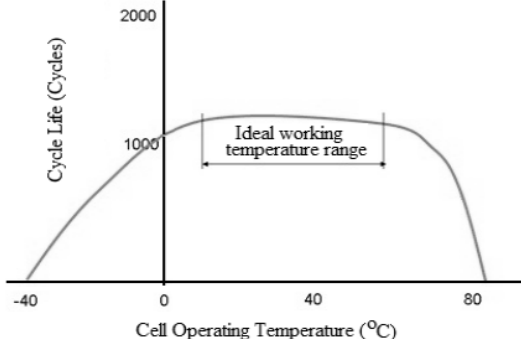


Figure 2.4: LiB cycle life dependency on temperature [1]

below a threshold [1, 3, 5].

A value known as C_{rate} , or simply C, is used to describe charging and discharging currents in comparison to a cell's capacity. It is defined as $C_{rate} = \frac{P_{ch}}{E_{cap}}$, where P_{ch} is the maximum charging power and E_{cap} is the total battery capacity [3]. C_{rate} has units of $hours^{-1}$, thus discharging a cell at 1 C will take 1 hour, 2 C will take 0.5 hours. Battery manufacturers use C to specify the maximum continuous discharge current, maximum charging current and charging termination current [3, 5].

The CC-CV procedure is a product of the limits of operating conditions of LiBs. Heating and other effects limit the maximum cell current, while the electrolyte properties limit the maximum voltage. Therefore, to safely charge a cell in minimum time is by following the CC-CV procedure.

An important measure while using a battery is its state of charge (SoC). It is defined as $SoC = \frac{E_{releasable}}{E_{rated}}$ [1, 8]. SoC is dimensionless and is commonly reported as a percentage. The complement to SoC is depth of discharge (DoD), defined as $DoD = 1 - SoC$. DoD describes the amount of charge removed from a cell, in other words its utilisation. It makes intuitive sense that higher DoD would slowly wear out a cell. This correlation is widely reported in the literature [3, 9, 10]. The correlation can be seen visualized in figures 2.5 from Cassani and Williamson [10]. Not only do they demonstrate a reduction in cell life, but that it is not made up by the higher utilization of each cycle.

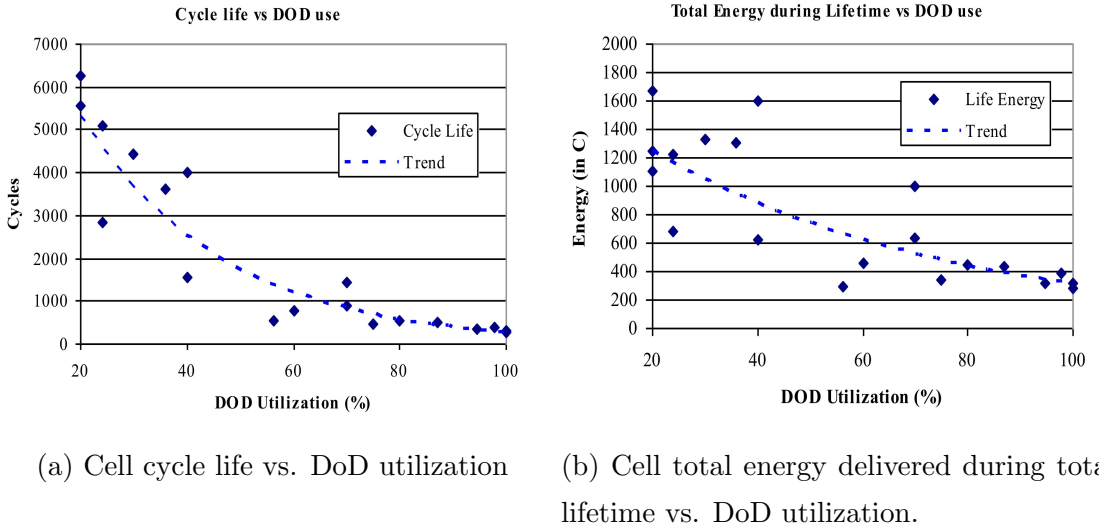


Figure 2.5: The inverse correlation between DoD and cycle life [10]

2.2.2 Battery Modelling

Determining the SoC of a battery can be a difficult process, for which many techniques have been developed. A wide overview of the area of research is provided by Waag et al. [11] in their 2014 paper *Critical review of the methods for monitoring of lithium-ion batteries in electric and hybrid vehicles*. The study lists other measures alongside SoC. The most popular approaches, according to their findings, are based on electrical models of cells, where measurements of the cells are connected to model parameters. A common assumption is that battery open circuit voltage (OCV), the voltage of a battery not recently under load, is a nonlinear monotonic function of the SoC [3, 11, 12]. Unfortunately OCV often differs greatly during use, and can only be observed after a period of relaxation.

A detailed account of the issues in cell modelling, in addition to the fundamentals of battery system design is provided in the 2002 book *Battery Management Systems* by Bergveld et al. [13] of *Philips Research Laboratories*. Explanations for influential factors and equations that describe the voltage response of a cell are accounted for in the study [13]. In addition, they provide detailed descriptions of the chemical reactions involved in LiBs. They derive an intricate equivalent circuit model (ECM) for an LiB, and then provide a simplified and more practical model with four lumped components, as shown in figure 2.6 This lumped model, and variations of it, are used

extensively in the literature [2, 7, 11, 14–24]. A similar approach will be taken in this project.

Multiple naming schemes are used for the components of similar ECMs. In figure 2.6 the following definitions are used: terminal voltage of the cell is $V_{bat} = EMF + \eta^k + \eta^d + \eta^\Omega$, where EMF is the equilibrium potential of the cell, also known as the OCV. The η components are known as overpotentials. They are voltages induced by cell current. Specifically, η^k is the sum of kinetic overpotentials, η^d is the sum of diffusion overpotentials, and η^Ω is the sum of ohmic overpotentials. To provide a simplistic description of the overpotentials would be to attribute the diffusion components to the movement of ions in the electrolyte, kinetic components to the reactions at each electrode, and ohmic components to the sum of real resistance through the cell. The ECM is further analysed in the time and frequency domains. In the complex impedance domain of a Nyquist plot the values of certain elements can be identified, which are informative for the condition of the cell. This technique, known as the electrochemical impedance spectroscopy (EIS), is very powerful, but requires specialised laboratory tools. The power and utility of EIS is represented by its popularity in the literature [18, 20, 21, 25]. The overpotentials are also shown in the time domain by [13] as the response to a step current. In figure 2.7, they attribute ΔV_1 to R_Ω and ΔV_2 to both η^d and η^Ω . Identifying R_Ω is useful as a measure of battery condition. In addition, they observe that in figure 2.7, the differential resistance of the cell at t_1 is $\Delta V_1 / \Delta I = R_\Omega$.

A cell's ohmic internal resistance is described by many different terms by different authors: R_Ω [13, 18, 26], R_i [7, 21], $R_i + R_{ct}$ [14], R_0 [2, 11, 17, 19, 22, 23, 27], R_s [16, 24]. The choice of term is derived from the authors' cell model. For simplicity, in this paper the purely ohmic component of a cell's resistance will be denoted as R_i .

The relationship between SoC, OCV and terminal voltage is demonstrated in [15]. As part of their investigation, the authors discharged and charged a cell with regular pauses to observe the voltage relax. Their results are shown in figure 2.8. Although it is not shown, time progresses in clockwise around the cell voltage curve. The hysteresis is caused by cell overpotentials, reducing the cell voltage during discharge and increasing it while charging. The cell OCV is approximated by the large dashed line, with lower currents or longer pauses the cell voltage would approach closer to

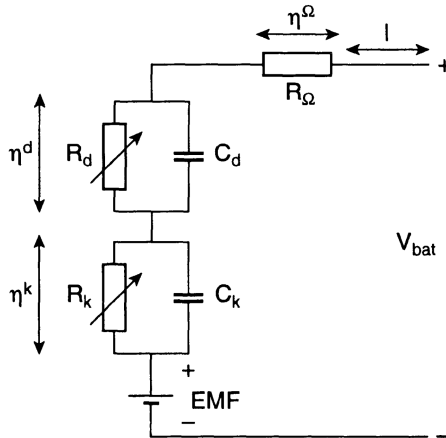


Figure 2.6: Simplified battery equivalent circuit model [13]

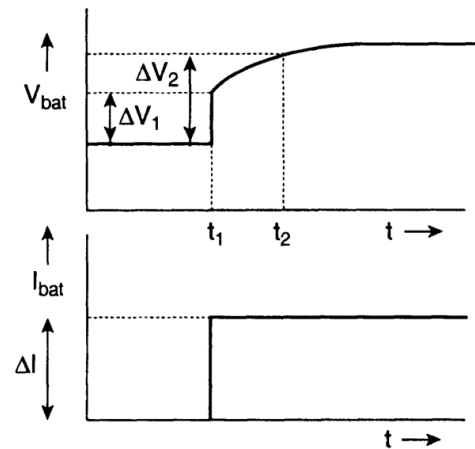


Figure 2.7: Cell overpotentials [13]

that line. During the rest periods the large immediate voltage rise is due to the ohmic components of the cell impedance. Similar plots are shown in the results of this project, figures 4.8 and 5.14.

In 2002, when the study by Bergveld et al. [13] was published, LiBs did not have the market dominance they do today. Due to this, their discussion is not limited to lithium technologies, but also includes Nickel based batteries. They make an important observation on the CC-CV procedure within the discussion of overpotentials. They show that an increase in charging current has a diminishing return on charging time, as can be seen in figure 2.9. They explain that an increase in current, during the CC phase, leads to greater overpotentials. This in turn leads to a transition to the CV stage at a lower SoC.

2.2.3 Cell Balancing

A specific problem occurs when charging batteries comprised of multiple cells in series as LiBs cannot tolerate voltages above a maximum. If the charge controller only observes the whole battery for voltage control, then it is possible that the average cell voltage is at its maximum, while some cells are below and others above their maximum. This is referred to as cell imbalance and is caused by the inevitable mismatch between cells in their capacity, OCV to SoC response and overpotential

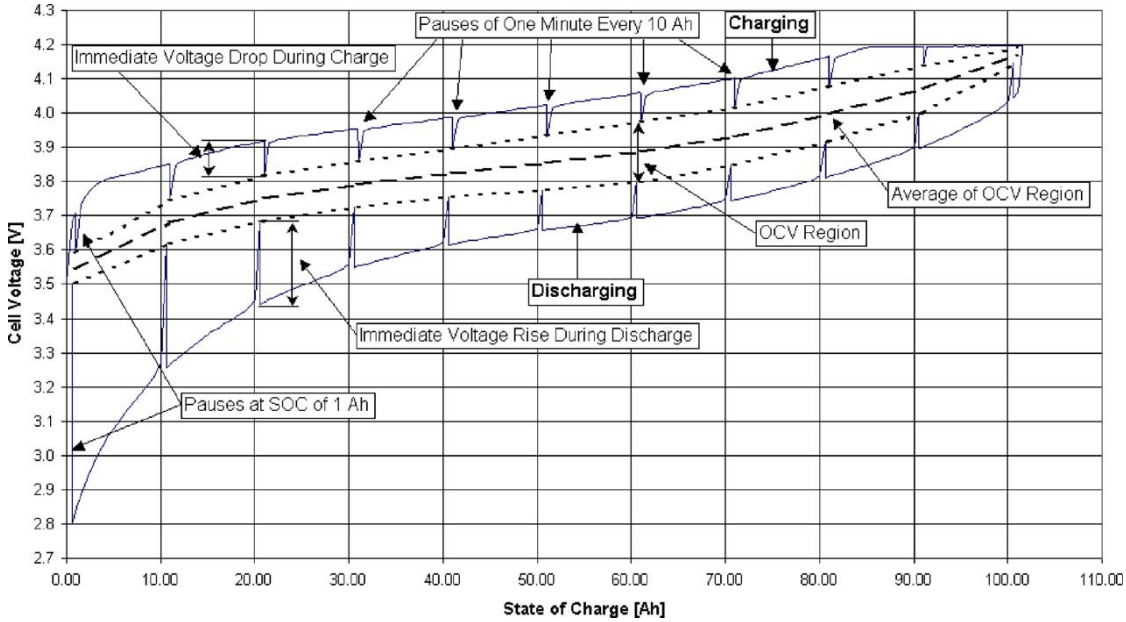


Figure 2.8: Cell voltage hysteresis and the OCV relationship with SoC [15]

magnitudes. Apart from the arduous task of finding cells with identical parameters, this problem is resolved by observing the individual cell voltages and altering their net charging rate [1, 3, 13, 28, 29].

The methods for altering a cell's net charging rate are compared in [29]. The approaches are classified into either active or passive methods. Passive methods partially divert charging current from a cell through a resistor. Active methods, on the other hand, use reactive elements to transfer charge to or from a cell. The authors describe a passive system and multiple active systems, as well as their operating principals, effectiveness and component counts. However, they do not discuss the specifics of the algorithms for controlling the application of balancing, other than noting the simplicity of some.

The controller for a passive system in figure 2.10a determines which cell is at risk of overcharging and closes the switch to its shunt resistor. The active system in 2.10b is a small example of a charge shuttling system, known as a flying capacitor. The capacitor is alternately connected across B1 and B2 where it charges to the cell's voltage: if the cells have a difference in voltage, the capacitor will transfer charge as it changes from one cell voltage to the other. A flying capacitor is a simple active

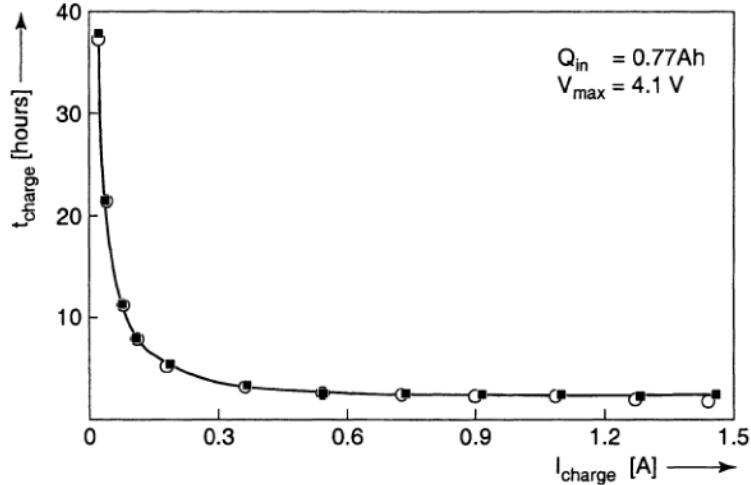


Figure 2.9: Charge time as a function of charging current [13]

system, it suffers in cases of small charge differences where the balancing time grows exponentially. Active systems are classified into charge shuttling, like the flying capacitor, and energy converters, in [29]. The energy converter systems, presented in the study, use transformers between the whole battery and each individual cell to transfer energy either from an overcharged cell to the whole battery, or from the whole system to an undercharged cell.

A comparison of fifteen balancing circuits was conducted in [28]. The authors compared component counts, balancing speed and application power. Their component counts were parametrised for the number of cells. For balancing speed, the levels *Satisfactory*, *Good* and *Very good* were noted, while for application power the levels were *Low* and *Medium/High*. No specification for the scale of time or power were given. They found passive balancing, as in 2.10b, to have a good balancing speed and low application power. The highest performing systems were inductor based and a full bridge convert, all with very good balancing speed and medium/high application power. Apart from the component count, all results were only reported in ordinal levels, there was no discussion of the scale of speed or power.

Similar qualitative evaluations of various balancing techniques were undertaken in [30] and [31] with similar conclusions. The authors also perform simulated experiments with the balancing circuits. Their procedure was to simulate four batteries with varying SoC (e.g. 80%, 78%, 76% and 74%) being charged and balanced.

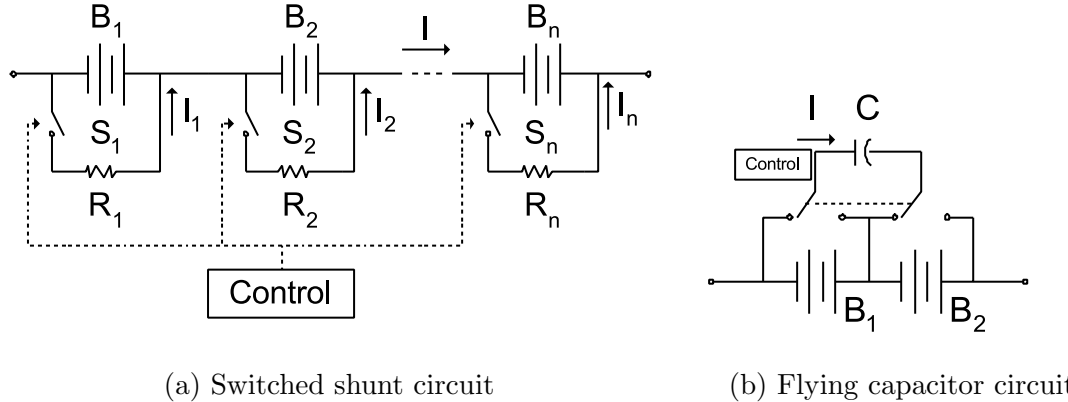


Figure 2.10: Cell balancing circuits [29]

Unlike others, [30] and [31] do have a limited discussion of the algorithms used to apply balancing. Their passive balancing algorithm only applies cell shunts during the final phase of charging, immediately before charging is finished. They do not discuss the justification for this system.

An advantage overlooked by both [28] and [29], is the scalability of passive balancing systems. In a configuration where multiple battery packs are combined in a modular system, passive balancing will maintain its effectiveness. Active systems are unable to balance between battery packs without additional circuitry. This is simply because most active systems rely on the charge transfer from either a cell to the pack or pack to a cell, so cannot balance on a pack to pack level.

As a trend, active methods have higher efficiencies than passive, but at the expense of higher complexity. These factors will be considered in the context of the requirements of the application in this project. Both [29] and [28] conclude with the importance of a balancing system for LiBs. Furthermore, [29] discuss how the application must justify the complexity of the system, while [28] simply state that active systems are preferable.

2.3 Battery Management Systems

Bergveld et al. summarise their field:

”The basic task of a Battery Management System (BMS) is to ensure

that optimum use is made of the energy inside the battery powering the portable product and that the risk of damage inflicted upon the battery is minimized. This is achieved by monitoring and controlling the battery's charging and discharging process.” [13]

All three studies [13], [3] and [1] describe possible functional blocks for achieving the goals summarised in the above quotation. Common blocks include: temperature management, cell balancing, battery protection, charging control, to mention a few. The main components considered in this project, which also feature in all of the previous studies, will be: measurement functions, control algorithms and switching components. Firstly, important measurements are cell voltage, current and temperature. Secondly, control algorithms are software that read the measurements, activate the switching components, calculate derived quantities of the battery and communicate with other systems. Finally, switching components are used to control balancing systems, cell protection, charging and discharging.

All three papers list different sets of fundamental components for a BMS, this is due to a few different reasons. One reason is that the topic is too nebulous to be summarised in such a way. Another reason is that [13], [3] and [1] strive to define a general BMS and come to different conclusions, as [13] argues, because the degree of sophistication must be justified by the application. Furthermore, [13] work in the domain of handheld electronics, [3], whereas [1] work on electric vehicles.

According to [13], the designer must consider the following categories: the cost of the product, features of the product and the type of product. The cost and features of the product are closely related, for example, reporting the state of charge increases cost and complexity. Considering the type of product means to review the expected lifetime, charging schedule and discharging rate.

The most critical function of a BMS is maintaining the safety of the system. As mentioned previously, thermal runaway or cell degradation can be caused by operating outside the safe operating region. [13] describe a simple safety switch in series with the battery to isolate it, in case of unsafe operation. As has been put forward by [1, 3, 5, 13], the three important safety criteria are voltage, current and temperature.

The charging control of a BMS, on the other hand, requires a power supply

that can regulate current and voltage, as well as control for appropriate charge termination. [13] discuss the options whether to position the power electronics, power electronic controls and charging controls on board or off board. They do not conclude that any configuration is superior, but that the design must be justified by the application.

2.4 Derived quantities

There are important quantities for battery management, which are not as tangible as voltage, current and temperature, but can only be derived: SoC, battery capacity and internal resistance, to mention a few. Calculation of these quantities are most heavily affected by the limits of sophistication, stated by [13]. Unfortunately, some quantities require computation and detailed measurements, which are not necessarily available. Derived quantities describing the state of the battery, are often to be communicated to other systems. [13] introduce the system management bus (SMBus) standard, popular in computers, it lays out communication of run time to empty, SoC, cycle count.

The measure R_i is used in methods for estimating battery *health* [17, 23], voltage drop prediction [2] lifetime [22], power capability [21] and SoC [7, 19].

An industry research group *PNGV*, led by the US government, standardised a popular test procedure for batteries in a hybrid electric vehicle setting. The test procedure is called: the hybrid pulse power characterisation (HPPC) test [32]. The main purpose of the test is to quantify the battery impedance and power capabilities in charging and discharging. It is a simple current profile: 18 seconds of constant discharge, 32 seconds of zero current, 10 seconds of charge current. In order to better understand the characteristics of a battery, the test can be repeated over the cycle life of a battery, or over varying SoC. PNGV provide a set of calculations on the test results to derive R_i , OCV, and time constant. Battery impedance is derived from the HPPC test by observing the change in voltage with a change in current. The relationship between the two is the differential resistance, as seen in figure 2.7. This test, and alterations of it, is often cited for either characterising batteries or as the basis for a more targeted test [2, 7, 14, 19, 23].

Stroe et al. [21] implement a modified HPPC test to determine a cell's impedance.

Their modified test uses alternating current pulses growing in magnitude, as seen in figure 2.11. An individual current pulse and expected voltage response is shown in figure 2.12, experimental measurements of positive current pulses are shown in figure 2.13. The measurements of $R_{\Delta V/\Delta I}$ by [21] for varying SoC can be seen in figure 2.14.

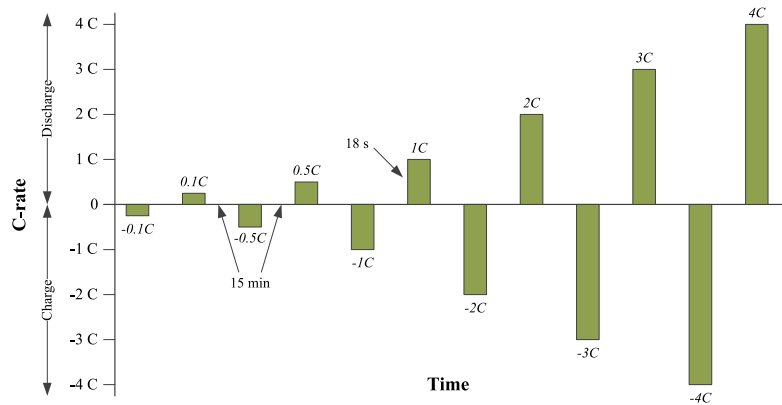


Figure 2.11: A train of current pulses [21]

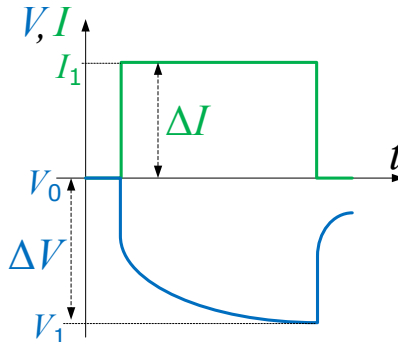


Figure 2.12: An example current pulse and voltage response [21]

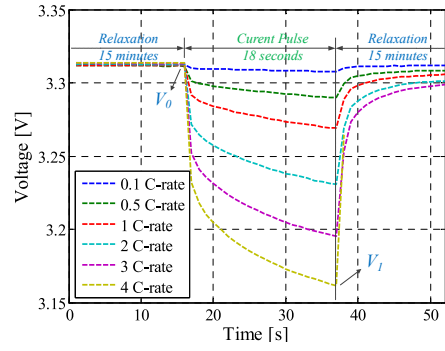


Figure 2.13: Voltage response to (positive) current pulses [21]

Further along, [21] use the more precise technique of EIS to determine the complex impedance as a function of frequency. Their results show the resistance at 0Hz, R_i , to be approximately $5m\Omega$. Their results from HPPC testing, shown in figure 2.14, give a value three times that found through EIS. This is due to the fact that during their HPPC based test there is a large time difference between the measurements. Figures 2.12 and 2.13 show how the voltage changes sharply, followed by a

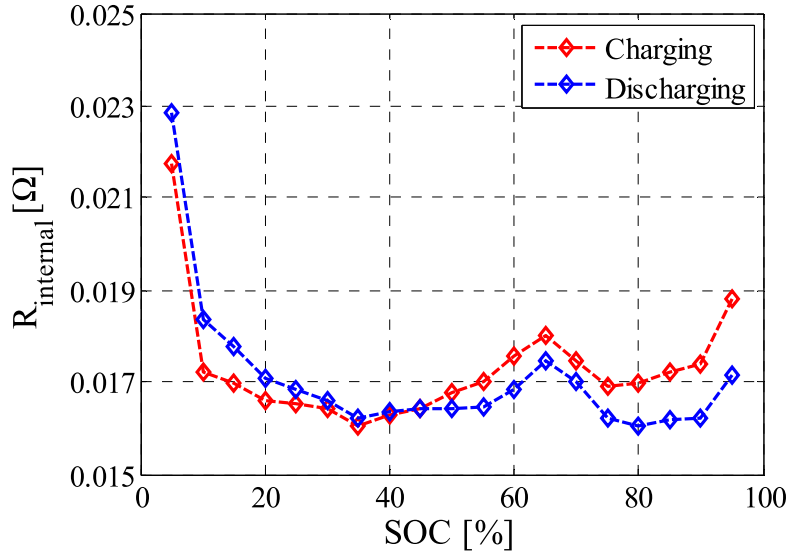


Figure 2.14: Cell impedance variation across SoC [21]

capacitor-like curve. Clearly, the measurement will represent both ohmic and non-ohmic components. This does not form part of the authors' discussion, they do not compare the results, perhaps because they view them as having different purposes.

Kim et al. [14] use an HPPC derived test procedure, similar to [21], but distinguish between the ohmic and non-ohmic components of the response. The chemistry of the LiB used in the study [14] is not specified, nevertheless, they report a consistent lumped impedance of approximately $65m\Omega$. Interestingly, [14] make an observation that the impedance can be determined graphically, by plotting the current pulse magnitudes against the voltage change. Figure 2.15 shows such a plot, where the dashed line is the impedance, denoted DCIR. A similar plot is shown in the results section of this project, in figure 5.6

2.4.1 Real Time Impedance Estimation

Lievre et al. [2] propose a technique for determining part of the internal impedance of a cell, by simple observation of a cell during operation. Their application is in a hybrid vehicle, with large repeated charging and discharging currents. Their approach is to observe changes in current and voltage, to derive a differential resistance, as in 2.1. It is then further aggregated into a value they call R_S , representing

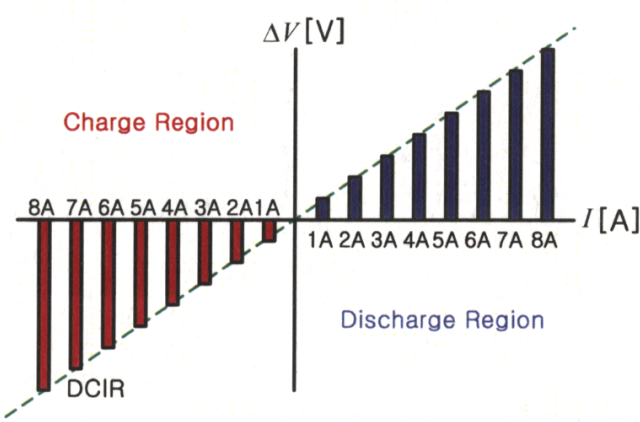


Figure 2.15: Current and voltage differences during current pulse train [14]

the ohmic and a selection of non-ohmic components. The study uses an ECM similar to figure 2.6, but with an arbitrary number of $R||C$ elements, shown in 2.16. They show, by approximation, that when sampling at Δt intervals the differential resistance will represent R_i and the $R||C$ components with time constants between $\Delta t/3 < R \cdot C < \Delta t \cdot 10$.

However, a clear issue with equation 2.1 is that for minimal current difference, $R_{\Delta V/\Delta I}$ will be highly sensitive to noise. In order to combat this issue [2] created a *quality coefficient*, as seen in equation 2.2 and in figure 2.2. I_{min} and I_{max} are fixed and chosen to minimise noise.

On selecting I_{min} and I_{max} , Lievre et al. state:

”The minimum variation is defined to remove measurement noise by fixing its value above the sensitivity of current sensors. The maximum variation is defined as the nearest value to the most important variation, which can occur in a typical use of the cell (calculation of $R_{\Delta V/\Delta I}$ is considered optimal in this situation).” [2, p. 4507]

Their criteria for optimality is not defined and they do not provide any supporting arguments for this statement. Their conditions are, if anything, the maximum bounds; larger bounds would be counter productive by including noise and or excluding large current events.

With this scheme $R_{\Delta V/\Delta I}$ can be calculated for every pair of samples. A first order infinite impulse response filter was employed to provide a more stable value,

R_S , as in equation 2.3. The feedforward parameter $\alpha_k = \alpha_{max} \times \alpha_{quality,k}$, where $\alpha_{max} \in [0, 1]$. The initial condition R_{S_0} must be set, but does not affect the long run value of R_s . [2] show that R_s will converge to the same result for different initial conditions.

$$R_{\Delta V/\Delta I} = \frac{\Delta V}{\Delta I} = \frac{V_k - V_{k-1}}{I_k - I_{k-1}} \quad (2.1)$$

$$\alpha_{quality} = \begin{cases} 0, & |\Delta I| < I_{min} \\ \frac{\Delta I - I_{min}}{I_{max} - I_{min}}, & I_{min} \leq |\Delta I| \leq I_{max} \\ 1, & I_{max} < |\Delta I| \end{cases} \quad (2.2)$$

$$R_{S_k} = R_{S_{k-1}} \cdot (1 - \alpha_k) + R_{\Delta V/\Delta I} \cdot \alpha_k \quad (2.3)$$

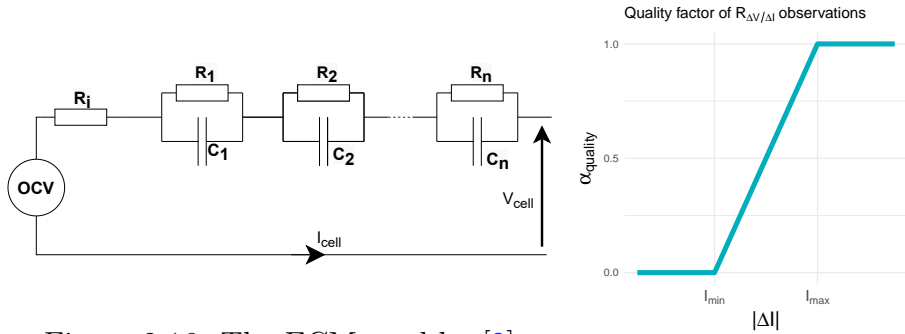


Figure 2.16: The ECM used by [2]

Figure 2.17

[2] note that a direct comparison between EIS and HPPC based tests cannot be done. The different current levels, rest periods and physical configuration between the types of tests will give inherently different impedance measurements. To validate their results they test the affect of temperature on R_s , noting that $R_s \propto 1/T_{cell}$, as would be expected. They produce a polynomial fit for the relationship, enabling them to normalise R_s for use in state of health calculations.

The test described by [2] has the benefit that it can be conducted online during normal operation of the battery. There is no need for the specialised offline testing devices used by [21] and [14] to generate current pulses. This is only the case in hybrid-like applications, where high variations in current are present. Henceforth,

the method described by Lievre et al. [2] will be referred to as Lievre's method for simplicity.

2.5 Gaps in the knowledge

The method introduced by [2] is only applicable in systems with regular high current events. The lower limits of such events are not discussed, neither are techniques for circumventing this problem. Furthermore, the selection of I_{min} and I_{max} values by [2] is not well explored. The authors' do not investigate the affects of varying the values, or discuss the meaning of the "sensitivity" of a current sensor. For example, sensitivity could refer to minimum resolution, noise floor or uncertainty in the measurement. In this project a novel method will be introduced for generating changes in current by using already existing balancing circuitry. In addition, analysis of uncertainties will be used in the selection of I_{min} and I_{max} .

The specific algorithms used for cell balancing are not widely available or discussed. In the limited discussion, such as by [30] and [31], only a simplistic algorithm is presented without justification or analysis. In this project, a more broadly effective algorithm will be implemented and analysed for its energy efficiency and charging time.

A fundamental component of any balancing algorithm is to identify the cell which will reach its maximum voltage soonest, i.e. assuming similar SoC to OCV relationships between cells, the cell with the highest SoC. Due to the complications of overpotentials, simple observation of a cell's terminal voltage is not sufficient to determine its SoC. The problem caused by overpotentials can be seen in a case of two similar cells differing only by their R_i values. Although during charging they may have identical SoC and OCV, the higher R_i of one cell will lead to a high terminal voltage. Simple observation of terminal voltage would suggest reducing the charging rate of the cell with a large R_i , now unbalancing the pair. When the current is reduced the overpotential will be less and the new imbalance will be apparent, causing a new round of balancing to counteract the first.

To properly identify the cell with the highest OCV and SoC requires calculating the overpotentials. In this project Lievre's method will be implemented to improve the balancing algorithm by determine a ranking of the cells' SoC.

Chapter 3

System Design

This chapter considers the application's requirements and how the BMS is constructed to meet them. Cell balancing and estimation of internal battery resistance are covered in the subsequent chapters, but find their motivation and justification in the same interpretation of the requirements.

3.1 Design Requirements

Designing a battery for a particular system demands the identification of the application's requirements. The most important requirements are total energy, maximum power and cost. Firstly, the total energy determines the number and type of cells, but can be simplified if the design allows for modality. Secondly, maximum power will determine the cell chemistry and the rating of the power electronics used. Finally, cost is not only the upfront dollar value of the batteries and components but also includes the time dependent and ongoing factors, for example: the usable life of the battery and the costs of electricity for charging.

Once the capacity of the battery is determined, the cost of electricity for charging is only dependant on the efficiency of the system. Internal cell resistance, BMS power overheads, energy lost during balancing and unused capacity due to cell mismatch will all contribute to a lower efficiency. The significance of the efficiency loss compared to the increased complexity of the system must be considered.

To give maximum run time, the battery should have maximum energy density. NCA LiBs were chosen, as they have high specific energy and power. Four cells will

be used in series, in order to reach the 12V requirement. Specifically, the Samsung INR18650-30Q cells will be adopted, with a nominal capacity of $\sim 3\text{Ah}$ and a maximum voltage of $4.2 \pm 0.05\text{V}$. The four cells will be referred to as B1, B2, B3 and B4 throughout this project, with B1 being closest to ground. In addition, if it becomes necessary, multiple identical batteries with passive balancing may be used to form a larger pack, while still giving the same balancing performance, something that is not possible with active methods. As discussed in the project background, section 1.1, the application benefits from an extended run time, and uses relatively inexpensive utility power for charging. Therefore, an external charger will be applied. An advantage of this is that it also reduces the onboard weight.

A microcontroller unit (MCU) will be used in this project in order to implement the management algorithms, as opposed to a dedicated battery management IC. The advantages of adopting an MCU are that it allows for: flexibility, communication with other systems, and data logging. Safety will be ensured by the MCU monitoring the current, voltage and temperature of the battery. If necessary, the MCU will be able to individually disable charging and discharging of current.

3.2 Design Implementation

3.2.1 Microcontroller and Onboard Power

An MCU manages all of the BMS systems and algorithms. Its responsibilities are: collecting system measurements, controlling system isolation and charging, applying the balancing algorithm, deriving quantities such as R_i and accumulated charge, data logging, and communication. An STM32F103C8T6 MCU was selected for its low cost and broad range of capabilities, that reduce the constraints on development. Further advantages of the STM32 are that, if necessary, it can be placed into low power modes to conserve power, or even be replaced with a low power version in the same line after development is completed. An SD card is connected to the MCU to log the state of the BMS, batteries and record any specific events.

The MCU and other components require a standard 5V. This could be supplied with a buck converter taking power from the full stack of the battery. This means a step down of $\sim 11\text{V}$ and a lower efficiency for the converter. A higher efficiency could

be found by taking the input of the buck converter from only the two lowest cells, reducing the step down to $\sim 2.5V$, but this would inherently unbalance the battery. The penalty of lower efficiency is acceptable as the average current for the MCU and peripherals is minimal.

3.2.2 Measurement

Voltage Measurement

Measuring the terminal voltage of each cell is done using an analogue to digital converter (ADC) polled by the MCU at 2Hz. The voltage from ground to the negative terminal of a particular cell will be referred to as the common mode voltage (V_{CM}), while the voltage across the cell will be referred to as the differential voltage (V_{diff}). Figure 3.1 shows the voltages described in relation to two cells.

There is a fundamental challenge in configuring measurements of several cells in series. ADCs have a maximum measurement range, often 5V, so an ADC measuring from the negative terminal of a battery will only be able to measure the lowest cell. There are three prominent solutions to this problem. First, the implementation of several ADCs, to cover all of common mode voltage ranges. However, this solution would require several ADCs, level shifters for communication to the MCU, and a complicated power supply arrangement. Second, translating down the cell voltages into the operating region of an ADC tied to ground, effectively removing the common mode voltages. This could be accomplished with a specialised operational amplifier, known as differential amplifier. While differential amplifiers can give excellent performance, they come at a similar price to an ADC. Third, scaling the voltages into the input range of the ADC. A set of simple resistive voltage dividers could be utilised without the concern for input voltage limits that op-amps would bring. The benefits of this solution would be that voltage dividers have fewer components, and they only require one ADC with simple power requirements. However, scaling the voltages will be subject to resistor tolerances, reduced resolution, increased source impedance, and will not be suitable for large numbers of cells.

A voltage divider based sensing system is adopted in this project, its drawbacks can be mitigated while maintaining its simplicity and small overhead, as discussed in section 3.3. The ADC used is a MAX11616, a 12 channel, 12 bit ADC [33]. It

provides adequate resolution, surplus channels for possible experimentation, fully differential inputs and a 4.096V measurement range, thus 1mV resolution. The sensing circuit for one cell can be seen in figure 3.1, and can be found in full in the appendix B. To give the best accuracy measurements, two matched resistor dividers connected the ADC input to each cell's terminal with Kelvin connections. The MAX11616 ADC cannot tolerate a source impedance above 1.5 $k\Omega$. To facilitate this, a 10 nF capacitor was placed across the input of each channel. Although this reduced the bandwidth by forming a low pass filter, the source impedance was beneficially reduced. The cutoff frequency for the filter can be seen in equation 3.1, where R_1 and R_2 are the upper and lower resistors, respectively. The numerical values for the resistors, cutoff frequencies, and precision after scaling are shown in table 3.1

$$\omega_{-3dB} = \frac{R_1 + R_2}{R_1 R_2 C} \quad (3.1)$$

Cell	B1	B2	B3	B4
$R_1 [k\Omega]$	12	91	120	130
$R_2 [k\Omega]$	150	75	51	39
Ratio	0.926	0.452	0.298	0.231
ω_{-3dB} [Hz]	1432	387	445	530
Resolution [mV]	1.08	2.21	3.36	4.33

Table 3.1: ADC input network properties

The limited bandwidth does not impinge on the performance of the BMS, as will be demonstrated in section 5.3. The greatest sampling frequency is less than 60 Hz, almost one tenth of the minimum bandwidth. If necessary, the manufacturer states that a 100 pF capacitors can be used, giving a bandwidth in excess of 50kHz.

For optimum results, both channels of the differential input would be connected to the sensing points with identical voltage dividers. Any mismatch in the resistors results in the presence of V_{CM} in the ADC input. In the ideal case, only V_{diff} will appear on the input to the ADC. Common mode rejection ratio (CMRR) is a standard measure for the proportion of the common mode signal in the output of a system.

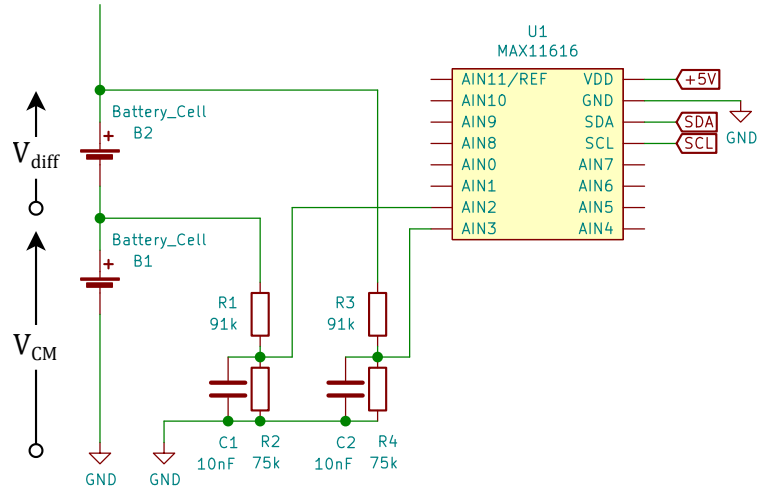


Figure 3.1: Differential Voltage Divider ADC Input (for one cell only)

CMRR is defined in equation 3.2. Differential amplifiers can have CMRRs in excess of 100dB, thanks to their precision trimmed internal resistor networks. Considering the network shown in figure 3.1 with 1% precision resistors, the worst case CMRR is calculated in equation 3.3 to be 30.1 dB for cell B4. To give perspective, this equates to an intrusion of V_{CM} 10% the size of V_{diff} . The common mode influence is linear, meaning that it can be mitigated through calibration, as will be shown in section 3.3.

$$CMRR = 20 \log \left(\frac{A_{diff}}{|A_{CM}|} \right) [dB] \quad (3.2)$$

$$V_{AIN3-AIN2} = V_{diff} \frac{R_4}{R_3 + R_4} + V_{CM} \left[\frac{R_2}{R_1 + R_2} - \frac{R_4}{R_3 + R_4} \right]$$

$$CMRR = 20 \log \left(\frac{R_2}{R_1 + R_2} \right) - 20 \log \left(\left| \frac{R_2}{R_1 + R_2} - \frac{R_4}{R_3 + R_4} \right| \right)$$

$$R_1 = 0.99R_a, \quad R_2 = 1.01R_b$$

$R_3 = 1.01R_a, \quad R_4 = 0.99R_b$, where R_a and R_b are the nominal values

$$CMRR = 20 \log \left(\frac{1.01R_b}{0.99R_a + 1.01R_b} \right) - 20 \log \left(\left| \frac{0.99R_b}{1.01R_a + 0.99R_b} - \frac{1.01R_b}{0.99R_a + 1.01R_b} \right| \right)$$

$$CMRR_{B1} = 50.6 dB, \quad CMRR_{B2} = 33.1 dB$$

$$CMRR_{B3} = 30.9 dB, \quad CMRR_{B4} = 30.1 dB \quad (3.3)$$

Current Measurement

The battery current was measured with an INA219 dedicated current sensor and a 0.1Ω shunt resistor. In each cell, the current was simply calculated from the battery current minus the current through the shunt resistor, which is known through Ohm's law and the state of the shunt switch. The reasons behind selecting the INA219 was its bidirectional capability and high resolution. The adopted shunt resistor gave the system a 0.1mA resolution and a maximum current of 3.2A. This range can easily be adjusted by replacing the resistor during development.

The sense resistor was placed in a high side configuration, above the positive terminal of B4. This does not cause the same issues of sensing as was seen with voltage. The INA219 incorporates, as is common in most current sensors, a precision trimmed differential amplifier with a CMRR of 120dB. High side sensing was used to remove the need for a voltage divider, to sense the voltage on the negative terminal of cell B1. As the INA219 was already equipped with high side sensing, this came at no extra cost.

Temperature Measurement

Samsung specifies that INR18650-30Q should only be operated between 0 °C and 50 °C. To monitor this, the temperature of each cell is measured with negative temperature coefficient (NTC) thermistors, one for each cell. Although a single sensor may be sufficient, and is often found in practice, four are used to give finer detail during development. The biasing circuit is shown in figure 3.2, where the nodes *TEMP_B1* among others are ADC inputs of the MCU. The MCU's internal ADC uses the same 3.3V supply as a voltage reference, simplifying the measurement. The simplicity and inexpensiveness makes thermistors suitable for this application. However, thermistors do not produce the most accurate temperature measurements, as will be discussed in section 3.4.2. The reason for measuring temperature in this project is to avoid overheating and damaging the cells, so that the accuracy they provide is sufficient. In order to calculate temperature from the ADC measurement, a simplified Steinhart–Hart equation is used, as shown in equation 3.4. In it the R_{lower} is the nominal resistance of the lower resistor, B is the thermistor's Steinhart–Hart parameter and R_0 is the nominal resistance of the thermistor at temperature T_0 .

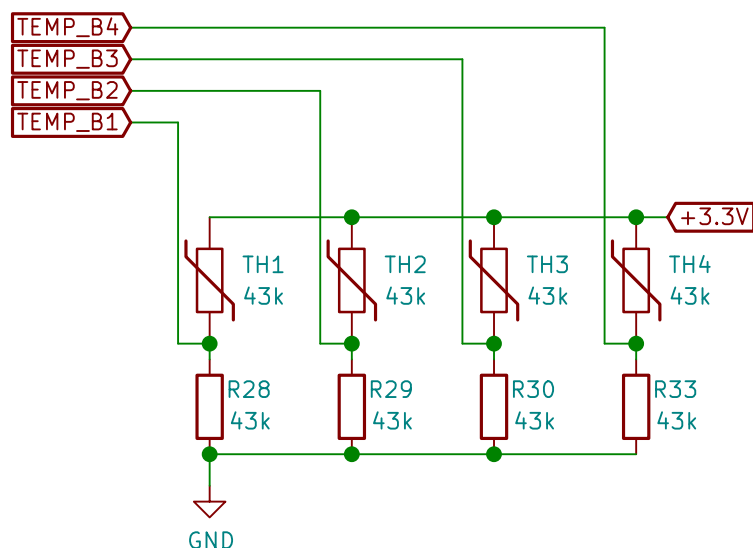


Figure 3.2: Cell temperature sensing circuit

$$\begin{aligned}
 R_{NTC} &= R_{lower} \left(\frac{1}{V_{TEMP_Bn}} - 1 \right) \\
 r_\infty &= R_0 e^{-B/T_0} \\
 T_{cell} &= \frac{B}{\log_e(R/r_\infty)} - 273.15 \quad [^\circ C]
 \end{aligned} \tag{3.4}$$

3.2.3 Charging and Discharge Control and Safety

A key requirement of the BMS is safe charging and operation. As discussed by [1, 3, 5, 13] in section 2, improper management of LiBs can lead to battery degradation or damage to other systems. The BMS must be able to handle various fault scenarios, in addition to the normal charging cycle.

Control Hardware and Charger

In order to control charging and isolation of the battery, the BMS uses two MOSFETs that individually control the battery charging or discharging of current. Bergveld et al. [13] stated that the system should be partitioned according to the application requirements. Following their advice, the charger is an external device to minimise onboard weight, while control over charging termination will remain with the MCU onboard. The charger is a DC power supply with current and voltage control functions set to 1.5A and 16.8V, respectively, as recommended by the manufacturer.

Selective control over charging and discharging current is accomplished by arranging the MOSFETs in *anti-series*, with their body diodes opposing each other. In figure 3.3 the MOSFET controlling discharging and charging currents are referred to as *ISO* and *CHG* respectively.

Safety and Charging Algorithms

As stated in section 2.3 cell voltage, current and temperature are identified as critical parameters for safety. This is implemented in the BMS with five fault conditions checked by the MCU, if any of the conditions occur, either ISO or CHG will be switched off according to the finite state machine models illustrated in figures 3.4 and 3.6. The Boolean fault conditions are: *over voltage*, *under voltage*, *over charge current*, *over discharge current*, and *over temperature*. These are combined into the

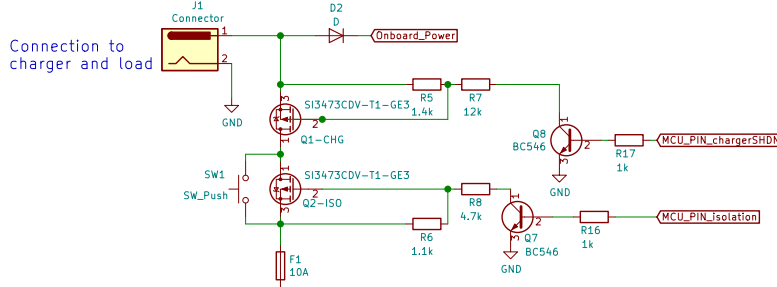


Figure 3.3: Battery input protection and charging control

values $CHGFAULT = \text{Over Voltage} \mid \text{Over Charge Current} \mid \text{Over Temperature}$ and $ISO\ FAULT = \text{Under Voltage} \mid \text{Over Discharge Current} \mid \text{Over Temperature}$.

The fail safe configuration of the battery input ensures that the battery only operates under supervision of the MCU. The CHG and ISO MOSFETs require the MCU's active control to connect the battery. Additionally, a fuse protects the battery and load against current faults that occur faster than the MCU can respond. Due to the MCU being powered from the battery through the ISO MOSFET, it can be booted either by connecting a charger, or with the momentary switch portrayed in figure 3.3.

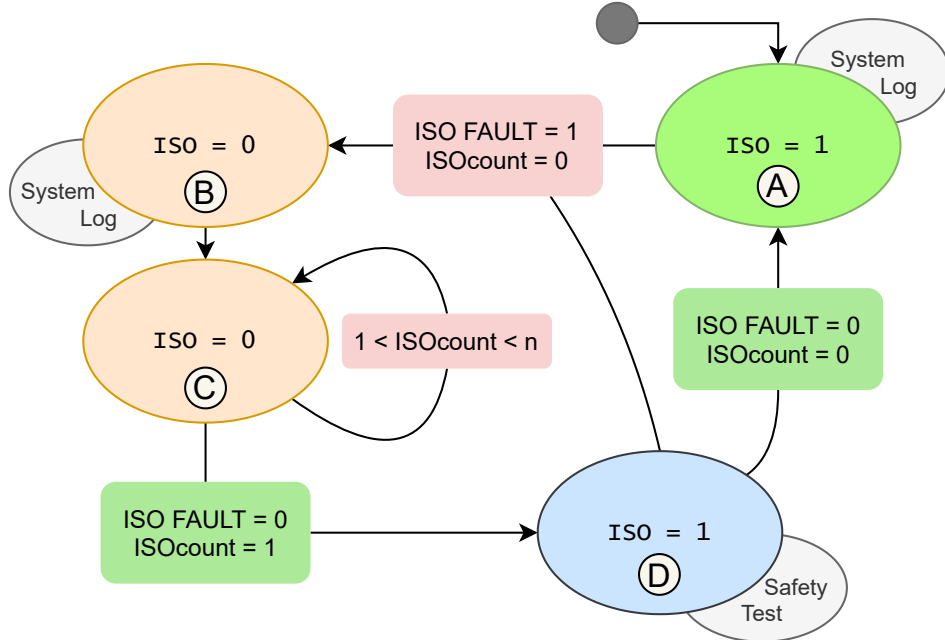


Figure 3.4: Isolation (ISO) control finite state machine

The finite state machines (FSMs) in figures 3.4 and 3.6 determine how the BMS handles various combinations of fault conditions. The FSM in figure 3.6 also handles charging control. The variables CHG and ISO are the state of the MOSFETs. The variables ISOcount and CHGcount provide a *cool-down* period after a fault before the checks if the fault has been resolved. This system allows the BMS to protect itself from harm, while still recovering from temporary faults.

When a new fault occurs, ISOcount and CHGcount are set to their maximum value, n (100). After which, the variables count down until the safety test is performed. If a fault occurs when the count has not yet been cleared, the countdown is reset to $n-1$. Both ISOcount and CHGcount follow the same logic in equation 3.5, but referring to the appropriate fault conditions.

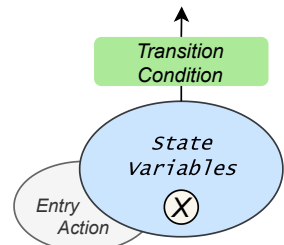


Figure 3.5: Finite State Machine Legend

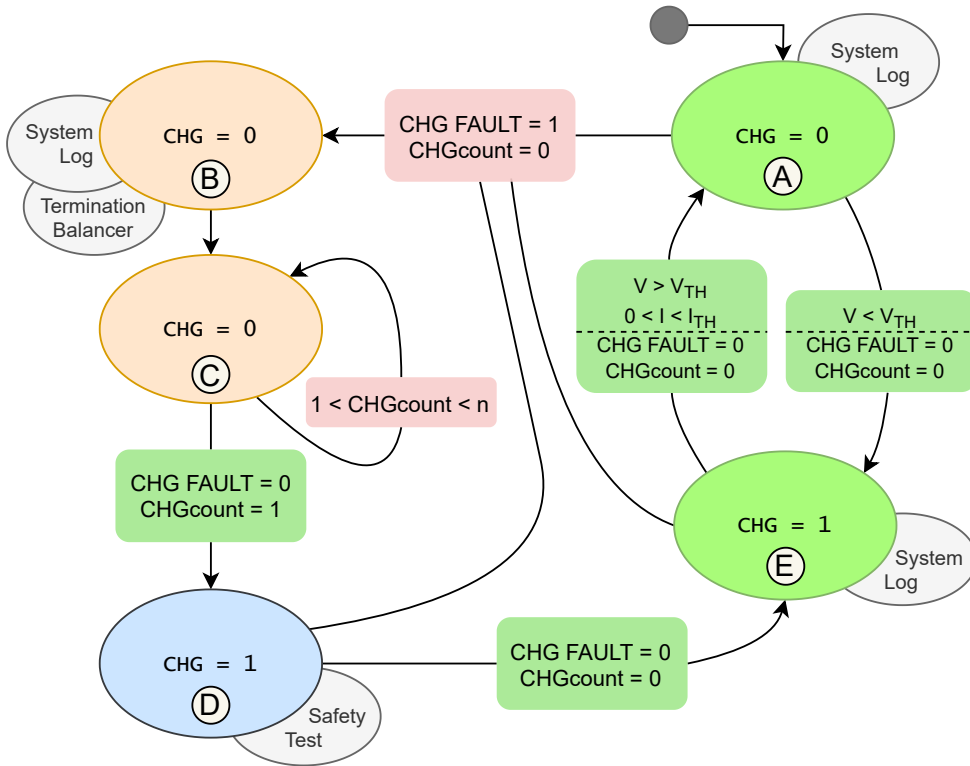


Figure 3.6: Charging (CHG) control finite state machine

$$ISOcount = \begin{cases} n, & ISOfault = 1, ISOcount = 0 \\ n - 1, & ISOfault = 1, 0 < ISOcount < n \\ ISOcount - 1, & ISOfault = 0, 0 < ISOcount < n \end{cases} \quad (3.5)$$

The charging control cycle in figure 3.6 occurs in the states *A* and *E*. The system begins in state *A* with the charger disconnected. Assuming there are no faults, if the voltage of all cells is below the threshold voltage $V_{TH} = 4150mV$ set by the manufacturer, then the system will transition into state *E* and the charger will be connected. If the charging current falls below the threshold, i.e. $I_{TH} = 100mA$, and the voltage of all cells is above the threshold, then the system will transition into state *A* and the charger will be disconnected.

Both FSMs handle faults in the same manner through states *B* to *F* in both diagrams. To illustrate the function, consider the case of the ISO FSM during an

over temperature fault:

- (A) → (B) : An *over temperature* fault caused ISO to be switched off and a system log to be written.
- (B) → (C) : B will always transition to C
- (C) → (C) : The *over temperature* persists, so ISOcount remains at $n - 1$.
-
- (C) → (C) : The *over temperature* fault has resolved and ISOcount is decremented.
-
- (C) → (D) : Safety test momentarily reconnects ISO and rechecks for faults.
- (D) → (A) : Safety test did not detect a fault, ISO is reconnected and system log is written

FSMs handle momentary, recurring and persistent faults equally well. After a momentary fault the system will recover, but a recurring or persistent fault will prolong the cool-down period for as long as required. The under voltage cutout of the battery operates in this way, the cool-down period is extended until the battery is charged. Once the battery is depleted to its minimum voltage, an *ISO FAULT* is triggered which disables discharging current. The variable ISOcount will remain at its maximum until the battery has been recharged. Hysteresis is added by increasing the lower cutoff voltage by 500mV. This gives a smooth cutoff even with varying cell overpotentials.

3.3 Measurement Calibration

Accurate and precise measurement of the cell voltages and currents is essential for good performance. As discussed in section 3.2, the voltage measurement circuits are susceptible to scaling errors and common mode signal intrusion from minor imperfections in the hardware. To a lesser degree, the current measurement system is also susceptible to scaling errors. Fortunately, the systems and errors are linear so they can be minimised through calibration.

Both offset and scaling errors can be handled simultaneously by equating the output codes from the ADC to the cell voltages they are measuring, or determining the inverse transfer function of the resistor network and ADC. The inverse transfer function can be seen in equation 3.6, where ADC is the output code from the ADC, G_{diff} is the differential scaling factor, V_{CM} is the voltage at the negative terminal of the cell, G_{CM} is the common mode voltage scaling factor and $Offset$ is a constant offset. G_{diff} is the result of the ratio of the resistor dividers, while G_{CM} is the result of the inequality of paired dividers. This equation is derived from the input network and ADC, and the assumption of linearity the system.

$$V_{cell} = ADC \times G_{diff} + V_{CM} \times G_{CM} + Offset \quad (3.6)$$

Although resistor dividers of matching ratios were used to connect the positive and negative terminals of each cell to the ADC, the tolerances of the resistors results in a significant common mode signal in the output. The proportion of this signal is evaluated with the standard measure of common mode rejection ration, or CMRR, was discussed in section 3.2.2.

Equation 3.6 is a linear equation in three dimensions. The values for the parameters were determined for each cell channel by applying a common mode voltage from ground to the negative cell holder terminal and a differential voltage between the two cell holder terminals, and recording the output code of the ADC. The common mode and differential voltages were measured with a multimeter, and the ADC codes were recorded and averaged of 80 samples. The test was repeated for each cell channel; for differential voltages from 2V to 4.5V in 0.1V increments and for common mode voltages from 0V to the maximum possible for each channel in varying steps. A selection of the tests for the B4 channel are shown in figures 3.7 and 3.8. Note that due to the finite resolution of the ADC, the output codes in figure 3.8 follow a the staircase function of the ADC.

The relationship in equation 3.6 is a plane in the V_{cell} , ADC V_{CM} spaces. A least squares fit in three dimensions was used to find the plane which best represented the observations.

Current measurements made with the INA219 were also assumed to follow a similar transfer function and were calibrated with a similar method. The distinction

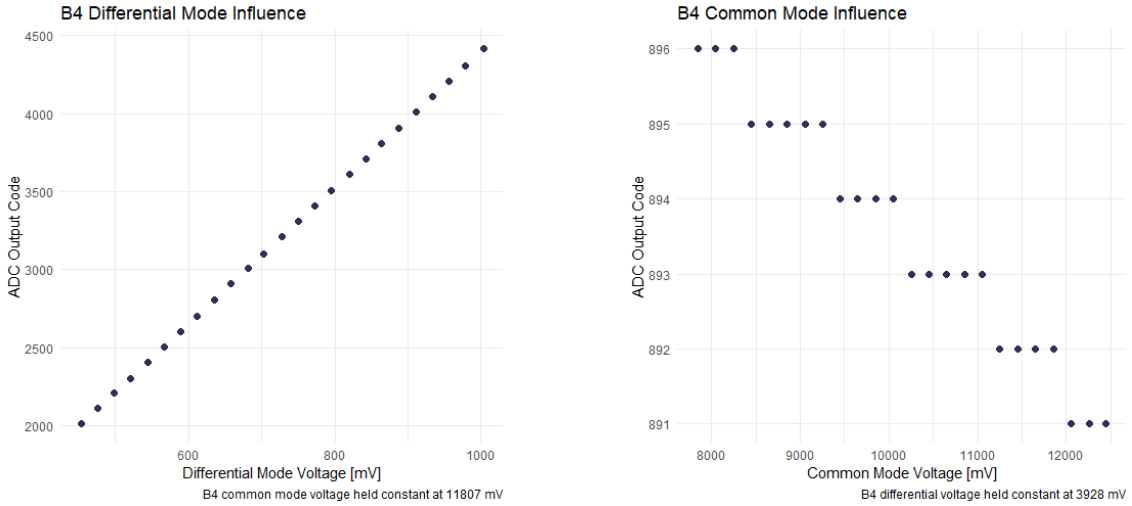


Figure 3.7: The influence of differential mode voltage on the output codes of the ADC

Figure 3.8: The influence of common mode voltage on the output codes of the ADC

being that having a specified CMRR of 120dB means that any common mode term of equation 3.6 would be insignificant, so it was neglected.

Cell B1 shares its negative terminal with ground so will never experience any common mode voltage, so equation 3.6 was also simplified. This simplification was a motivation for using high-side current sensing.

Table 3.2 shows the values for the model parameters for each channel of the ADC and the current sensor. All of the models fitted the data perfectly, with R^2 values greater than 0.999, and minimal $\sigma_{resit.}$.

The CMRR before calibration is included in table 3.2 and was calculated directly from the model parameters: $CMRR = 10 \log(G_{diff}/G_{CM})$. Given the closeness of the linear regressions, it is not be meaningful to remeasure the CMRR after calibration.

After calibration the system was verified against the multimeter used for calibration. The values of both were sufficiently close across the range of differential and common mode voltages. Here sufficiently means that the difference was within the normal fluctuations of $\sim \pm 5\text{mV}$.

	B1	B2	B3	B4	INA
Offset	-2.07 mV	-3.52 mV	-0.41 mV	10.50 mV	-0.82 mA
G_{diff}	1.08	2.20	3.35	4.37	0.098
G_{CM}	NA	-4.90e-03	-2.20e-03	1.80e-03	NA
CMRR [dB]	NA	26.53	31.84	33.86	NA
$\sigma_{resid.}$	0.6650	1.723	4.259	9.199	5.5052

Table 3.2: ADC and INA inverse transfer function parameters and residual standard error. G_{diff} and G_{CM} have units of $\frac{mV}{bit}$ or $\frac{mA}{bit}$ as appropriate, $\sigma_{resid.}$ has units mV or mA as appropriate. All models have $R^2 > 0.999$

3.4 Handling of Uncertainties

It is important to the operation of the BMS that the MCU have reliable information on the state of the cells. Although no single component in the BMS measurement systems has unacceptable accuracy, it is not guaranteed that after calibration and further calculations that the final values are acceptable. This section deals with identifying sources of uncertainty and how that uncertainty propagates.

Assumptions and definitions

Uncertainty in this context follows the common definition of the standard deviation of a repeated measurement. In some cases the uncertainty is specified by the manufacturer of a device, in other cases the measurement was repeated multiple times and the mean and standard deviation of that measurement are used as the best value and uncertainty of the quantity. It is assumed that the uncertainty in all quantities in this analysis are independent.

The absolute uncertainty of a quantity x is represented as δx and relative uncertainty is represented as $\frac{\delta x}{x}$.

3.4.1 Propagation of Uncertainty

It has been shown that for a function q , the uncertainty of its arguments propagates as follows shown in equation 3.7 [34]. Each partial derivative in the equation for $\delta q(x, \dots, z)$ is evaluated with the values x, \dots, z of the original equation for $q(x, \dots, z)$. Intuitively, the partial derivatives in equation 3.7 can be thought of as the sensitivity of the original function to variation in the variable in question, and the product with the uncertainty of that variable represents the possible variation of that variable.

$$q(x, \dots, z) \rightarrow \delta q = \sqrt{\left(\frac{\partial q}{\partial x}|_{\bar{x}, \dots, \bar{z}} \delta x\right)^2 + \dots + \left(\frac{\partial q}{\partial z}|_{\bar{x}, \dots, \bar{z}} \delta z\right)^2} \quad (3.7)$$

For cases such as the sum, product, factor and index, the simplified equations can be seen in table 3.3.

Operation	Equation	Propagated Uncertainty
Multiplication by a factor:	$q = Bx$	$\delta q = B \delta x$
Sum and difference:	$q = x + y - u - \dots$	$\delta q = \sqrt{(\delta x)^2 + (\delta y)^2 + (\delta u)^2 + \dots}$
Product and quotient:	$q = \frac{x \times z}{u}$	$\frac{\delta q}{ q } = \sqrt{\left(\frac{\delta x}{ x }\right)^2 + \left(\frac{\delta z}{ z }\right)^2 + \left(\frac{\delta w}{ u }\right)^2}$
Raised to a power:	$q = x^n$	$\frac{\delta q}{ q } = n \frac{\delta x}{ x }$

Table 3.3: Uncertainty propagation in common formulas [34]

3.4.2 Sources of Uncertainty

All measurements made in this project have an accompanying uncertainty. Thermal noise, nearby effects of components, calibration tolerances and system non linearity

are conspicuous sources of uncertainty.

Measurements are made in five separate ways in the calibration and operation of the system. The ADC makes measurements of cell voltages through a resistor network, the MCU's ADC measures the voltage across NTC thermistors, the INA219 measures the voltage across a shunt resistor, and a digital multimeter (DMM) was used to calibrate the ADC and resistor network and to calibrate the INA219's transfer function.

When a measurement of voltage or current is taken, the uncertainty is the combination of uncertainty of the device taking the measurement and noise in the value being measured. For example, the output of the ADC represents the voltage at its input, noise on its input and uncertainty in its transfer function both contribute to the output uncertainty. Often the noise in the measurement is insignificant or cannot be determined, so it is neglected.

Figures 3.10 and 3.9 describe how values and their uncertainties propagate from their source to the final voltage or current. The function Lm represents the linear regression in section 3.3. $Bin2mA$ and $Bin2mV$ are the inverse transfer functions, similar to the one shown in equation 3.6, for calculating the voltage or current from the binary codes. The function Σ represents the way that the lower cell voltages are summed to calculate the common voltage of a cell. These diagrams give an overview of the relationships, in the following sections the uncertainties are isolated and quantified.

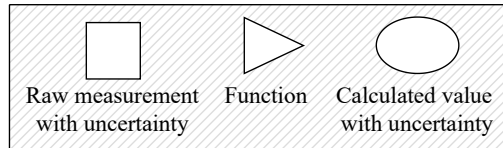


Figure 3.9: Legend for figure 3.10.

Uncertainty of the MAX11616 ADC

The MAX11616 ADC measures an input voltage and produces a corresponding binary code, represented as . It has a specified differential linearity error of ± 1 LSB, that is the deviation in output codes from an ideal ADC. The resolution of the ADC is 1 mV/LSB The input to the ADC, V_{in} , contains noise from the resistor network and nearby effects. This noise was quantified by repeated sampling, its standard deviation was found to be approximately 0.5LSB. The resolution of the ADC fundamentally limits its sensitivity to noise below this amount. Considering

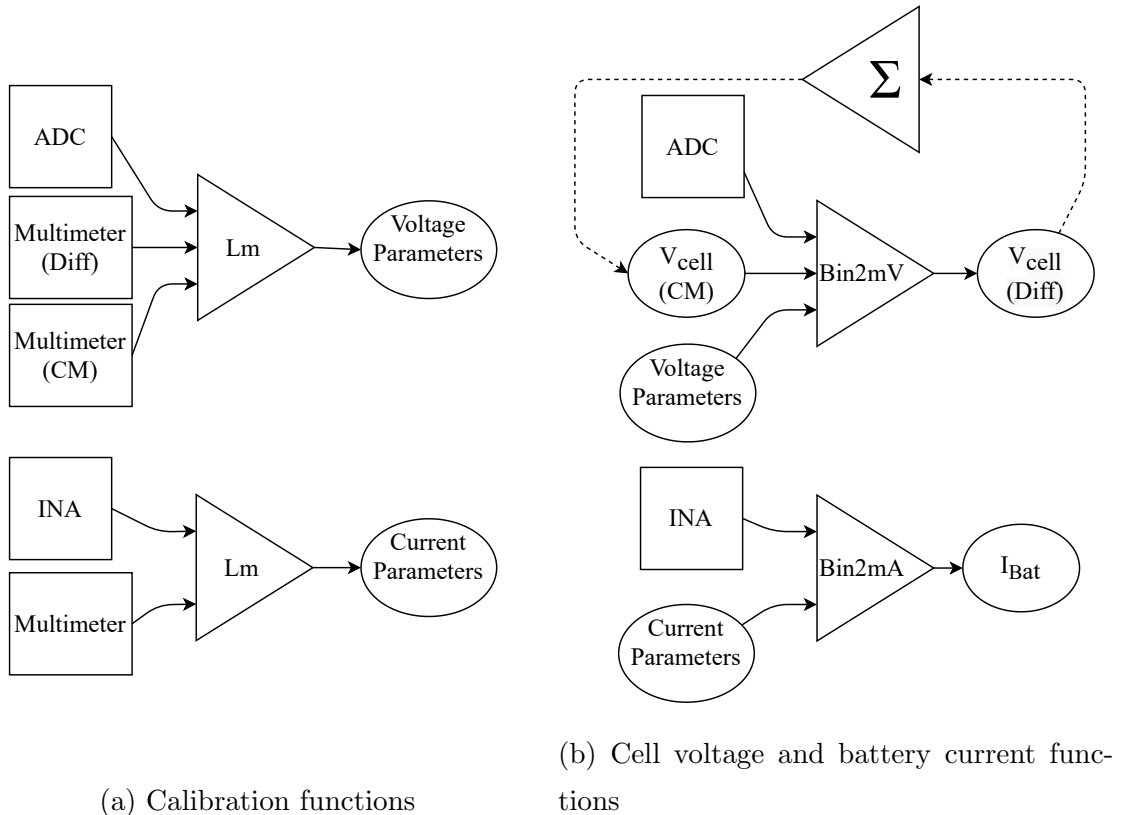


Figure 3.10: A functional overview of BMS calculations.

the ADC as a system with a transfer function shown in equation 3.8, where $G_{ADC} = 1000 \pm 1 \left[\frac{\text{bits}}{V} \right]$, and $V_{in} = V_{in} \pm 5 \times 10^{-4} [V]$.

$$ADC(V_{in}) = G_{ADC} * V_{in} \quad (3.8)$$

From the rules for propagation of uncertainty in table 3.3, the relative uncertainty in the ADC codes is shown in equation 3.9

$$\begin{aligned}\frac{\delta ADC}{ADC} &= \sqrt{\left(\frac{1}{1000}\right)^2 + \left(\frac{0.0005}{V_{in}}\right)^2} \\ &= \sqrt{\left(\frac{1}{1000}\right)^2 + \left(\frac{0.5}{ADC}\right)^2}\end{aligned}\quad (3.9)$$

Uncertainty of the INA219 Current Sensor

Similar to the MAX11616, the INA219 contains an ADC, it measures the voltage across a 0.1Ω shunt resistor to determine the system current. It is specified to have a differential linearity error of ± 0.1 LSB, which with a resolution of $10 \mu V/LSB$, corresponds to a $\pm 1 \mu V$ non linearity, or a relative non linearity of $\frac{\delta INA}{INA} = \frac{0.1}{INA}$, where INA is the output code from the device. The manufacturer also specified a relative current measurement error of $\pm 0.5 \%$.

Comparing the two specification, the uncertainty due to differential non linearity is less than 10% of current measurement error for input voltages greater than ± 20 mA. Current measurements within ± 20 mA are not of great importance in the system. Although the manufacturer does not specify their definition of current measurement error, even if it does not include ADC non linearity, it is the dominant component of the device's uncertainty for practically all of its operating range. The noise on the input to the INA129 can also be quantified in the same manner as for the MAX11616. Figure 3.11 shows the counts of output codes from the INA219 for 2560 samples during a 50 second period. The $10 \mu V$ resolution is easily able to resolve the noise in the system to have an uncertainty of 1.471 bits, or $147.1 \mu A$.

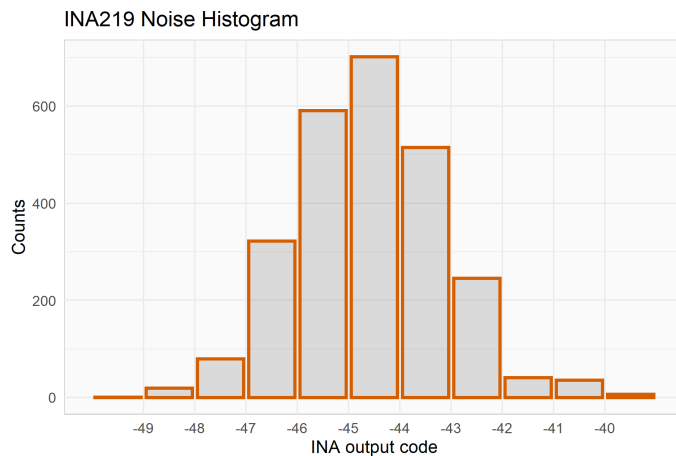


Figure 3.11: Histogram of noise as measured in the output codes of the INA219

Similar to the case with the MAX11616, considering the INA219 as a process with a transfer function shown in equation 3.10. Where $G_{INA} = 10^5 \pm 0.5\% \left[\frac{bits}{Volt} \right]$ and the voltage across the shunt resistor V_{in} has an uncertainty of $\pm 14.71 \mu V$.

$$INA(V_{in}) = G_{INA} * V_{in} \quad (3.10)$$

The relative uncertainty associated with the output code is shown in equation 3.11, and was derived using the relationships in table 3.3.

$$\frac{\delta INA}{INA} = \sqrt{0.005^2 + \left(\frac{14.71 \times 10^{-6}}{V_{in}} \right)^2} \quad (3.11)$$

Uncertainty in Voltmeter Measurements

A voltmeter was used in the process of calibrating the MAX11616 ADC and the resistor network. Section 3.3 details the procedure. The common mode and differential voltages were measured with the voltmeter and the output code of the ADC was recorded. The voltmeter used was an ANENG AN8008 multimeter. Its had a resolution of 1mV or 10mV for the voltages ranges $0V \rightarrow 10V$ or $10V \rightarrow 100V$ respectively. With a specified accuracy of $\pm(0.5\% + 3 \times \text{resolution})$. Equation 3.12 describes the relative uncertainty in the reading from the multimeter.

$$\frac{\delta V}{V} = \begin{cases} \pm (0.005 + 0.003 \times V) & \text{if } |V| < 10, \\ \pm(0.005 + 0.03 \times V) & \text{if } |V| > 10 \end{cases} \quad \text{V in Volts} \quad (3.12)$$

The voltages measured with multimeter are subject to system noise. The noise as seen by the ADC is taken as an approximation for the noise seen by the multimeter. The relative uncertainty specified by the manufacturer of the multimeter is many orders of magnitude greater than the system noise for all practical values. Therefore the the system noise can be neglected in this case.

Uncertainty in Ammeter Measurements

The INA219 was calibrated using the current measurement of the ANENG AN8008 multimeter. Following the same logic as for voltage measurements, the relative uncertainty is shown in equation 3.13.

$$\frac{\delta I}{I} = \begin{cases} \pm (0.01 + 0.0003 \times I) & \text{if } |I| < 1, \\ \pm(0.01 + 0.003 \times I) & \text{if } |I| > 1 \end{cases} \quad I \text{ in Amps} \quad (3.13)$$

Uncertainty in the STM32 ADC temperature measurement

Cell temperatures were measured by measuring the output voltages from a set of voltage dividers containing NTC thermistors placed against the cells. The internal ADC of the MCU, an STM32F103C8T6, read the relevant voltages. The MCU's ADC was specified to have a *total unadjusted error* of ± 2 LSB, with a resolution of approximately $0.8 \frac{mV}{LSB}$.

The noise on each of the four ADC channels can be seen in figure 3.12 as the sd , or standard deviation of the counts.

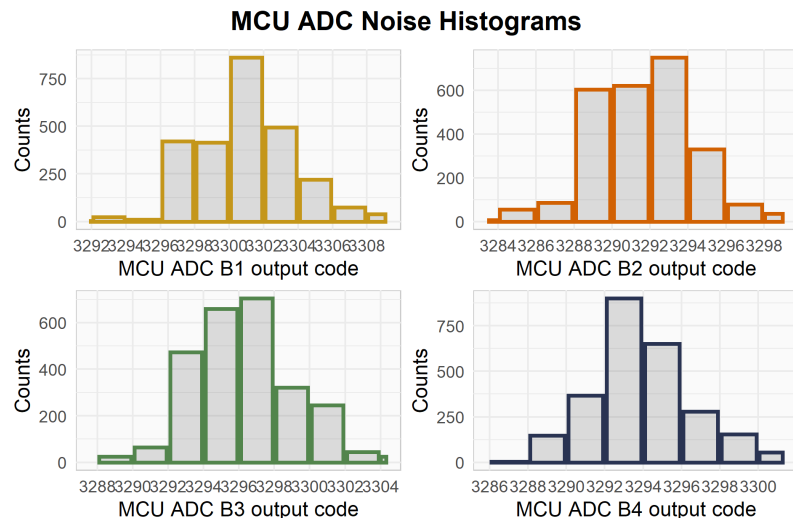


Figure 3.12: Histograms of output codes from the MCU ADC

Cell	B1	B2	B3	B4
μ	3301	3291	3296	3294
σ	2.86	2.59	2.79	2.57

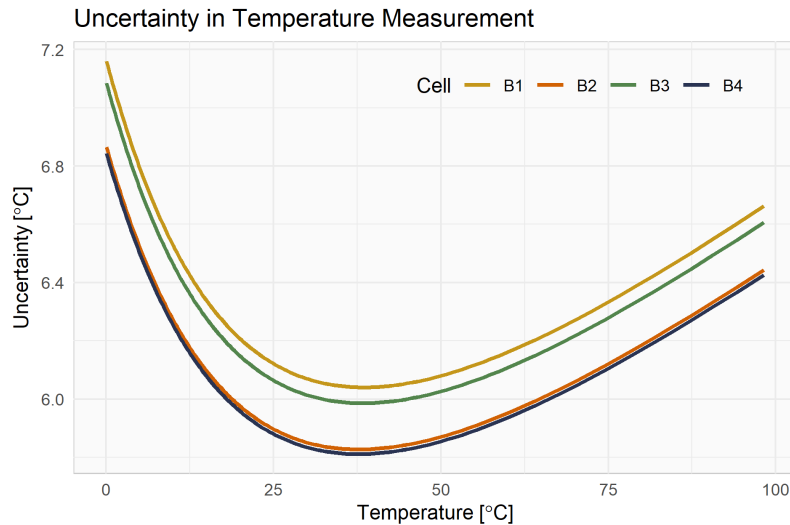


Figure 3.13: Uncertainty in cell temperatures, according to equation 3.14

3.4.3 Uncertainties of Derived Quantities

Uncertainty in Temperatures

Cell temperature is calculated using equation 3.4, and the uncertainty can simply be derived using the equations in 3.3, as shown in equation 3.14. Using the value from figure 3.12, the uncertainty in cell temperatures is shown in figure 3.13

$$\delta T_{cell} = \sqrt{\left(\frac{\delta R_{lower}}{R_{lower}}\right)^2 + \left(\frac{\delta V_{ADC}}{V_{ADC}^2}\right)^2 + \left(\frac{\delta R_0 e^{-\frac{B}{T_0}}}{R_0}\right)^2} \times \frac{B}{\ln \frac{R_{NTC}}{r_\infty}} \quad (3.14)$$

Uncertainty in Cell Voltages and Currents

The raw voltage measurements made on the BMS are scaled and translated to reverse the transform from the measuring process, as described in section 3.3 and figure 3.10.

The uncertainty in the final value for the cell voltage, according to equation 3.6, is shown in equation 3.15, and was derived using the relationships in table 3.3.

The values and uncertainties for ADC and V_{CM} , the uncertainty terms δG_{diff} , δG_{CM} and $\delta Offset$ must be calculated.

When fitting by least squares, certain statistics can be derived, such as the standard error shown in table 3.2. Unfortunately this quantity describes the residuals, or difference between the fitted model and observations, it does not describe the uncertainty in any parameter or the propagation of errors.

$$\delta V_{cell} = \sqrt{(\delta ADC \times G_{diff})^2 + (\delta G_{diff} \times ADC)^2 + (\delta V_{CM} \times G_{CM})^2 + (\delta G_{CM} \times V_{CM})^2 + (\delta Offset)^2} \quad (3.15)$$

The uncertainty of the parameters can be derived from first principals. Equation 3.7 dictates how errors will propagate for any continuous function with continuous derivatives. The functions used to calculate the parameters of a two dimensional relationship by least squares are shown in equations 3.16, where x and y represent the observations x_1, \dots, x_n and y_1, \dots, y_n , all sums are over $i = 1 \rightarrow n$ and \bar{x}, \bar{y} are the means of x and y .

$$y = a + b \times x$$

$$a = \frac{\bar{y} \sum x_i^2 - \bar{x} \sum x_i y_i}{\sum x_i^2 - n \bar{x}^2}$$

$$b = \frac{\sum x_i y_i - n \bar{x} \bar{y}}{\sum x_i^2 - n \bar{x}^2} \quad (3.16)$$

The partial derivatives of a and b with respect to x_j and y_j , $j \in [1, n]$, can be calculated by the chain, product and quotient rules, and are shown in equations 3.17

$$\frac{\partial a}{\partial x_j} = \frac{\left[2x_j \sum y_i - y_j \sum x_i - \sum x_i y_i \right] \left[n \sum x_i - (\sum x_i)^2 \right]}{- \left[\sum x_i^2 \sum y_i - \sum x_i \sum x_i y_i \right] \left[2nx_j - 2 \sum x_i \right]} \quad (3.17)$$

$$\frac{\partial a}{\partial y_j} = \frac{\sum x_i^2 - x_j \sum x_i}{n \sum x_i^2 - (\sum x_i)^2} \quad (3.17a)$$

$$\frac{\partial b}{\partial y} = \frac{\left[ny_j - \sum y_i \right] \left[n \sum x_i^2 - (\sum x_i)^2 \right]}{- \left[n \sum x_i y_i - \sum x_i \sum y_i \right] \left[2nx_j - 2 \sum x_i \right]} \quad (3.17b)$$

$$\frac{\partial b}{\partial y_j} = \frac{nx_j - \sum x_i}{n \sum x_i^2 - (\sum x_i)^2} \quad (3.17c)$$

Equation 3.7 contains the partial derivatives of the function evaluated with the values of x, \dots, z used to calculate $q(x, \dots, z)$. The functions for least square fit parameters in two dimensions have $2 \times n$ arguments, for all x and y observations. The uncertainty of a is shown in equation 3.18, with the other parameters following the same form.

$$a(x_1, \dots, x_n, y_1, \dots, y_n)$$

$$\rightarrow \delta a = \sqrt{\sum_{i=1}^n \left(\frac{\partial a}{\partial x_i} \Big|_{x,y} \delta x_i \right)^2 + \sum_{i=1}^n \left(\frac{\partial a}{\partial y_i} \Big|_{x,y} \delta y_i \right)^2} \quad (3.18)$$

A two dimensional linear model was used for B1 and the current sensor. Channels B2-4 used a three dimensional model that included a common mode voltage parameter, denoted as c . The derivation of the equations for parameters a , b and c can be found in the appendix. Due to the number of terms involved, a program was written to perform the analytical partial differentiation of each equation.

The outcome of these calculations are shown in table 3.4 figure 3.14. The table shows the uncertainty in the model parameters and the figure shows the final relative uncertainties for each cell voltage across their operating range.

The relative magnitudes of the uncertainties could be somewhat counter intuitive, one might expect uncertainty to increase from B1 to B4, as the minimum resolution increases. Naturally the explanation lies in the values in equation 3.15 and in the uncertainties of each parameter. Firstly, for identical cell voltages, the value of ADC is smaller for higher cells, as caused by the voltage dividers. Secondly, cells B1 and B2 have offset parameters, $\delta Offset$, four to seven times larger than B3 and B4. Finally, the common mode gain uncertainty, δG_{CM} , of B2 is more than double that of B3 or B4. The last two issues, relating to parameter uncertainty, are likely caused by the simple fact that models for higher cells used more observations for common mode voltages over a greater range.

Absolute Uncertainties:

	B1	B2	B3	B4	INA
a (G_{diff})	1.41E+01	1.88E+01	3.18E+00	2.41E+00	1.32E+00
b (G_{CM})	5.10E-03	8.73E-03	4.92E-03	5.92E-03	2.84E-04
c ($offset$)	NA	2.49E-03	6.36E-04	4.34E-04	NA

Relative Uncertainties [%]:

	B1	B2	B3	B4	INA
a (G_{diff})	-680.17	-533.25	-782.65	22.99	-160.95
b (G_{CM})	0.47	0.40	0.15	0.14	0.29
c ($offset$)	NA	-50.80	-28.92	24.17	NA

Table 3.4: Absolute and relative uncertainties of model parameters.

Individual cell currents are the sum of the battery current and the current through the shunt resistor corresponding to the cell, as seen in equation 3.20. The piecewise uncertainty is shown in equation 3.20

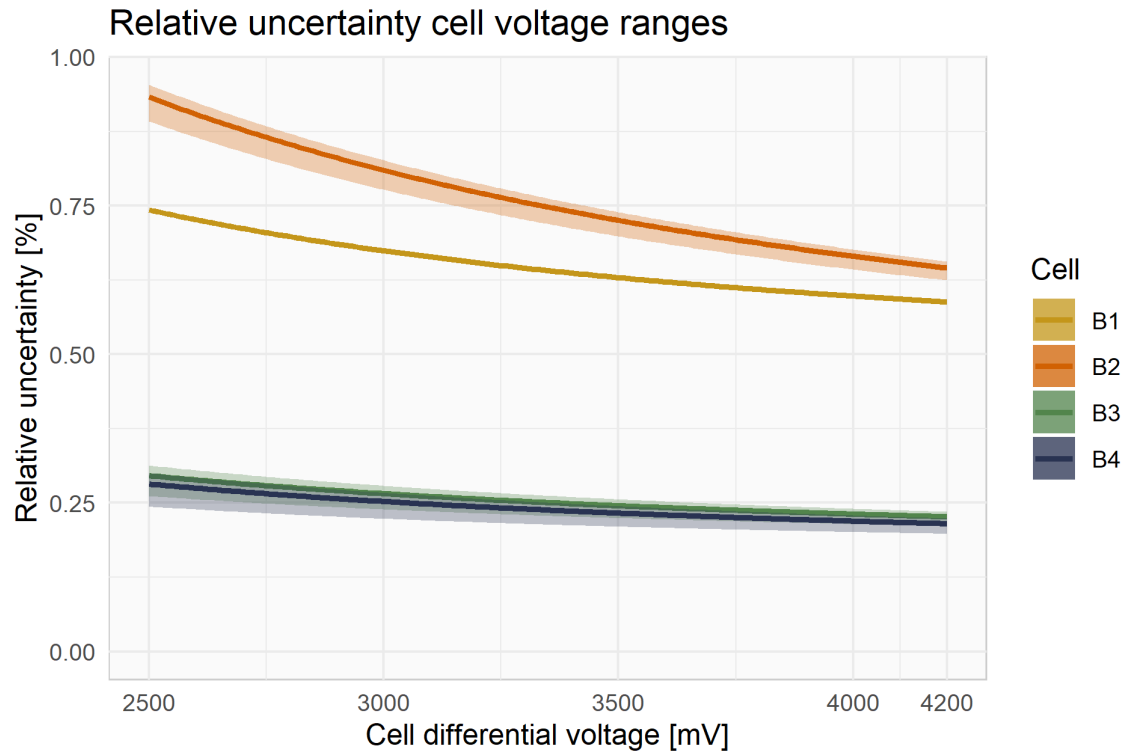


Figure 3.14: The range of relative uncertainties for varying cell voltages and differential voltages. Lines represent a constant common mode voltage of 3.7V, where applicable. Shaded regions show the extent for maximum or minimum common mode voltage

$$I_{cell} = \begin{cases} I_{Bat}, & \text{shunt inactive} \\ I_{Bat} + \frac{V_{cell}}{R_{shunt}}, & \text{shunt active} \end{cases} \quad (3.19)$$

$$\delta I_{cell} = \begin{cases} \delta I_{Bat}, & \text{shunt inactive} \\ \sqrt{(\delta I_{Bat})^2 + \left(\frac{\delta V_{cell}}{R_{shunt}}\right)^2 + \left(\frac{\delta R_{shunt} \times V_{cell}}{R_{shunt}^2}\right)^2}, & \text{shunt active} \end{cases} \quad (3.20)$$

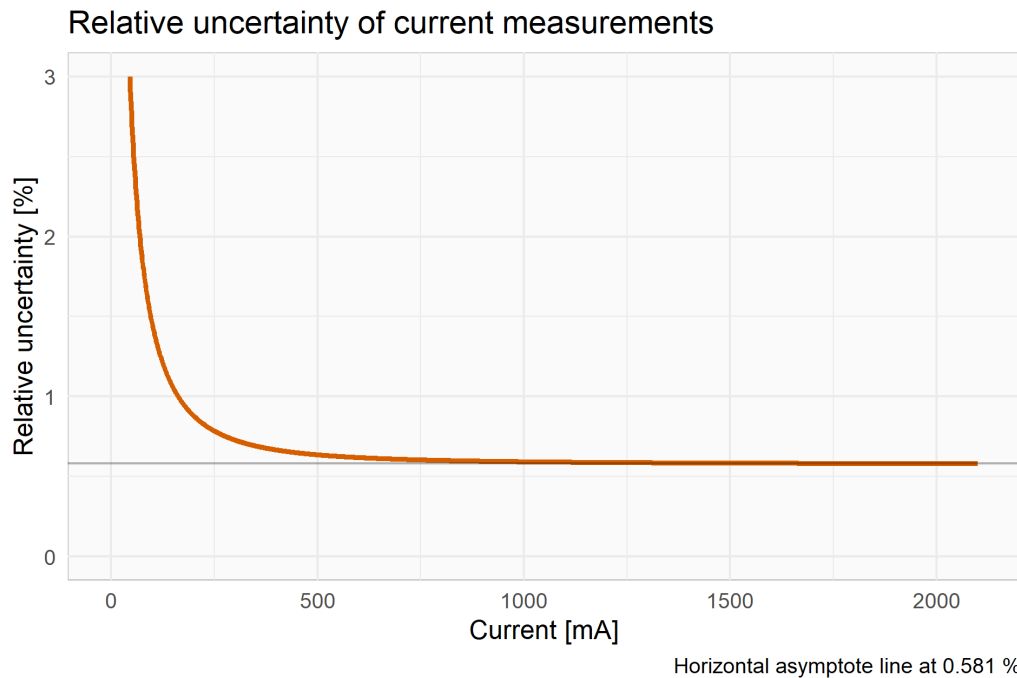


Figure 3.15: The range of relative uncertainties for varying battery currents

3.5 Function Validation

The design and construction of the charging and safety systems of the BMS are critical to operation and require proper planning, but are simple in effect. The finite state machines in figures 3.6 and 3.4 describe how the BMS handles the charging and safety systems. There are many permutations of possible events in these systems, but most are handled in the same manner. For the sake of conciseness, only two example cases are shown in this section.

Managing of charging and voltage limits is shown in figure 3.16. The first plot shows the voltage of all four cells during a test for section 4.3. The battery is discharged until empty at $\sim 180\text{mV}$, then is recharged from $\sim 150\text{mV}$ to $\sim 430\text{mV}$. The points T1, T2 and T3 have been highlighted as these are when the transitions in the FSMs occur. The second plot shows the states of the CHG and ISO MOSFETs, note that CHG is on all the way until T3, while ISO is only off between T1 and T2. The transitions are shown in the figure 3.17 and 3.19. Between T1 and T2 in figure 3.16, the ISO FSM remains in state C. Recall that an exception is made for *under voltage* faults, the fault causes the minimum voltage to be increased by

500mV. Connection of the charger and the rise in voltage allows the FSM to proceed through *D* and *E* to finally reach *A* where the system is unisolated. T3 occurred when all cell voltages were above the threshold, 4150mV, and the charging current was less than 100mA. As shown in figure 3.19, CHG was disconnected.

All of the fault conditions and charging situations have been verified to function as intended. The events shown in figure 3.16 are typical of the system's performance.

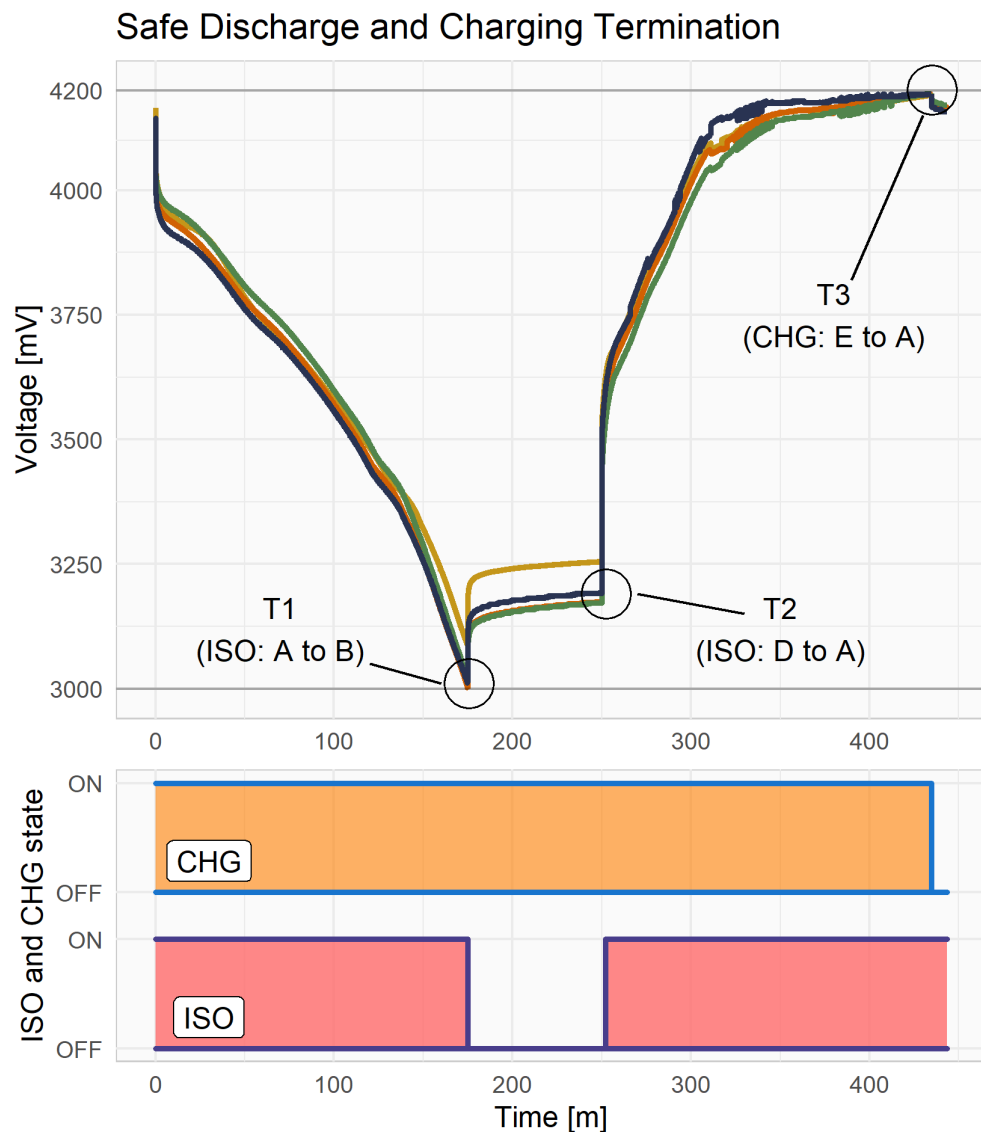


Figure 3.16

An example of overcharge protection is shown in figure 3.18. As can be seen, the

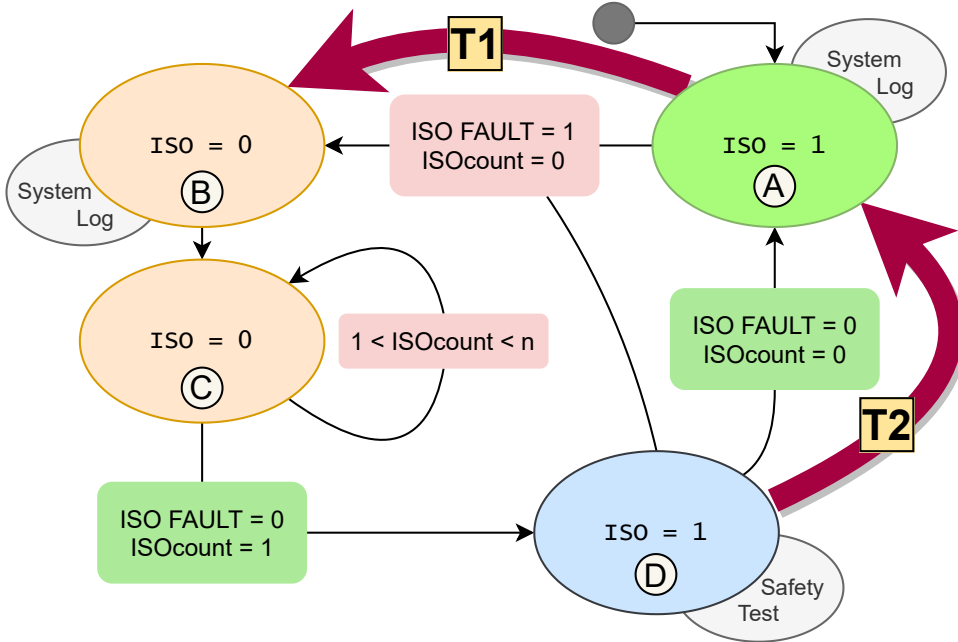


Figure 3.17: Isolation (ISO) control finite state machine with transitions T1 and T2

cells are almost charged, but are not balanced, cell B1 is not above the threshold voltage of 4150mV. When the voltage of cell B4 exceeds 4200mV, the FSM transitions from *G* to *B* and the charger is disconnected, causing the drop in cell voltages. This transitions and the *over voltage* fault triggers the `Termination_balancer` function, as explained in section 4.1.1, shunts cell B4 to reduce the imbalance. As the *over voltage* fault is removed by disconnecting the charger, the CHGcount variable is decremented and the FSM passes through states *C* to *F* until the charger is reconnected at T5.

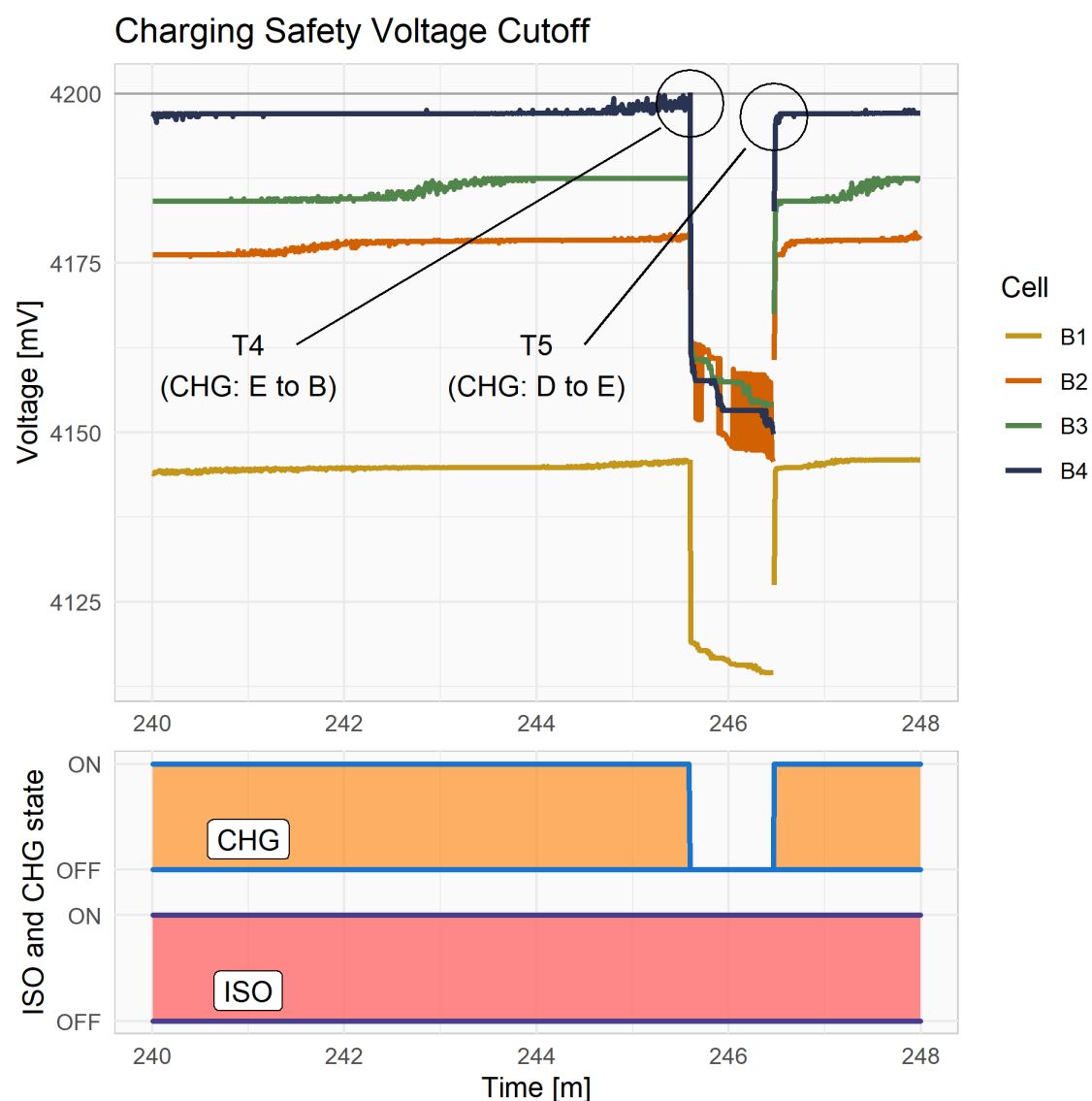


Figure 3.18: BMS over voltage protection

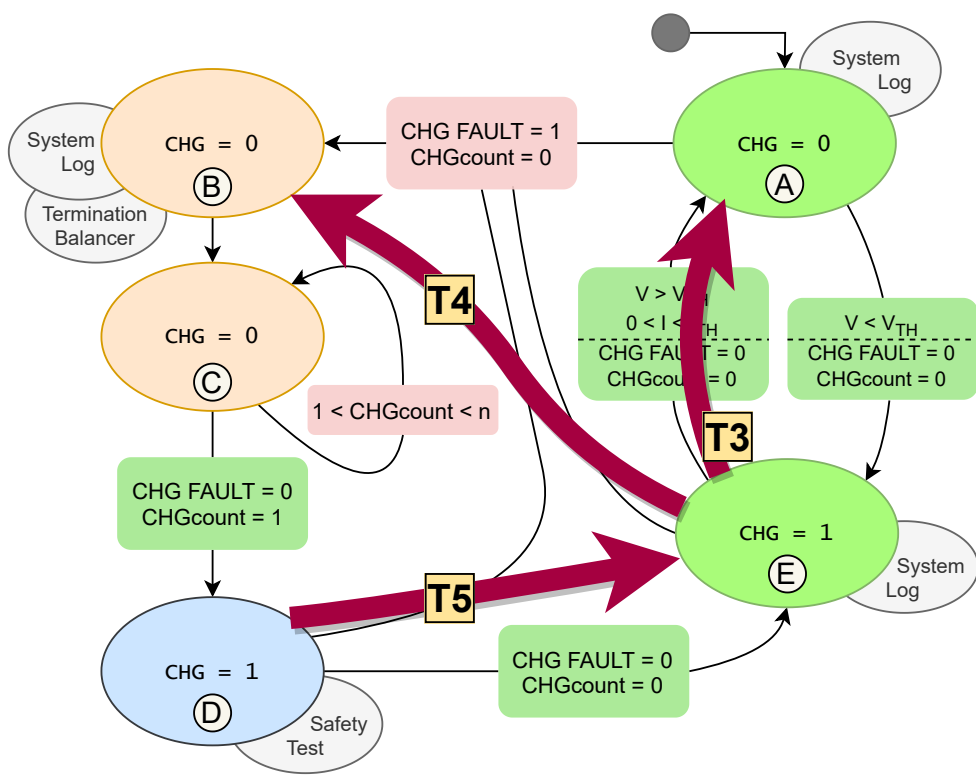


Figure 3.19: Charging (CHG) control finite state machine with transitions T3, T4 and T5

Chapter 4

Cell Balancing System

As discussed in sections 1.1 and 3.1, the application of this project requires a reliable battery with a maximised power density and which can charge in minimal time. These are driven by the low cost of charging power and the high value of operational time of the system. As described in section 2.2.3, balancing cell voltages is essential in multi-cell battery packs, and several circuits are compared in the literature. Given the economics of the application system, a passive balancing system was chosen. Passive balancing has a simple structure, although it has a lower efficiency than alternatives, the low cost of power reduces the penalty. As discussed in the section 2.5, Lievre's method will be used to improve the efficacy of the balancing system. This will be covered in detail in section 5.3.2.

4.1 Design and Implementation

Passive balancing works by diverting a portion of a cell's charging current through a resistor to reduce its charging rate. The hardware requirements are one shunt resistor and switch per cell. Figure 4.1 shows the circuit used in the BMS. The shunt resistance is a compromise between maximising the effectiveness of the balancing system and minimising the additional space and thermal requirements. A compromise of $40\ \Omega$ was selected, giving a peak power of less than 0.5W when shunting a fully charged cell. A resistor as small as a 1W 2045 surface mount resistor can be used, with its 5mm by 11.5mm footprint.

Beyond the simple hardware, an appropriate control algorithm needs to be de-

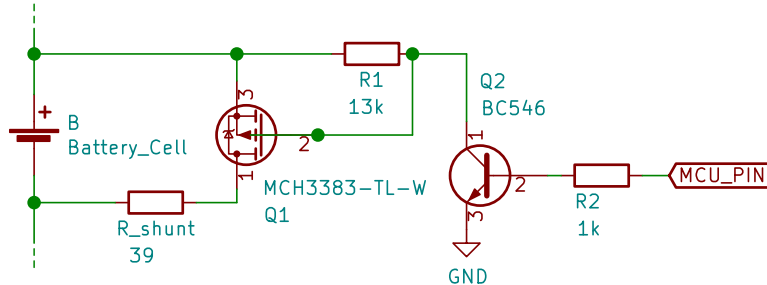


Figure 4.1: Cell and balancing shunt resistor

vised. There are many ways in which cell imbalance can manifest, differing capacities, SoC, or overpotentials for example. The control algorithm may not be able to determine why or even if an imbalance is present always.

The central assumptions in designing the balancing algorithm were as follows:

- LiBs cannot tolerate being overcharged.
- The actual SoC and capacity of each cell is not known.
- It is not guaranteed that any cells will have the same capacity, SoC or internal impedance.
- The voltage of a cell is only indicative of its SoC.
- To maximise battery energy density, all cells should be fully charged within the specified voltage tolerance (50mV).
- The minimum charge time is set by cell with the greatest capacity to be charged (this does not hold for active balancing).

Following these assumptions, an ideal algorithm would apply shunts to the all cells but the one with the greatest capacity to be charged, such that they all become fully charged simultaneously. As the true capacity to be charged is not known, the algorithm must rely on the cell voltages and currents. The fact that the shunts are have a fixed resistance means that there is a ceiling to the amount of imbalance between cells that can be overcome. It follows that balancing the cells as soon as possible is prudent in case the balancing required is significant.

Considering all of these factors, the algorithm deployed is as follows:

```

if (VB1 > min(VB2, min(VB3, VB4)) + a){ // a = 10mV
    REGB_HIGH = shunt1bit; // Activates Shunt
} else if (VB1 <= (VB2 + VB3 + VB4) / 3){
    REGB_LOW = shunt1bit; // Deactivates Shunt
}

```

This code is repeated for each of the four cells, the values VB1, etc. are the voltage of each cell in mV. In principal, the system applies hysteresis to switching on or off the shunt. A shunt is switched on if the cell voltage is 10mV above the minimum cell voltage, and only turned off again if it is equal or less than the mean of other cell voltages. The value of a dictates the range or tolerance for cell voltage difference. 10mV was chosen to be well within the final tolerance for cell voltages is 50mV, as dictated by the manufacturer, yet twice the minimum resolution of the system.

4.1.1 Termination Balancing

The fixed value of the shunt resistors dictates the maximum amount of energy which can be diverted from a cell. It is possible that the cells will reach their maximum voltage before the cells are balanced, causing an *over voltage* fault. To remedy this, a separate function called `termination_balancer` is used to balance the battery when the charger is disconnected.

`termination_balancer` is activated only when the battery is charging and an *over voltage* fault causes the charger to be disconnected. It applies shunts to the cell with the highest voltage and any cell within 10mV of it. If this would results in all four cells being shunted, if any other fault occurs or if the charger is reconnected, the function finishes.

4.2 Testing Methodology

The performance of the balancing algorithm and hardware was verified and quantified. The test procedure was based on [30] and [31], the cells were set to have different SoC and then were charged to completion. Differing from [30] and [31], larger SoC differences were used.

The procedure for the test was to discharge the battery through a load, while one or more cells were targeted to unbalanced. The targeted cells were also discharged through their shunt resistors. When the non-targeted cell(s) reached 3.9V, the load was disconnected but the targeted cell(s) continued to be discharged through their shunt resistors until a specified imbalance was achieved. The relative imbalance is defined in equation 4.1. The battery was then recharged and the affect of the balancing system was observed.

The value *relative imbalance*, 4.1, was generated to ensure consistent tests. During the tests, the current through each cell is integrate to give the charge in each cell. The value is initialised at zero with all cells fully charged, so during the test the charge in each cell is negative. The value represents the difference between the charge in the targeted and non-targeted cells as a percentage of the non-target cells' charge. To avoid meaningless values as charge in the To avoid meaningless values of *relative imbalance* as the charge values approach zero, the maximum value of the charge in the non-targeted cells across the whole test is used for the calculation. Visually, the value can be seen in figure 4.4. In the plot *Accumulated charge* the maximum magnitude of the non-targeted cells' charge occurs at zero minutes. The value *relative imbalance* is the difference between the blue (cell B4) and yellow (cell B1) lines as a ratio of the initial value of the blue line.

The balancing test procedure was realised through a function named `unbalancer()`. The function takes the number of target cells (i.e. one, two or three) and the *relative imbalance* and discharged and charged the battery appropriately. The load must be disconnected and the charger connected manually, so there is variability in the rest period between setup and testing phases.

$$\text{Relative Imbalance} = \frac{|q_{\text{target cell}}(t)| - |q_{\text{non target cell}}(t)|}{\max(|q_{\text{non target cell}}|)} \times 100 \quad (4.1)$$

4.3 Results

Tests were performed varying the number of cells targeted for unbalancing and varying the relative imbalance. Nine combinations of target cells and relative imbalance were tested: three combinations of cells and three levels of relative imbalance. This

gave a cross sectional view of the performance of the system in mild to extreme cases of imbalance in one or more cells. In each test either one (B1), two (B1 and B2) or three (B1, B2 and B3) cells were targeted for unbalancing. This is similar to the tests performed by [30, 35], but the distribution of imbalance cells is varied across multiple tests, rather than lumped in one test. The target relative imbalance was either 15%, 20% or 30%. Figure 4.6

4.3.1 Test Procedure

A test targeting cell B1 for 15% relative imbalance is shown in figures 4.2, 4.3 and 4.4 for the purpose of analysing the details of a test.

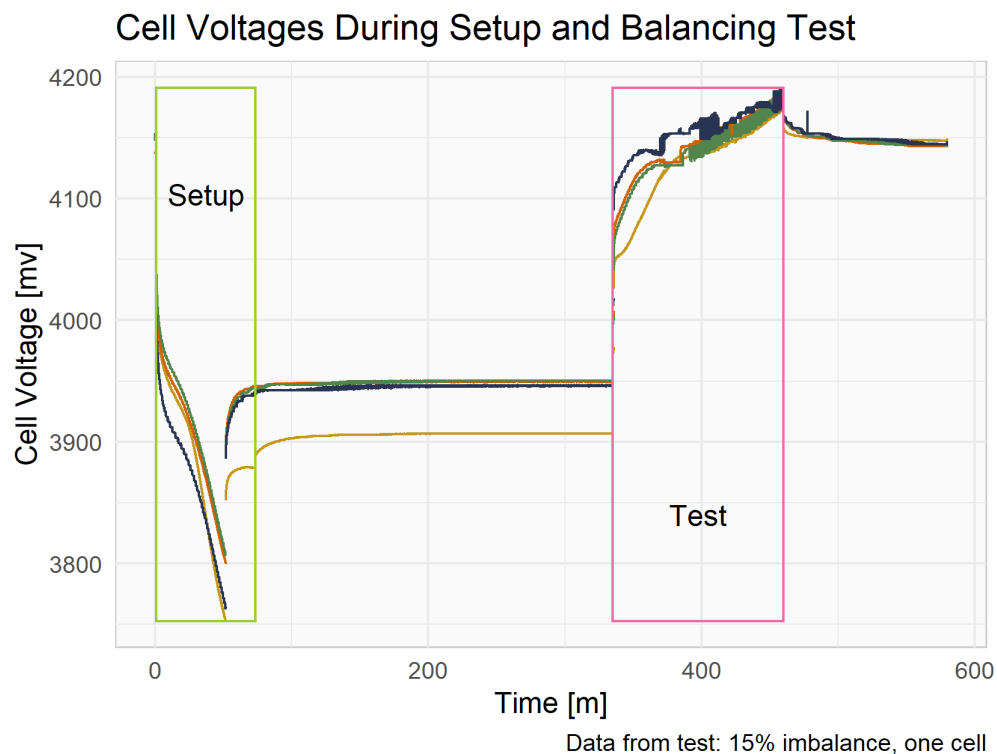


Figure 4.2: Cell voltages during the setup and test phases

Figure 4.2 shows the terminal voltage of each cell for the duration from setup to past test completion where cell B1 was discharged to give a relative imbalance of 15%. For clarity and comparability, the setup and test portions are plotted separately. During the setup period the battery is discharging and the unbalancer

function is active. After the target imbalance is reached there is a period of rest before the test. During the test the battery is charged.

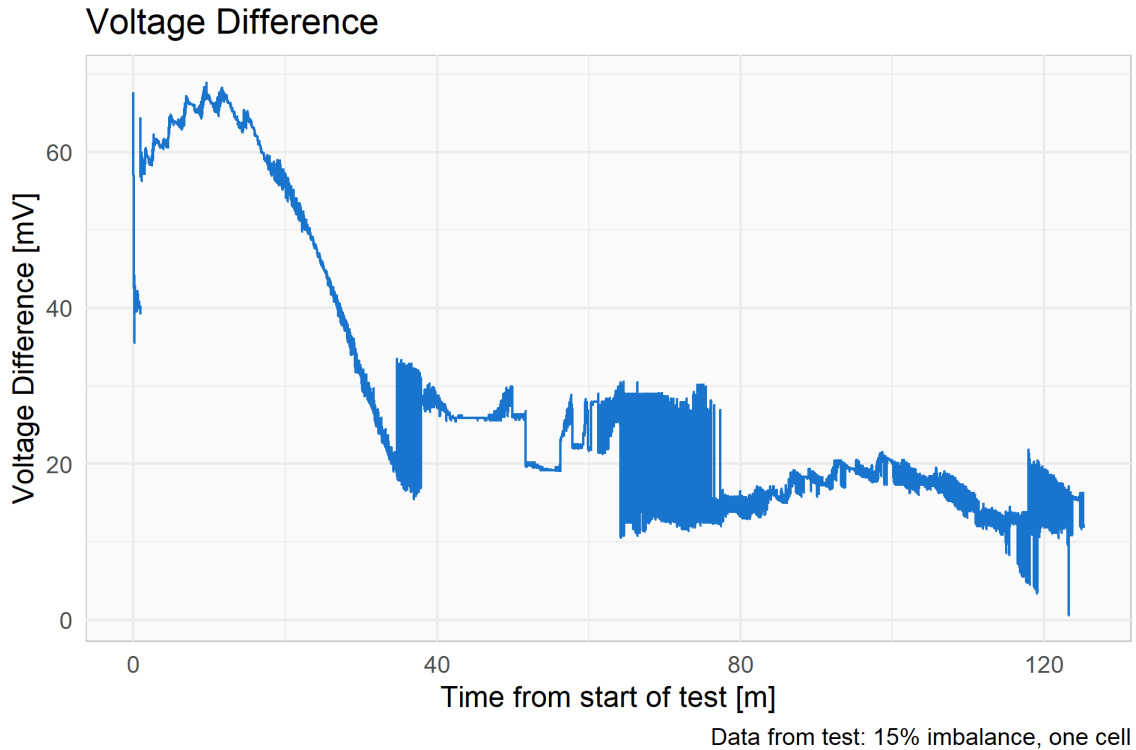


Figure 4.3: Cell voltage difference during test

Figure 4.3 shows the difference in voltage between the highest and lowest voltage cells during *test* period in figure 4.2. Most notable is the fact that a voltage imbalance of ~ 65 mV was induced and then successfully reduced to 12mV by the balancing system. The rapid changes in the voltage difference between 35 and 80 minutes is caused by shunt resistors being switched on and off as the cell voltages converge.

Figure 4.4 shows the net charge in each cell, the relative imbalance between the B1 and the other cells, and the state of each shunt during the test. The accumulated charge is the integral of the current through each cell, for reference, $1e+6 \text{ } mq \approx 278 \text{ } mAh$. The charge is initialised to zero at the start of setup, negative charge corresponds to a discharging of the cell. The exact state of the balancing shunts during the test are shown in *Balancing Shunt States During Test*. Note that the border of the regions have lower transparency, so darker regions represent times

when the shunts were repeatedly connected and disconnected.

The plot *Accumulated Charge* in figure 4.4 clearly shows the imbalance between the cells. The cells are balanced while charging, but their charge does not return exactly to zero. It is likely that the assumption that all cells were equally charged at the start of setup was incorrect. Nevertheless, the relative imbalance is successfully reduced to less than 5%.

In the period from \sim 35 to \sim 70 minutes the balancing shunts are not applied. This produced the flat section in *Relative Imbalance*, and was due to the low voltage difference as seen in figure 4.3.

In the event that the balancing system was able to correct the imbalance before a cell reached its maximum voltage, a separate subroutine named `termination_balancer` was called. The exact mechanism of the function is described in section 4.1.1.

Figure 4.5 shows three plots, the voltage of the cells during the charging phase of a test, a highlight of the final section, and the corresponding shunt states for that section. The first plot, *Cell Voltage*, shows the terminal voltage of all four cells, the lines at 4200 mV and 4150 mV represent the maximum safe voltage and the minimum charged threshold respectively. The second plot, *Cell Voltage Highlight*, show that when cell B4 reaches the maximum voltage before the battery is fully charged, a fault condition is activated and the charger is disconnected for the cool down period. This fault condition is triggered four times. The exact fault condition caused `termination_balancer` to be called, during the cool down period it applied the shunt resistors to cell B4 to discharge it before charging recommenced. Subsequently, when the third and fourth faults occurred, the other cells had high enough voltages to also require shunting. The third plot, *Shunt State*, shows in red the periods when a shunt was applied by the `termination_balancer` function. Note that the shunt for cell B4 is on almost continually, unlike those for cells B2 and B3. Both the balancing system and `termination_balancer` function are attempting to balance the cell.

The voltages in figure 4.5 contain an interesting *staircase* like form. This is a result of the voltage control system in the external charger, not due to any internal resolution limitation of the BMS.

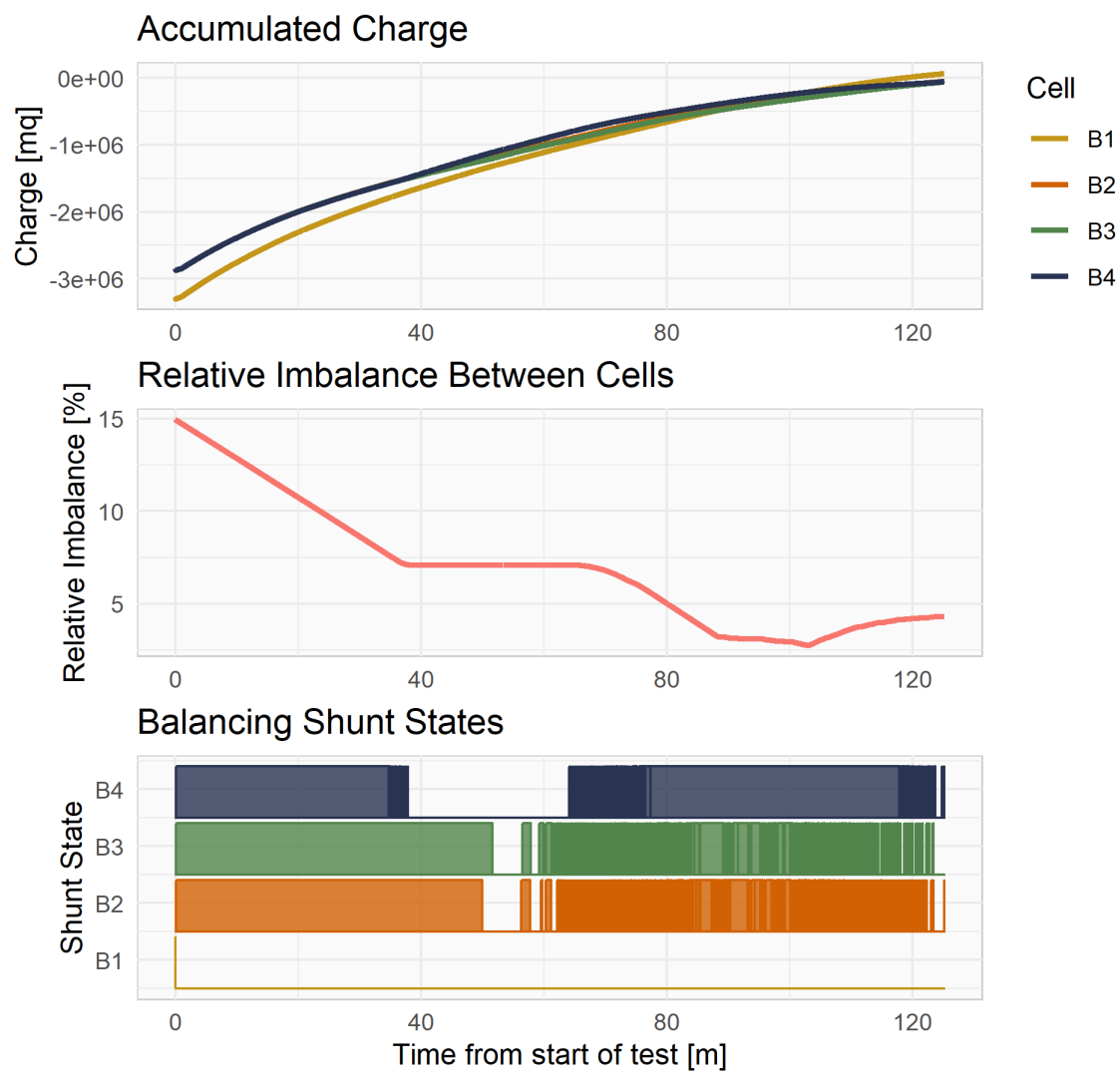


Figure 4.4: Accumulated charge, relative imbalance and shunt states during test

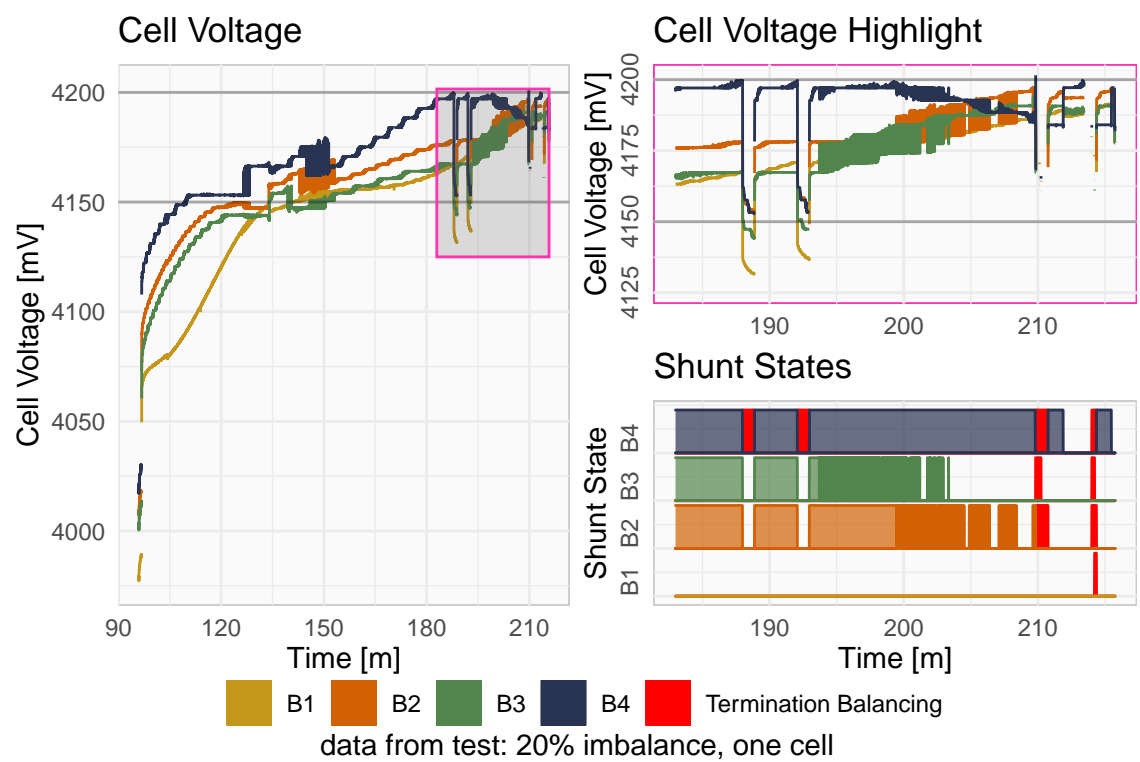


Figure 4.5: Action of the `termination_balancer` function, cell voltages and shunt states.

4.3.2 Cross Sectional Tests

The following figures show the results give a *cross sectional* view the performance for all nine cases of target cells and relative imbalances. Each figure contains a small multiple of plots showing all combinations of the two independent variables, *number of target cells* and *relative imbalance*. The initial conditions for each test case is shown in figure 4.6, all cells have been discharged, with some more so. Across each row, the plots increase in relative imbalance, down each column the plots increase in the number of cells targeted by unbalancer.

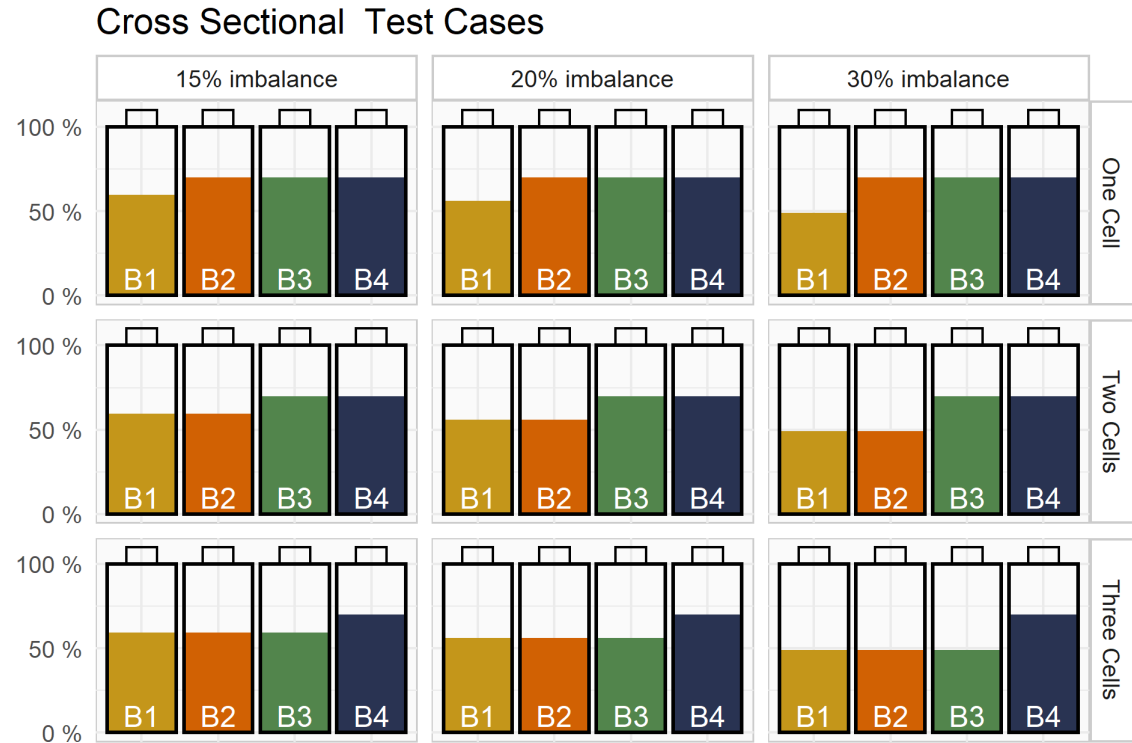


Figure 4.6: Initial cell SoC levels for each test case

The plots in figure 4.7 shows a similar response for all cases as were seen in the example case in figure 4.3. All nine tests have peak at the end of discharging which is corrected by the balancing system by the end of charging. The same artefacts from shunts being switched and the non-linear voltage response of LiBs occur in each plot. In the plots for 30% relative imbalance, there was an additional lower peak that occurred half way through charging.

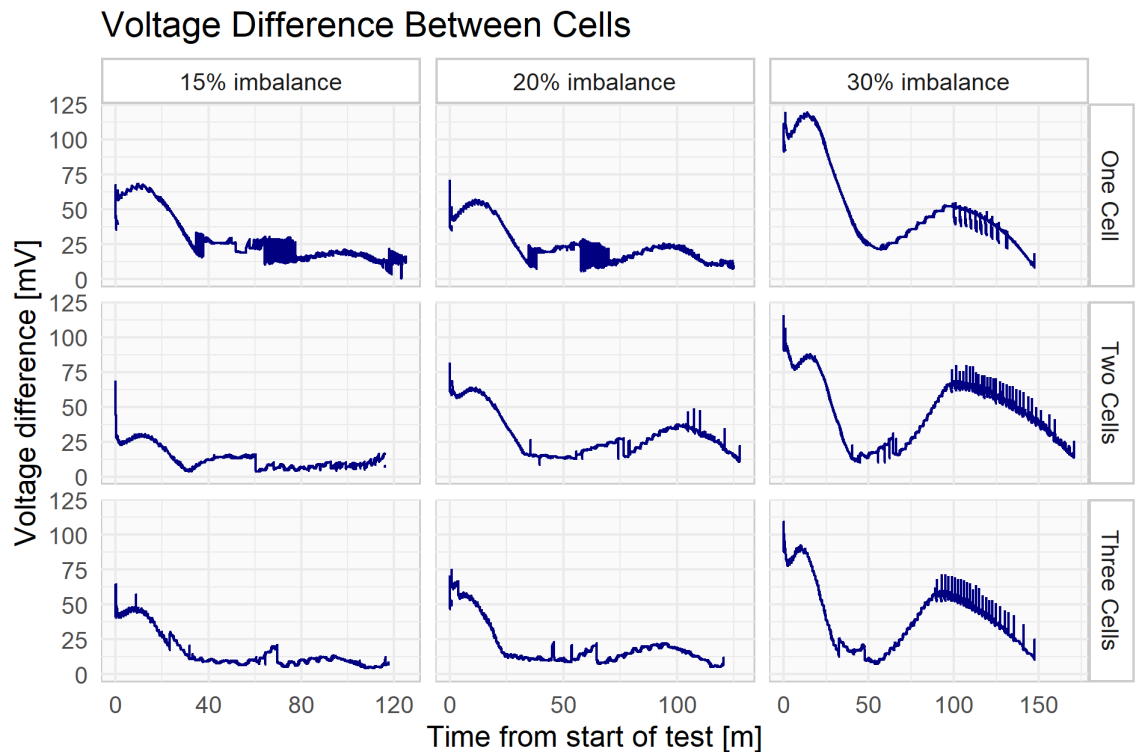


Figure 4.7: Cell voltage difference across all test conditions

The second peaks seen in figure 4.7 is due to the voltage of one cell rising faster than the others. It is not being charged faster, in fact it is being targeted by the balancing system. The estimated cell OCV are plotted in figure 4.8, to show the voltages of all four cells without the influence of charging rate and time. The OCV, as estimated by Lievre's and discussed in the next chapter, do not change the order of the voltages, but simply remove the large changes in overpotentials from shunts switching.

Table 4.1 lists the maximum and final values for the plots in figure 4.7. The maximum voltage difference is of course greater for higher relative imbalances, the final value is also higher. Importantly, the final voltage difference is significantly reduced for all cases.

Figure 4.9 shows the relative imbalance between the cells for each test. All tests show the target imbalance being met and then corrected by the end of charging. Tests with higher relative imbalance have smaller plateaus of imbalance during charging. As discussed, the plateaus are due to periods when the cells voltages are

Test Case		Maximum Voltage Difference [mV]	Final Voltage Difference [mV]
One Cell	15%	69.0	12.2
	20%	71.2	8.82
	30%	120	18.4
Two Cells	15%	68.7	7.79
	20%	81.5	21.6
	30%	116	25.7
Three Cells	15%	64.9	8.52
	20%	75.3	12.0
	30%	110	24.6

Table 4.1: Maximum and final voltage difference values

within the tolerance of the balancing algorithm (10mV). Naturally, this occurs more often with more mild imbalances.

Figure 4.10 shows the amount of charge diverted from each cell through the shunt resistors during the setup and test phases. Ideally, equal energy per cell would be used to re-balance the battery as were used to induce the imbalance, this will be discussed further in section 6.2.

To compare the amount of charge shunted during the test to the setup period, the normalised ratio of the two was used. Equation 4.2 shows the general formula and the calculation for the example seen in figure 4.10. The value $q_{R \text{ test}}$ and $q_{R \text{ setup}}$ are the sums of the charge through all shunts during the test and setup phases, $n_{\text{cells targeted}}$ is the number of cells targeted in the test, either one, two or three. The formula is constructed to normalise the amount of charge per shunt, without discounting any charge through either target or non-target cells. This quantity indicated the accuracy with which the balancing system applied balancing. The ratio for all nine test cases is shown in table 4.2. The first case *One Cell, 15%* appears to be an outlier in the set. Recall that it appears the battery was not fully

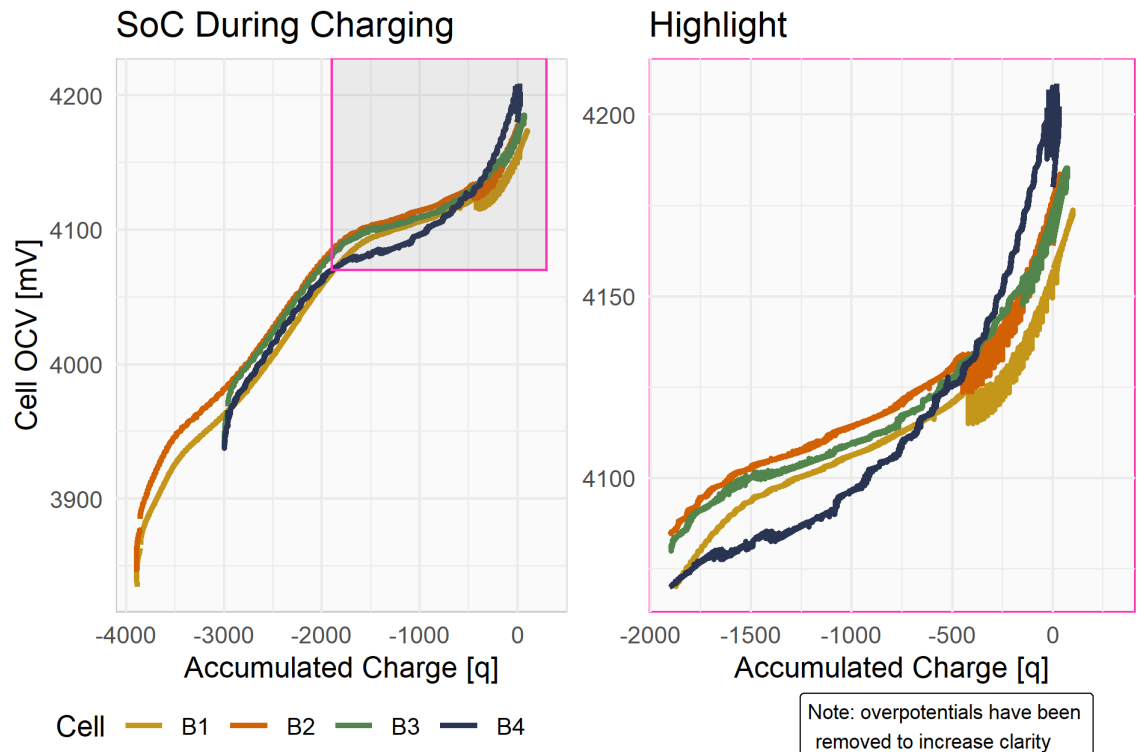


Figure 4.8: State of charge of each cell during test

charged at the beginning of the test. For this reason, the median of the set is more appropriate than the mean.

$$\text{Shunt Ratio} = \frac{q_{R \text{ test}} \div (4 - n_{\text{cells targeted}})}{q_{R \text{ setup}} \div n_{\text{cells targeted}}} \quad (4.2)$$

$$\text{Shunt Ratio} = \frac{(5.5\text{e}-5 + 6.3\text{e}-3 + 0.57 + 0.57) \div (4 - 2)}{(0.56 + 0.54 + 0 + 0) \div 2} = 1.04$$

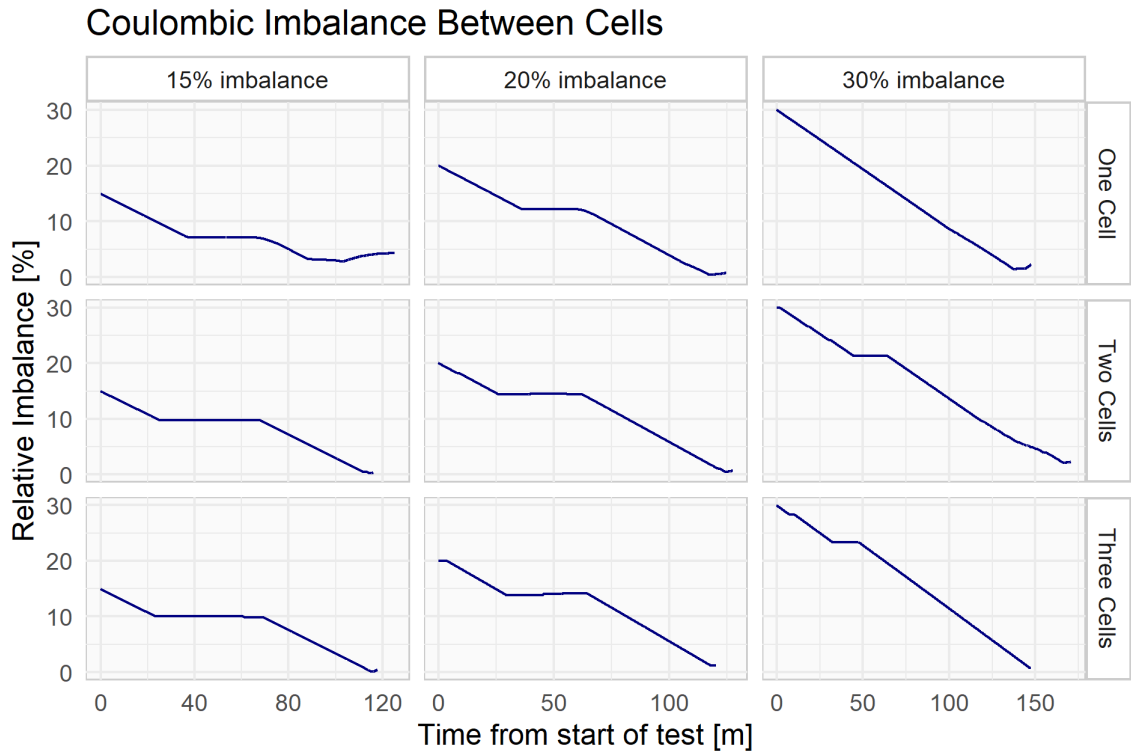


Figure 4.9: Relative imbalance between cells, as defined by equation 4.1

Shunt Ratio	15%	20%	30%
One Cell	1.28	1.02	1.05
Two Cells	1.01	1.04	1.08
Three Cells	1.03	1.08	1.03

Table 4.2: The shunt ratio, according to equation 4.2, across the nine test cases, median = 1.04

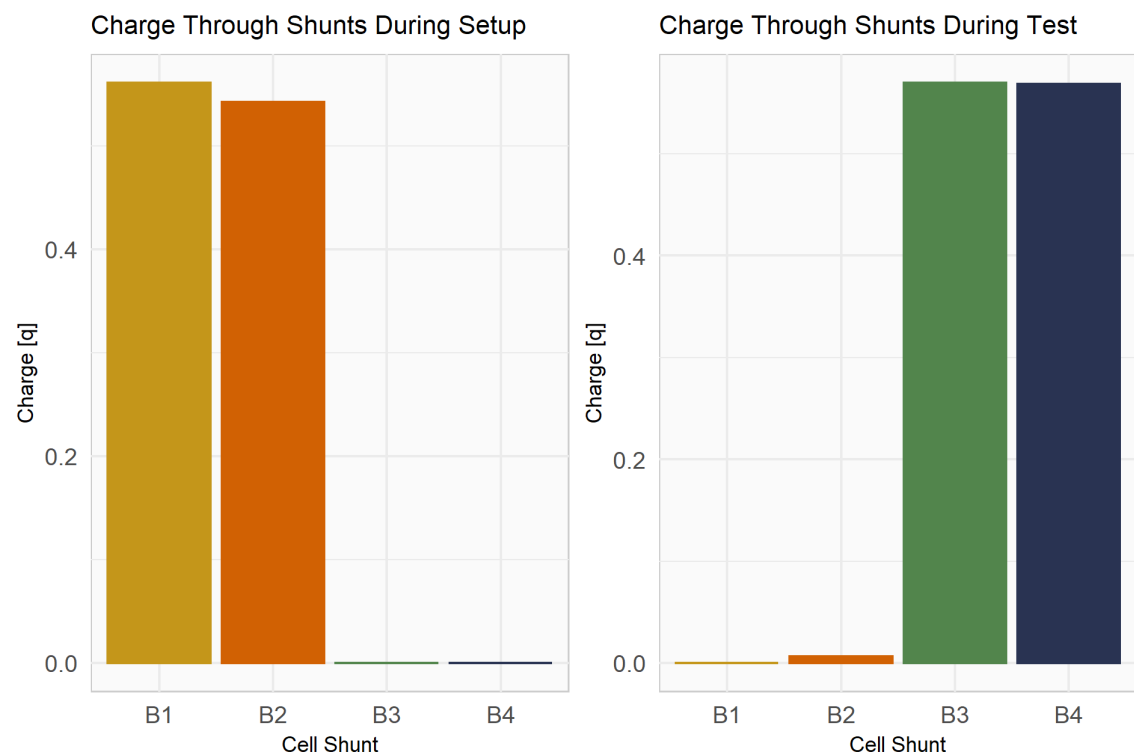


Figure 4.10: The charge that passed through each balancing shunt during the setup and test phases. Data from a test targeting two cells with 20% relative imbalance

4.3.3 Replication Tests

The following plots show the results of a single test replicated 10 times to show the repeatability of the results. All test results are shown superimposed, with varying hues of colour for each. Replication of the results was conducted for several test conditions, confirming the results.

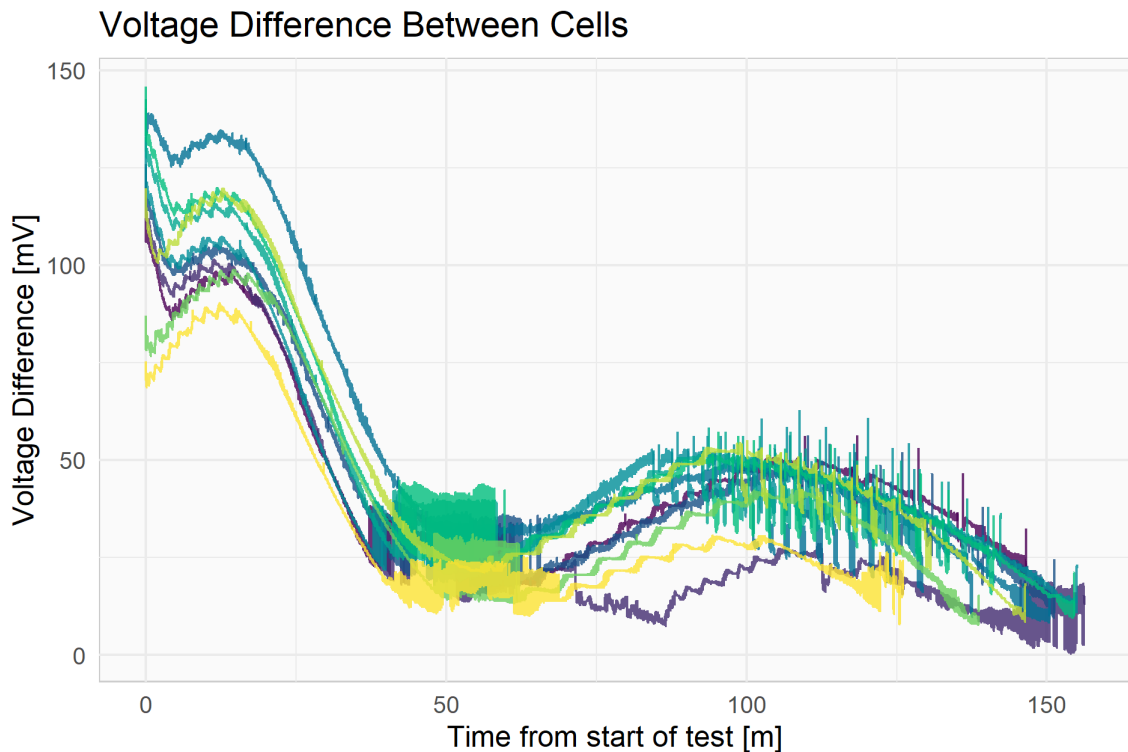


Figure 4.11: Cell voltage difference for 10 repetitions of cell B1 with a relative imbalance of 30%

Figure 4.11 shows the difference between cell voltages during the tests. The initial voltage difference of each test varies by almost 100mV, but the variation decreases to ~ 25 mV by the end of the test.

Figure 4.12 shows practically identical levels of relative imbalance during the discharge phase of the tests, and only minor deviation during the charging phase. Variation in the charging response occurs at 50 minutes, when the cell voltages in some tests are close enough to not trigger balancing.

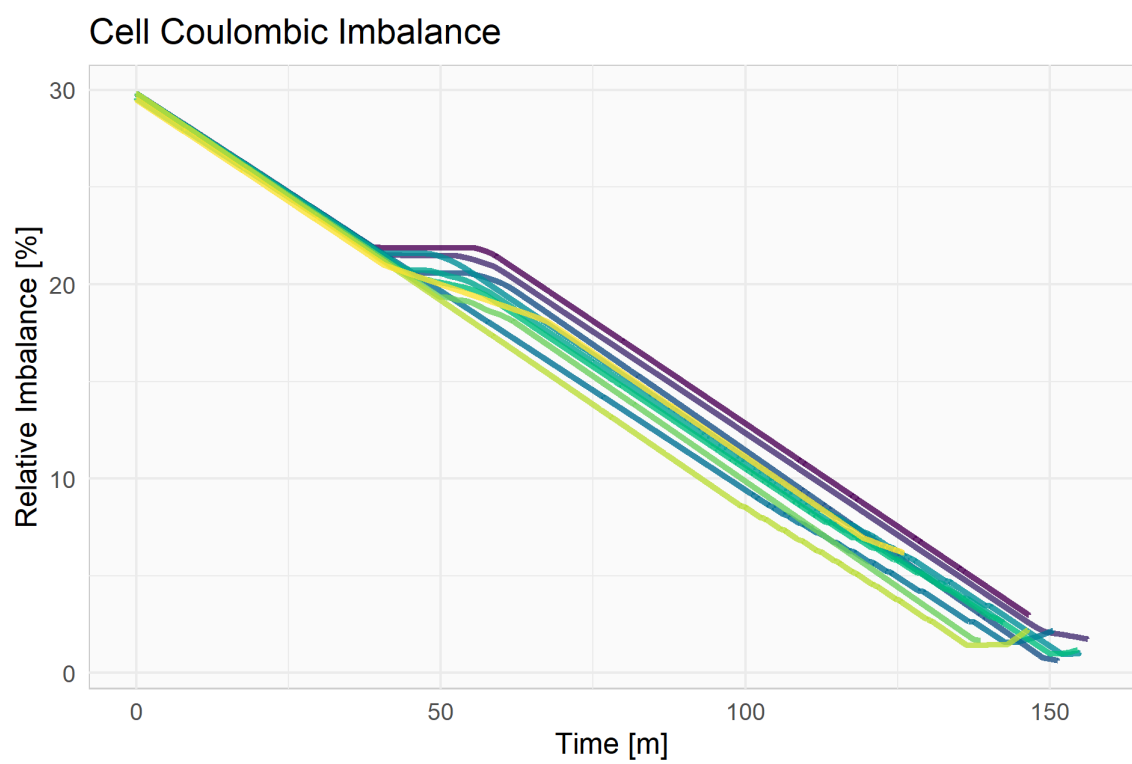


Figure 4.12: Relative imbalance for 10 repetitions of cell B1 with a relative imbalance of 30%

Chapter 5

Cell Modelling

Measurements of the cells may be the bedrock the BMS forms its decisions upon, but it is not the ultimate resource. The voltage, current and temperature of a cell indicate, but do not perfectly describe, the state of a cell. As is discussed in the literature, LiBs can be described by various equivalent circuit models (ECMs) [2, 7, 13, 14]. A common assumption in these models is that the *internal voltage*, or open circuit voltage (OCV) is a function of the SoC. As seen in figure 5.1, the difference between the terminal voltage, V_{cell} and the OCV is due to the overpotentials across the internal resistance. It would follow that the OCV is a better indicator of a LiB's state.

A method for estimating R_i was discussed in section 2.4.1, referred to as *Lievre's method* here. The method uses the popular principal that the cell impedance can be determined from the differential differential resistance of the cell [2, 7, 14, 21, 23, 32].

Other systems use external test equipment to generate changes in current and measure the differential voltage. What is unique about Lievre's method is that it passively observes the battery in normal operation, without the need of external equipment or dedicated calibration time. It achieves this by weighting the observation by their magnitude, discarding smaller values that are dominated by noise.

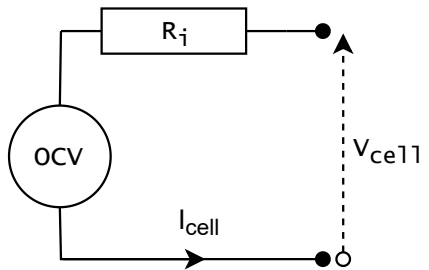


Figure 5.1: The simplified ECM employed by Lievre et al. [2]

5.1 Implementation

5.1.1 Original Implementation

The details of Lievre's method are discussed in section 2.4.1. Briefly, the system contains three components:

1. Differential Resistance: the change in current and voltage from the previous sample is calculated, as per equation 2.1.
2. Quality Filter: a value $\alpha_{quality}$ is calculated from the magnitude of the change in current, as per equation 2.2. *Small* ΔI map to $\alpha_{quality} = 0$, *large* ΔI map to $\alpha_{quality} = 1$, and *medium* ΔI map to a value between 0 and 1.
3. IIR filter: an infinite impulse filter takes the mean of previous value of R_i and the new R_i , weighed by $\alpha_{quality}$, as per equation 2.3.

Lievre et al. show that the sampling time will determine which components of the cell's internal impedance are represented in R_i .

Two important parameters, I_{min} and I_{max} , determine the limits between *small*, *medium* and *large* value of ΔI . The choice of these variable has a large impact on the performance of the system, as will be shown.

5.1.2 Extensions to the Original System

The application Lievre et al. designed their system for was a hybrid electric vehicle. This use case sees large charging and discharging currents in rapid succession. The large change in current events are what the method uses to estimate R_i . The described current events cannot be guaranteed in this project. To remedy this, a subsystem was developed to generate current events onboard the system in case the previous event became stale. This is referred to as the *calibration procedure*.

For an observation to become stale, means that the state of the battery may have changed since they were taken. Rather than counting the time since the last update to R_i , the subsystem counts the change in capacity of the battery. This avoids a scenario where it will repeatedly test the battery when not being used, since there is no reason to expect a change in its state. For the results in this project the change

in charge before a value was considered stale was set to approximately 5% of the total battery capacity.

New current events are generated by switching the shunt resistors, or the charger if available, to momentarily change the cells' current. If the charger is connected, the charger will be disconnected and reconnected. If, on the other hand, the charger is not connected the state of the balancing shunts will be inverted and then reverted. New measurements of the cell voltages and currents are taken between the momentary switching of the balancing shunts or the charger. Given the smaller magnitude of the shunt currents, $\sim 100\text{mA}$, they are switched on and off repeatedly. To minimise the affect this procedure has on the battery, the switching period is kept to a minimum, approximately 17ms.

5.2 Uncertainty in the Cell Model

Lievre et al. prescribe optimal selection of I_{min} and I_{max} to be above the minimum sensitivity of the current sensor and near the most important current variation occurring in normal operation [2]. However, they do not present justification for this.

It is clear that these values are the maximum bounds for I_{min} and I_{max} . Choosing I_{min} lower than the sensor's sensitivity would fail to exclude noise. Choosing I_{max} greater than the most important variation in current expected in normal operation, would simply reduce the value of important observations.

A better understanding of the effect of I_{min} and I_{max} can be found by analysing the propagation of uncertainty in the system.

The final output of the system, V_{OCV} , is calculated in multiple steps using many values. Figure 5.2 shows an overview of the functions involved in the process and how the uncertainties will propagate from the original measurements to the final value. A key for the figure can be seen in 3.9.

The uncertainties for each component of Lievre's method are shown in equations 5.2, 5.5 and 5.6, together these form the functional block of *Lievre* seen in figure 5.2. These were derived following the principals of the propagation of uncertainty in section 3.4.

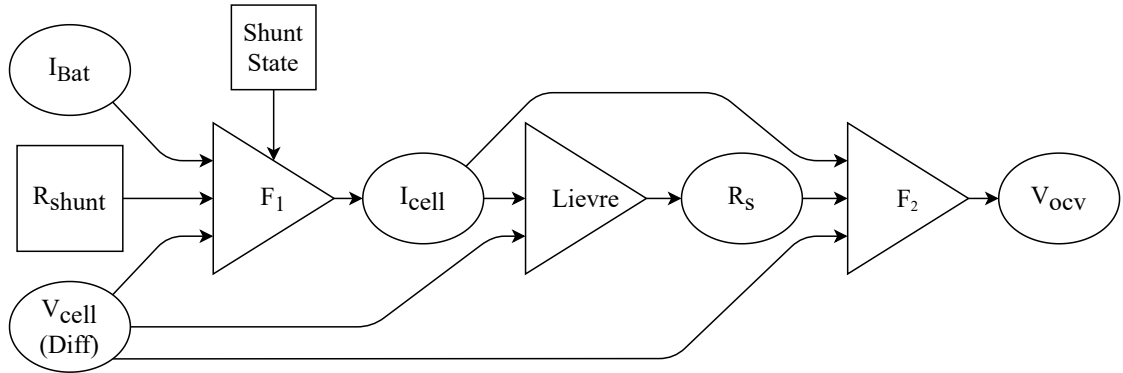


Figure 5.2: Functions for derived quantities

$$\alpha = \begin{cases} 0, & \Delta I < I_{min} \\ \frac{\Delta I - I_{min}}{2(I_{max} - I_{min})}, & I_{min} \leq \Delta I \leq I_{max} \\ 0.5, & I_{max} < \Delta I \end{cases} \quad (5.1)$$

$$\delta\alpha = \begin{cases} 0, & \Delta I < I_{min} \\ \frac{\delta\Delta I}{2(I_{max} - I_{min})}, & I_{min} \leq \Delta I \leq I_{max} \\ 0, & I_{max} < \Delta I \end{cases} \quad (5.2)$$

$$R_{\Delta V/\Delta I} = \frac{\Delta V}{\Delta I} = \frac{V_k - V_{k-1}}{I_k - I_{k-1}} \quad (5.3)$$

$$\delta R_{\Delta V/\Delta I} = \sqrt{\frac{\delta V_k^2 + \delta V_{k-1}^2}{(V_k - V_{k-1})^2} + \frac{\delta I_k^2 + \delta I_{k-1}^2}{(I_k - I_{k-1})^2}} \quad (5.4)$$

$I_k \neq I_{k-1}, V_k \neq V_{k-1},$

$$R_{S_k} = R_{S_{k-1}}(1 - \alpha) + R_{S_k}\alpha \quad (5.5)$$

$$\delta R_{S_k} = \begin{cases} \delta R_{S_{k-1}}, & \alpha = 0 \\ \sqrt{(\delta R_{S_{k-1}} \cdot (1 - \alpha))^2 + (\delta \alpha \cdot R_{S_{k-1}})^2 + (\delta R_B \cdot \alpha)^2 + (\delta \alpha \cdot R_B)^2}, & 0 < \alpha < 0.5 \\ \sqrt{\left(\frac{1}{2}\delta R_{S_{k-1}}\right)^2 + \left(\frac{1}{2}\delta R_B\right)^2}, & \alpha = 0.5 \end{cases} \quad (5.6)$$

Finally, the uncertainty in V_{OCV} is shown in equation 5.8 and is represented in the figure 5.2 by the functional block F^2 .

$$V_{OCV} = V_{cell} + I_{cell} \times R_{S_k} \quad (5.7)$$

$$\delta V_{OCV} = \sqrt{\delta V_{cell}^2 + \delta I_{cell}^2 \cdot R_i^2 + \delta R_i^2 \cdot I_{cell}^2} \quad (5.8)$$

5.3 Results

5.3.1 System Function

The stages of the R_i calculation for a brief period are shown in the following plots to illustrate how the system functions.

Figure 5.3 shows the current and voltage of cell B1 during a section of the setup phase of a balancing test. The period was chosen as it contains two large current events. The first change, occurring when the load is disconnected at A and the second when the cell's shunt is disconnected at B . In both cases, there is a clear and instantaneous change in voltage due to the cell's resistance and the change in current. From A to approximately 60 minutes, the cell voltage has a curved response, which can be attributed to the non-ohmic components of the cell's impedance.

The differential current and voltage, for the same period as in figure 5.3, is shown in figure 5.4. The peaks A and B have the values -917mA, 103mV and -98mA, 11mV respectively. The values represent the difference between consecutive samples and

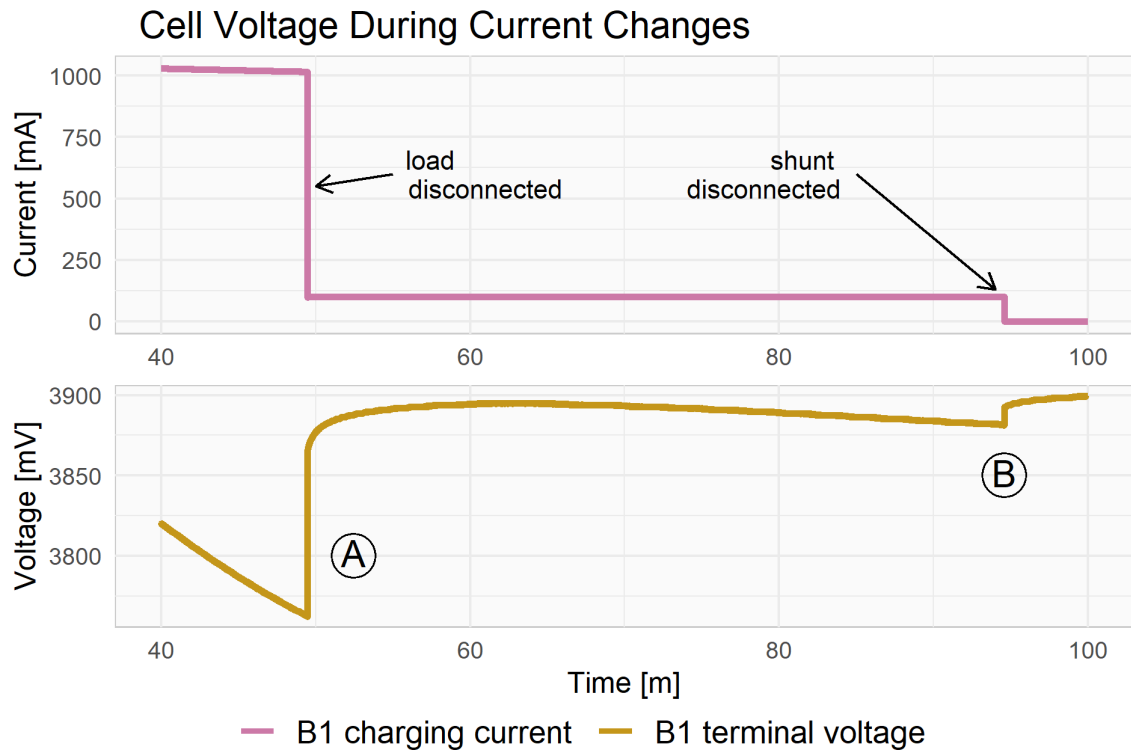


Figure 5.3: Cell current and voltage during changes in load

are calculated by the MCU in real time. They are the values ΔI and ΔV used in equation 2.1.

Figure 5.5 has the values ΔI and ΔV , from the previous figure 5.4, plotted on the V - I plane. The two prominent points A and B each have a line drawn through them, each coinciding with the origin. The slope of those lines demonstrates the differential resistance, $\Delta R = \Delta V / \Delta I$. The cluster of points at the origin marks the large number of zero values from figure 5.4.

Note that the x-axis in figure 5.5, $\Delta I[mA]$, is reversed. This is because cell current is defined with active sign convention, so its differential resistance would be negative. In order to report on the positive cell impedance being investigated, the impedance values are displayed as positive and the axis has been reversed to reflect this.

Plotting ΔI and ΔV for a longer period demonstrates the relationship that Lievre's method is attempting to distil, as seen in figure 5.6 with the overall balancing setup and testing period plotted. A similar figure was presented by [14] and is shown

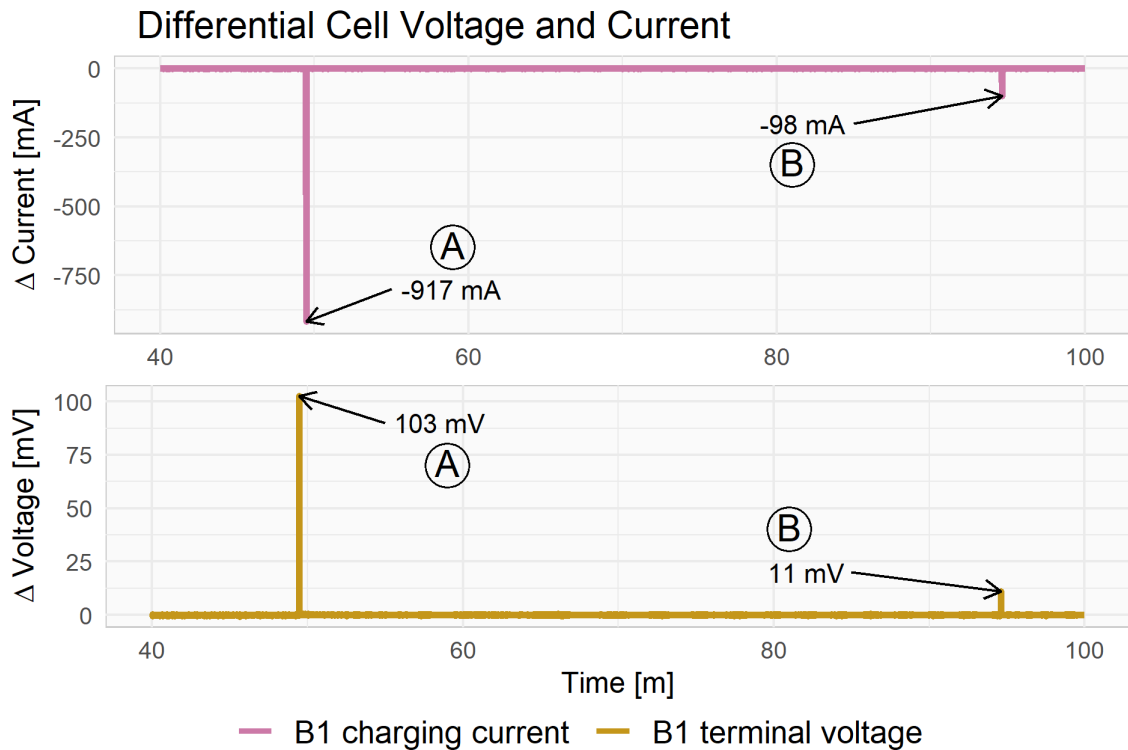
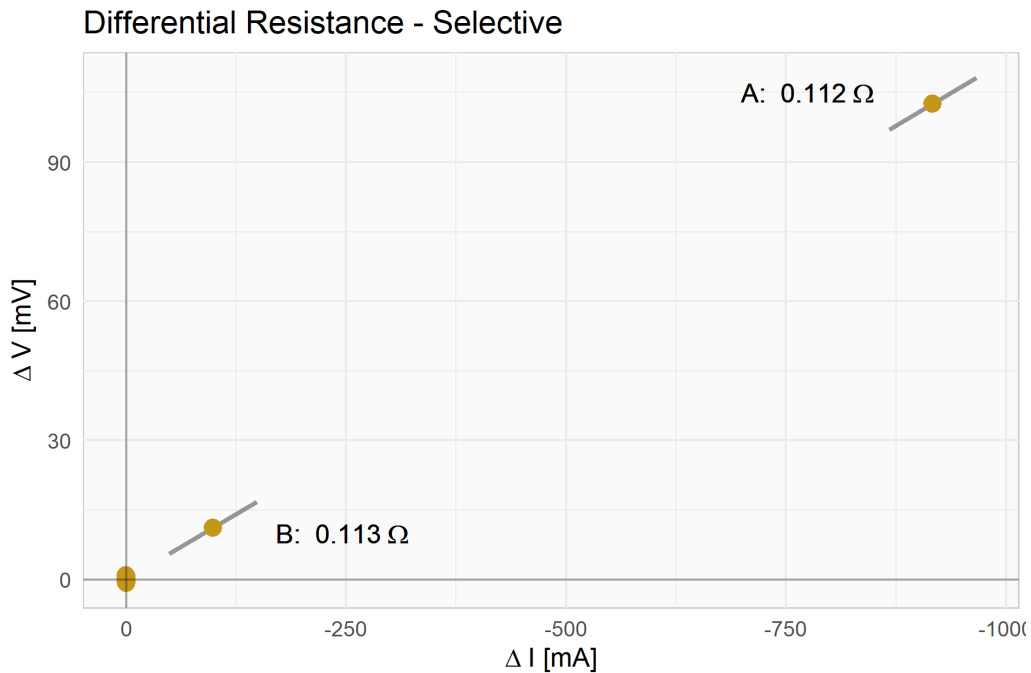


Figure 5.4: Instantaneous changes in current and voltage, ΔI and ΔV

in figure 2.15. The plot contains two large clusters around +100mA and -100mA. These are from times when shunt resistor were switched on or off for both balancing and the calibration procedure.

The value of $\alpha_{quality}$ is calculated from the magnitude of ΔI , the x axis in figure 5.6. To illustrate this, the lower part of the plot has been highlighted to show a hypothetical weighting with $I_{min} = 50mV$ and $I_{max} = 150mV$. The discarded observations are above the red section, weighted observations above the yellow section, and unweighted observations above the green section.

The calibration procedure can be seen in figure 5.7. In the plots the battery is being charged, so although the current is changing, it is too subtle to be useful for estimating R_i . The calibration procedure is triggered three times, each time the charger is momentarily disconnected and reconnected. The changes in current and voltage are used to update the cell's estimated R_i in the second plot. The OCV estimate is shown alongside the cell voltage. Note that the cell voltage drops to the OCV during the calibration procedure.

Figure 5.5: Changes in current and voltage on the V - I plane

Cell	R [Ω]	R^2
B1	0.0994	0.9910
B2	0.1043	0.9713
B3	0.0978	0.9605
B4	0.1217	0.9198

Table 5.1: V - I lines of best fit slope and R^2 for figure 5.6

In figure 5.6 a line of best fit, coinciding with the origin, is drawn for each cell. The line gives an approximation for the resistance of the cell, although it does not contain any weighting of points like in Lievre's method. Table 5.1 shows the slope and R^2 of the lines. As can be seen from the R^2 values the lines are a near perfect fit. The slopes of the lines are similar to the values produced by Lievre's method for the same period.

An important point made by Lievre et al. [2], was that the sampling time, Δt , of the system dictates the components of the cell's impedance which will be measured. A test to investigate this effect was conducted, a large current event was

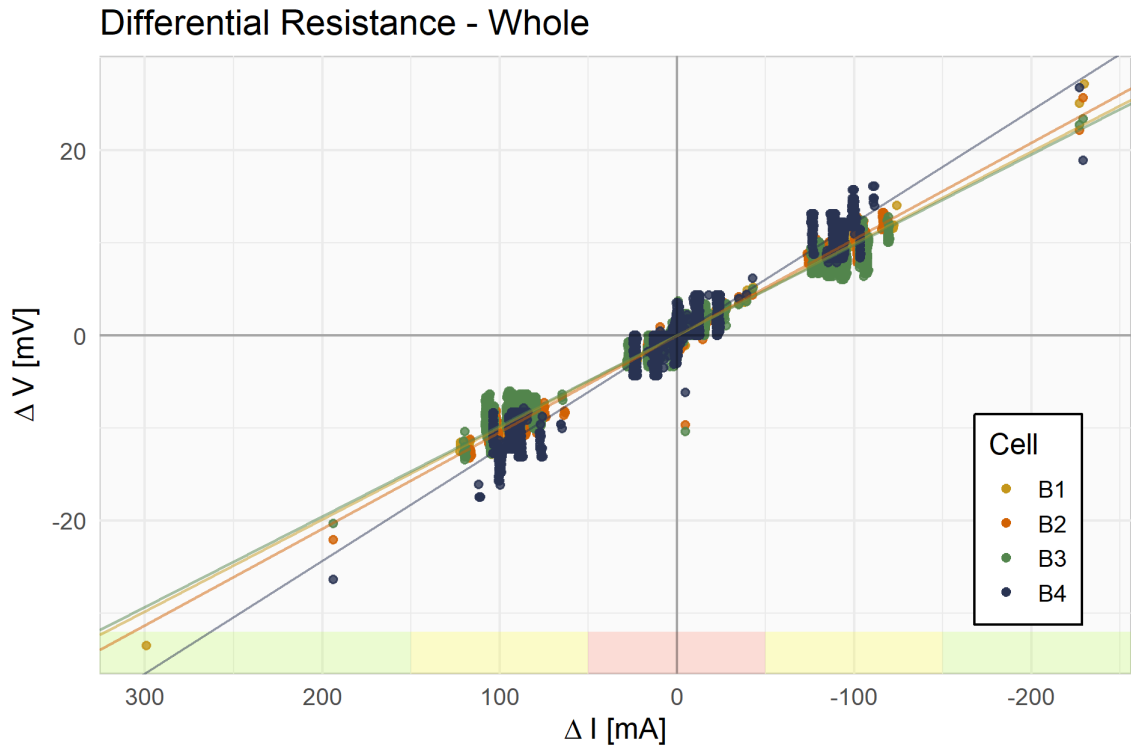


Figure 5.6: Changes in current and voltage on the V - I plane for all cells during a longer period. Coloured highlights indicate the weighting from a possible I_{min} , I_{max} selection

induced and the differential resistance for varying Δt were calculated. The voltage response during this test is shown in figure 5.8. A 16Ω load was disconnected from the battery at approximately 7.5s and reconnected at 12.5s to produce the response. The differential resistance was calculated, as per equation 2.1, with V_{k-1} immediately before the load was disconnected, and V_k varying between the 7.5s to 12s.

The varying differential resistance results are shown in figure 5.9. The V_{k-1} and I_{k-1} are the left most points on their respective plots. The vertical lines **A**, **B** and **C** mark common sampling times used by the system. Note that the plot is shown on a semi-log scale.

All three plots in figure 5.9 have an exponential response to the removal of the load. However, this response is to be expected from the capacitive components of the cell model. To examine this response more closely, figure 5.10 shows the differential resistance plot from the previous figure 5.9 in non-logarithmic time, with

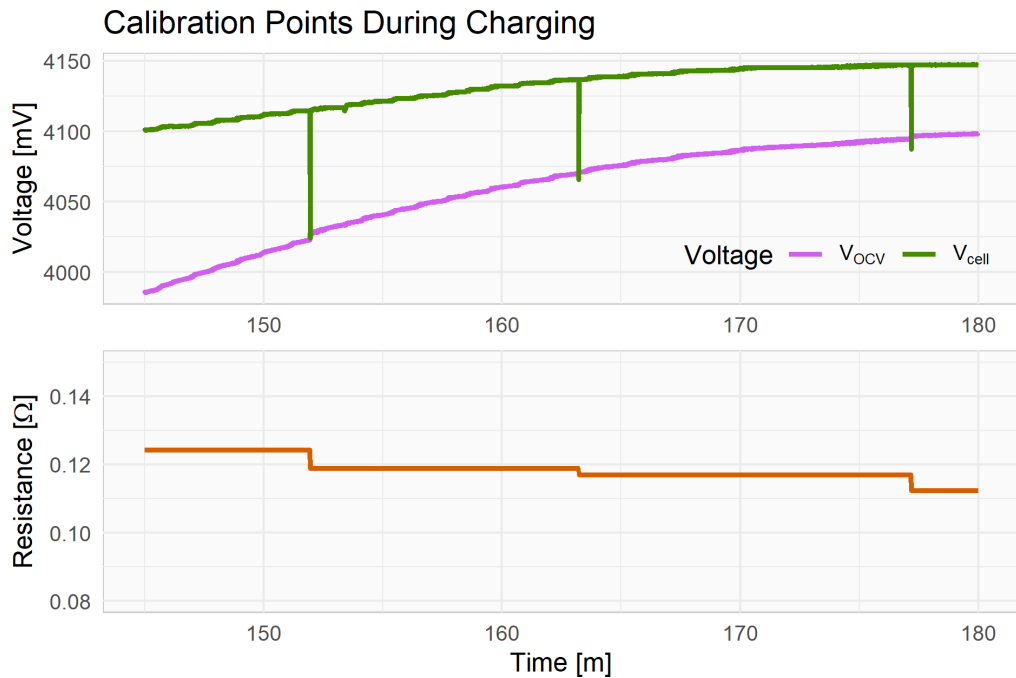


Figure 5.7: Cell B2 voltage and R_i during charging. Showing three instances of the calibration procedure.

an exponential curve fitted to the data. The parameters of the model can be seen in table 5.1.

Cell	τ [s]	b [Ω]	c [Ω]
B1	0.618	-6.019E-03	0.125
B2	0.207	-7.962E-03	0.133
B3	0.912	-5.605E-03	0.112
B4	0.747	-6.392E-03	0.114

Table 5.2: Exponential fit parameters for figure 5.10

$$\text{Model: } \Delta R = b \times \exp(\Delta t / \tau) + c$$

The value R_i is only an estimate, the level of its uncertainty needs to be considered before it is used. Figures 5.11 and 5.12 show the impact of I_{min} and I_{max} on the uncertainty and the responsiveness of the system.

The relative uncertainty cannot easily be plotted or parameterised for R_i and V_{OCV} like they were for simple cell voltages and currents. This is because the uncer-

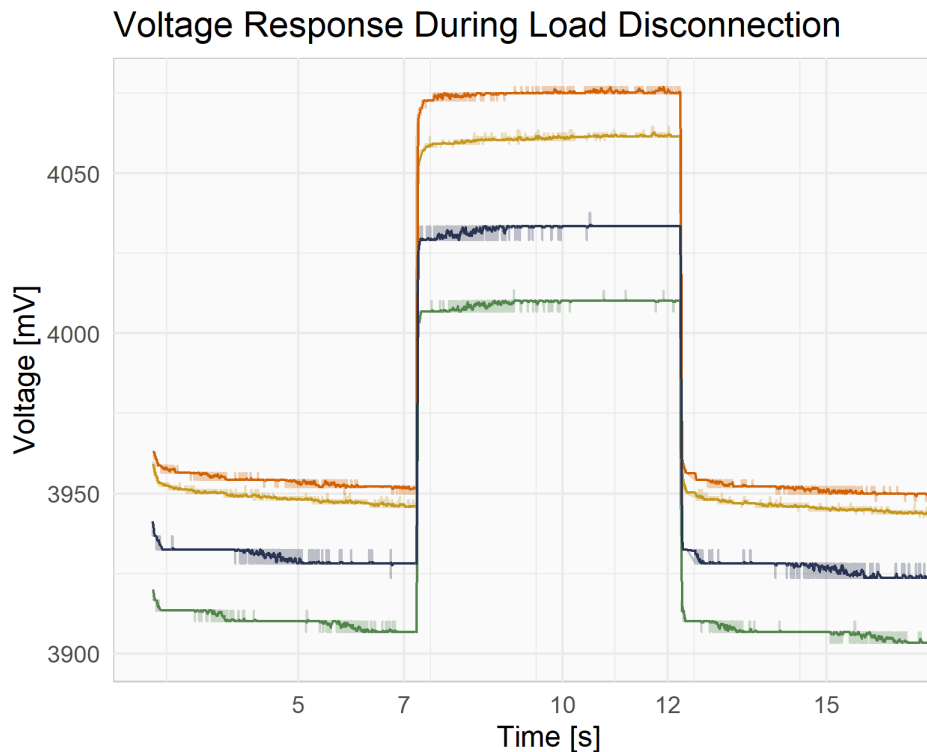


Figure 5.8: Voltage response for a 16Ω load being disconnected at 7.5s and reconnected at 12.5s

tainty fluctuates with the uncertainty in incoming current and voltage observations. To understand the uncertainty in V_{OCV} , the figure 5.13 shows the cell voltage and V_{OCV} with their uncertainties. The data comes from a test of the balancing system, where the battery is discharged and then recharged. The same period and voltages are shown in figure 5.14, but plotted against cell capacity (initialised at fully charged = 0) instead of time.

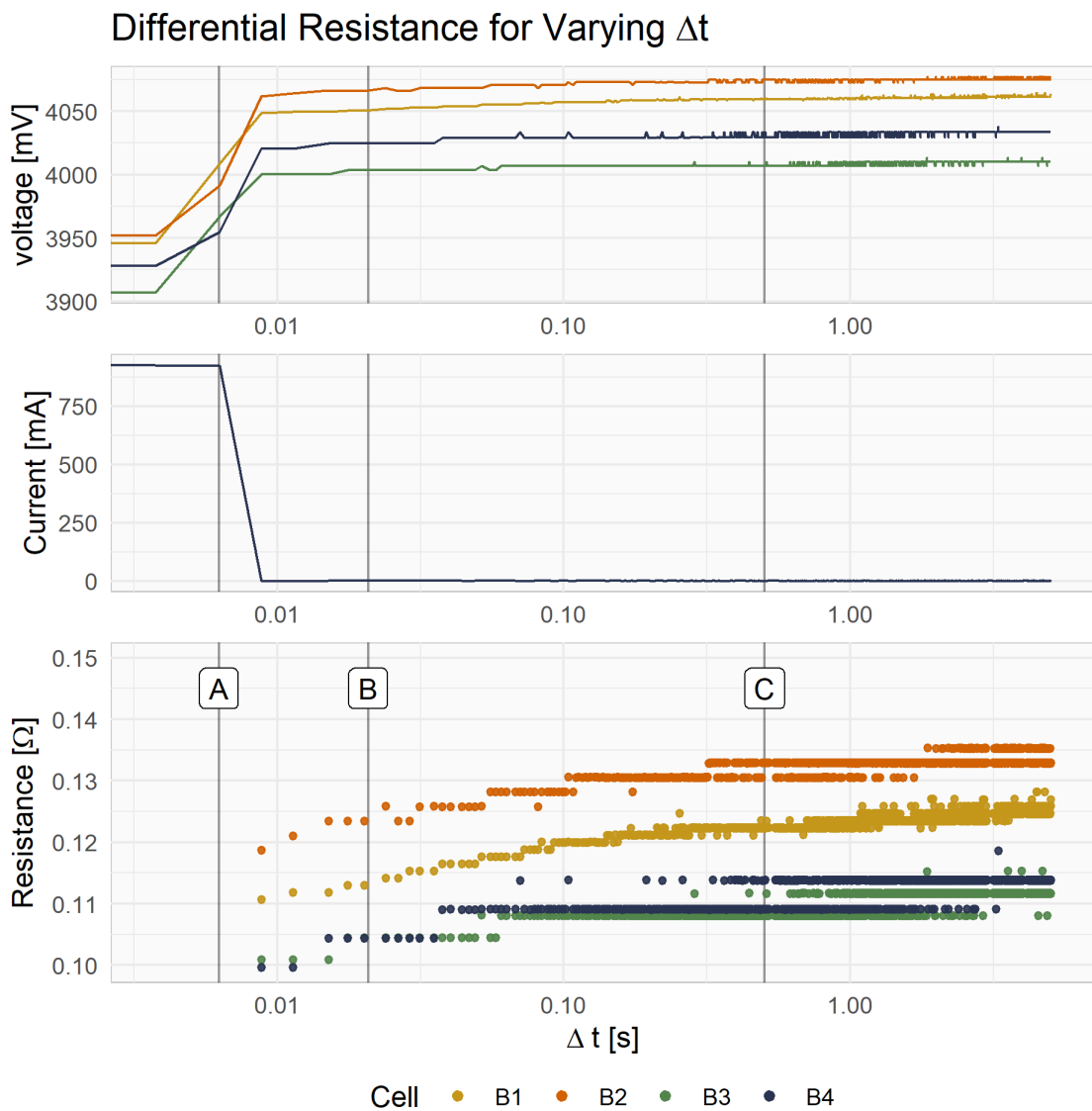


Figure 5.9: Differential resistance for varying sample time Δt , for the period 7s to 12s in figure 5.8.

- A:** 2.5ms, minimum sampling time,
- B:** 17ms, calibration procedure sampling time,
- C:** 500ms, nominal sampling time

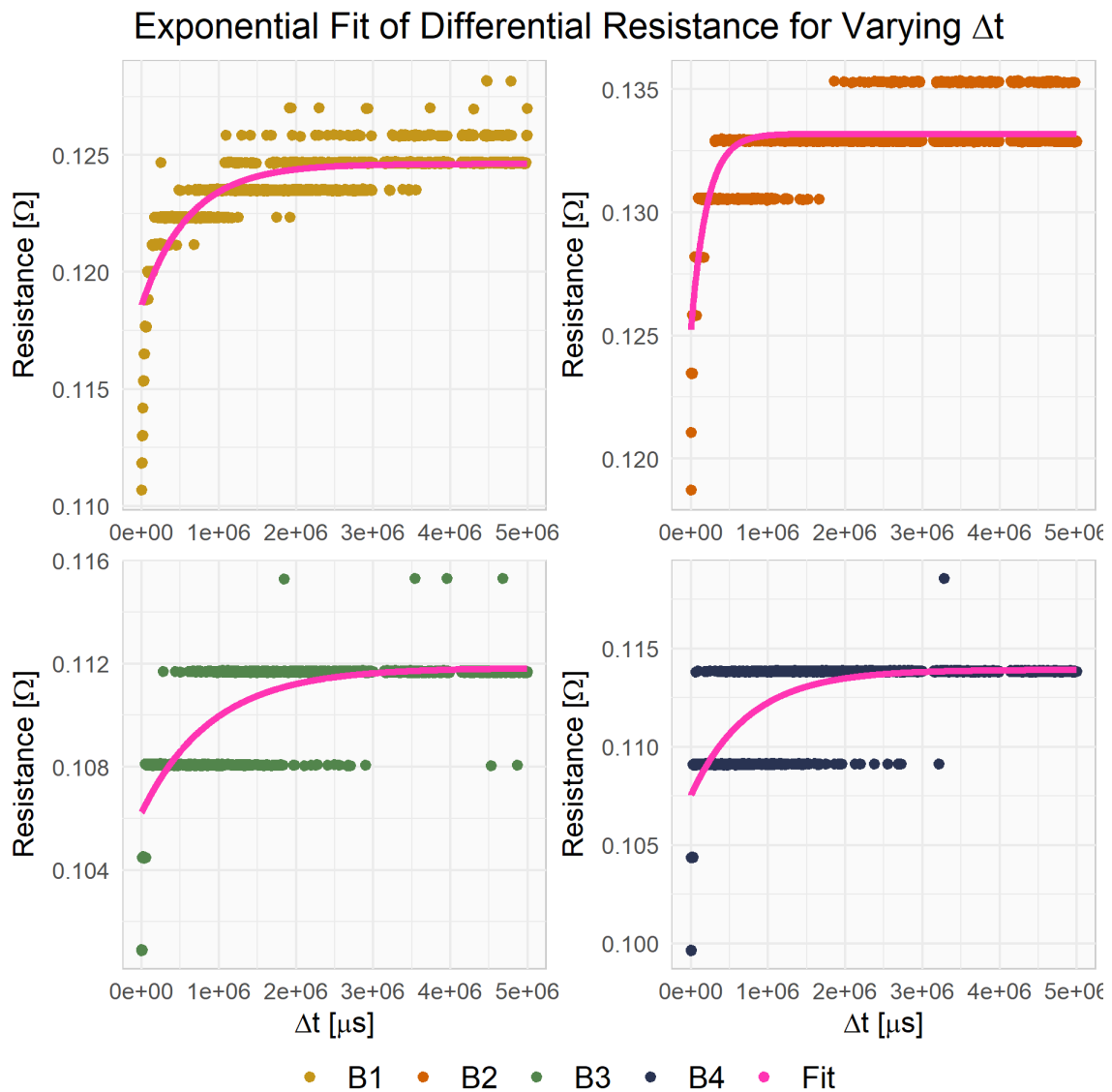


Figure 5.10: The exponential fit of the differential resistance responses seen in figure 5.9

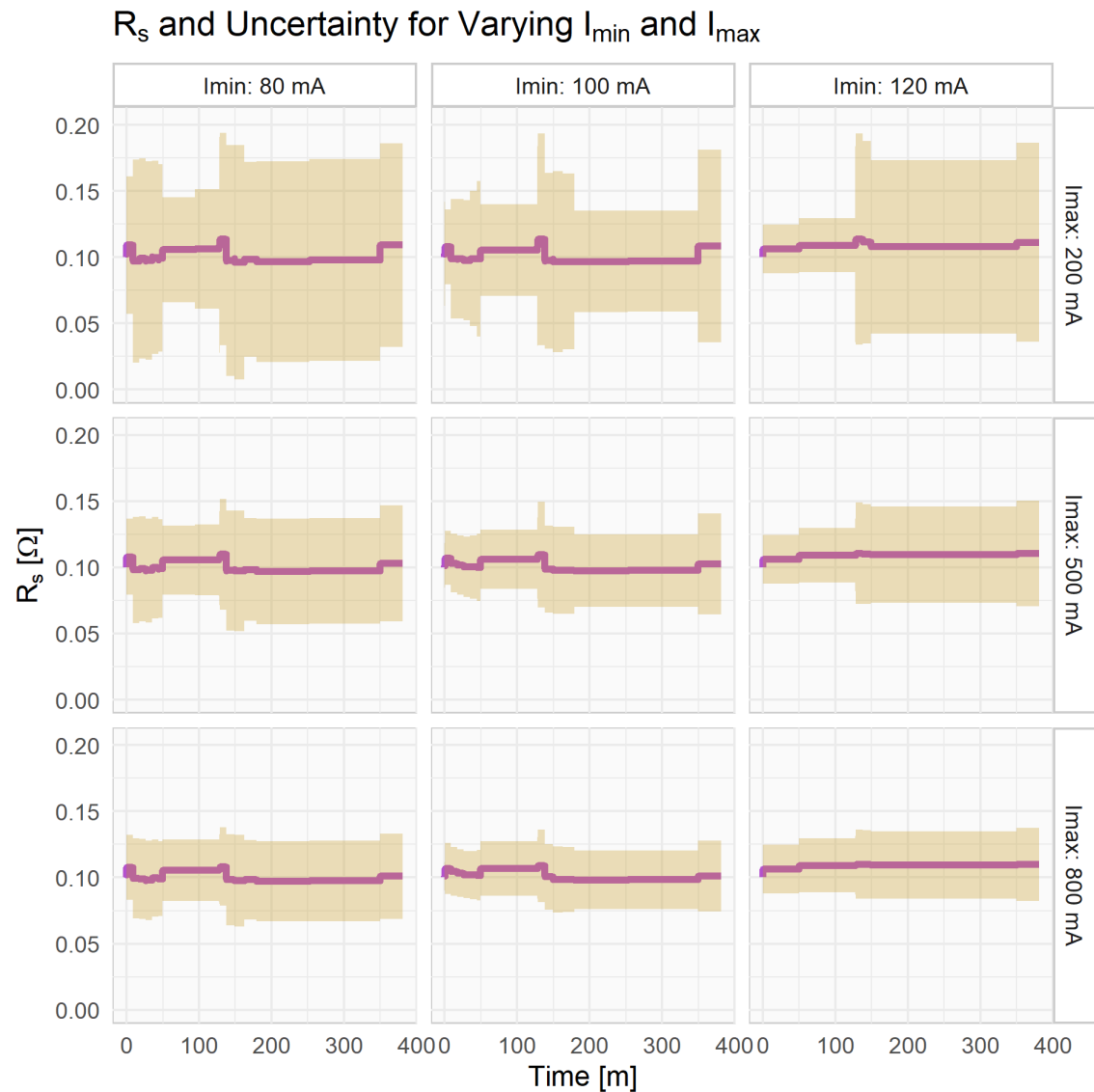


Figure 5.11: R_s and its uncertainty for cell B1 with varying I_{min} and I_{max} values for the same period. Columns have constant I_{min} values, rows have constant I_{max} values

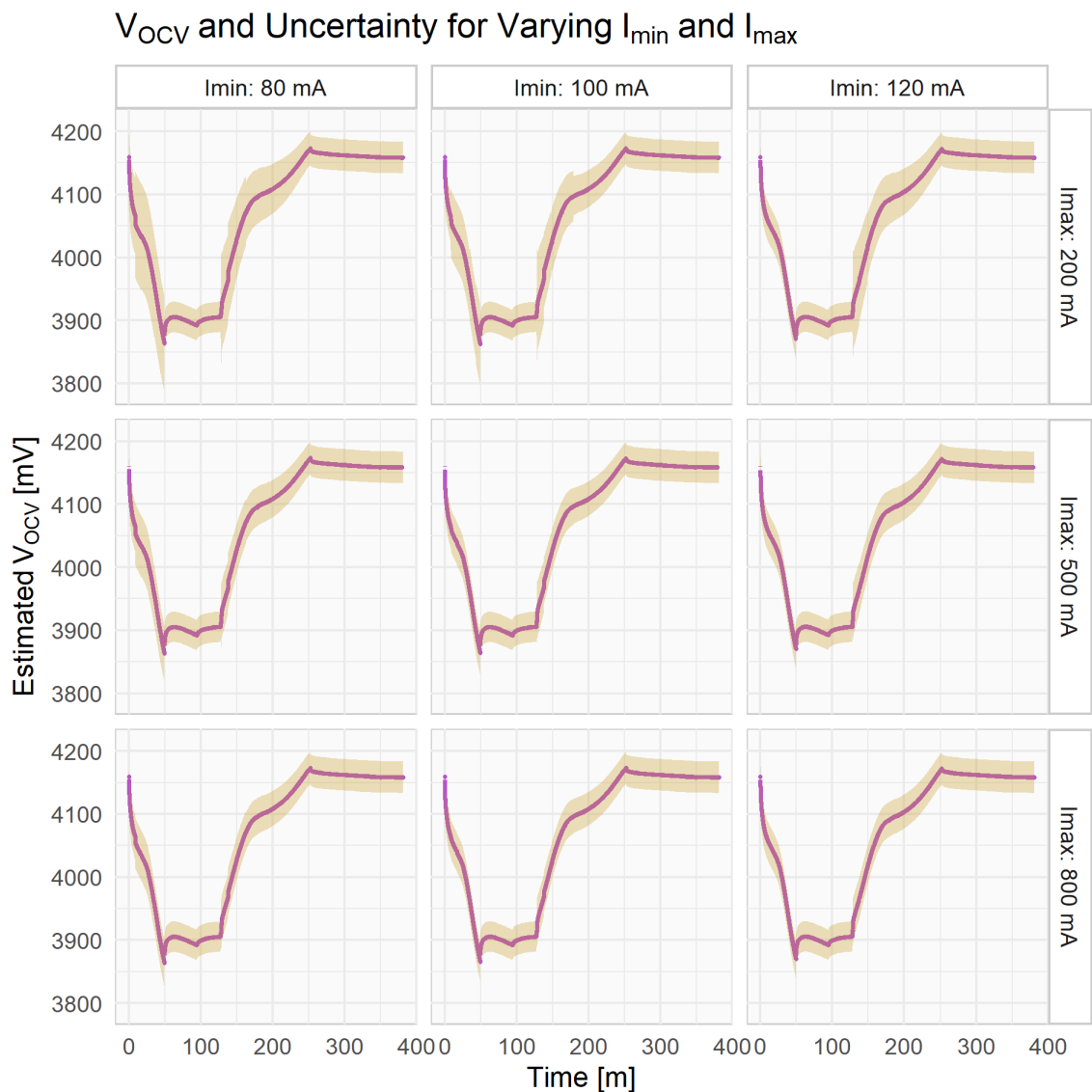


Figure 5.12: V_{OCV} and its uncertainty for cell B1 with varying I_{min} and I_{max} values. Columns have constant I_{min} values, rows have constant I_{max} values

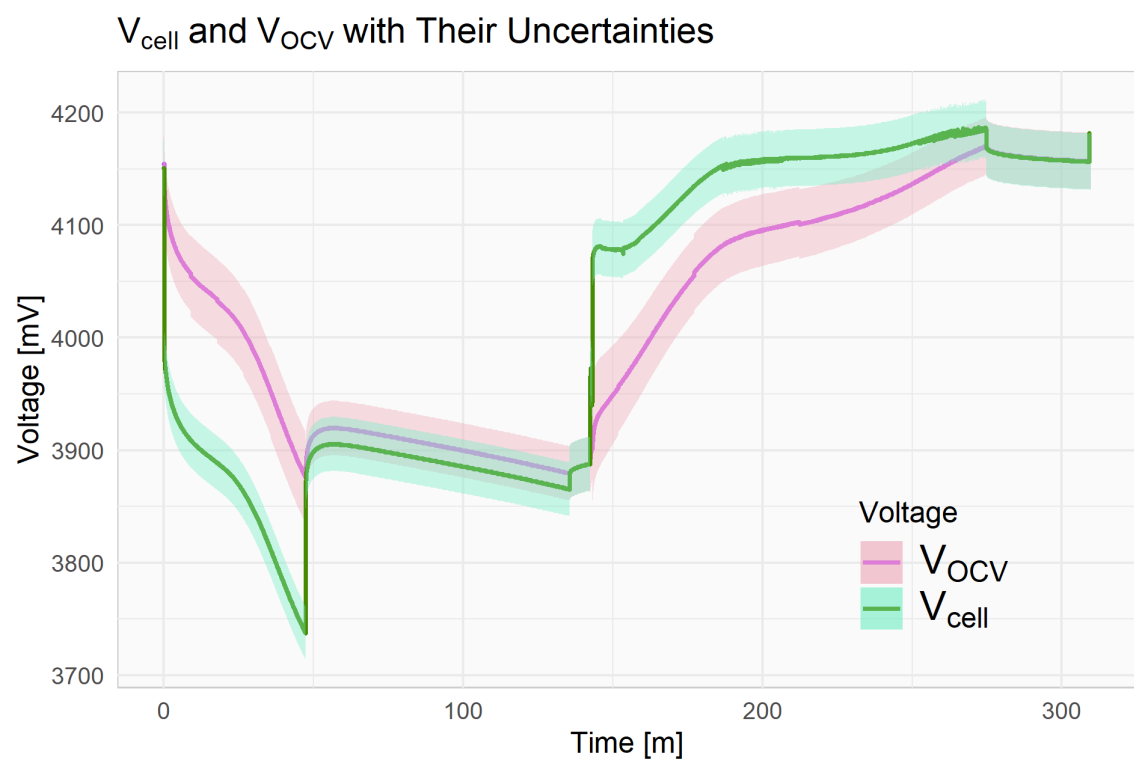


Figure 5.13: V_{cell} and the estimated V_{OCV} with their uncertainties for cell B1 during a test of the balancing system. R_i was calculated with $I_{min} = 100mA$ and $I_{max} = 500mA$.

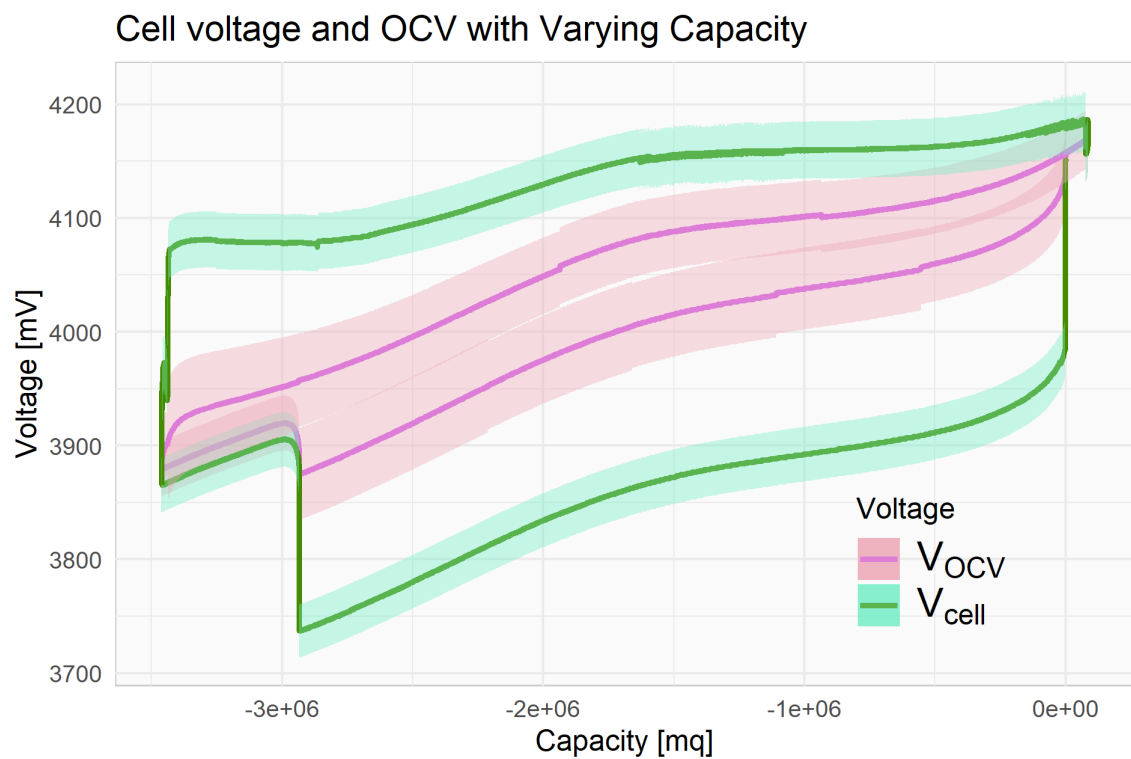


Figure 5.14: The V_{cell} and V_{OCV} response to SoC (capacity) of a cell for the same period as 5.13

5.3.2 The Impact on Balancing Time from Lievre's Method

The balancing algorithm, described in section 4.1, uses the cell voltages generated by Lievre's method to determine how shunting should be applied. The hypothesis and motivation for this is that those voltages better represent the state of the cells than the terminal voltages. To investigate the affect if any, the tests from section 4.3.3 were repeated with identical conditions but using the cell terminal voltages in the algorithm. This resulted in fifteen tests using Lievre's method and fifteen without Lievre's method. For all tests, the procedure, charging current limit, charging voltage limit and cells under test were held constant.

The economics of the application system mean that the minimising charging time is a high priority, as discussed in section 4. The time from charging commencing to completing was measured from each of the tests, figure 5.15 show the density plot of the distributions from the two test sets.

It was assumed that variation in the starting state, temperature and rest period between test setup and test would produce normally distributed random effects in the charging time for each test. The Shapiro–Wilks test is a test of normality was used to verify this assumption. The p-values for the tests were 0.1533 and 0.3177 for the method with Lievre and without Lievre respectively. As these are above the standard alpha value of 0.05, the null hypothesis cannot be rejected, confirming assumption of normality.

The two distributions in figure 5.15 have a difference between their means of 20.3 minutes. Welch's t-test was used to verify this difference, a two-tailed test gave a statistically significant p-value of 0.0034 ($t = 3.28$, $df = 22.5$, $CI = 4.98, 22.1$). Therefore the null hypothesis of equal population means can be rejected, confirming the effect of Lievre's method in the balancing algorithm. These results show a clear improvement with the use of Lievre's method, a 12.6% decrease in charging time.

A plausible alternative cause for the difference in charging time is that in the tests without Lievre's method, the cells received more charge. This can be rejected by calculating the total change in charge, the integral of the currents, for each cell during the tests. Table 5.3 shows the summary statistics for the charging of each cell across the test sets. It also shows that the Shapiro-Wilkes test returned a p-value great enough to accept the normality of the data. Furthermore, Welch's t-test

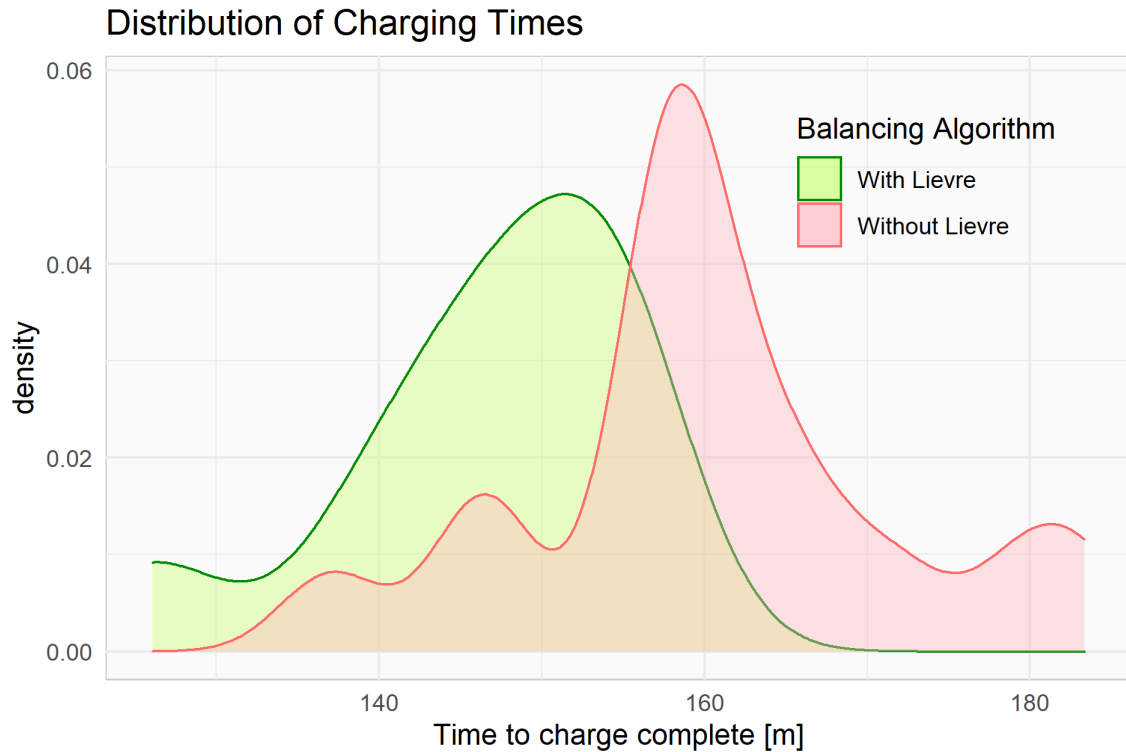


Figure 5.15: Density of charging time when balancing from a relative imbalance of 30% targeting one cell.

	μ	σ	n
With Lievre:	140.1	9.23	15
Without Lievre:	160.4	12.1	15

between the Lievre and non-Lievre sets for each battery show that there is no reason to reject the null hypothesis that the mean charge each cell received was equal across both test sets.

Given the charged capacity is equivalent across all test, but the charging time is different, it follows that the rate of charge must be different between the test sets. This is indeed the case, as shown in table 5.4, the average current with Lievre is higher than without. The value *Ratio* shows the ratio of the average current calculated with *Charge* and *Time* values for each test, compared to the measured average current. The fact that both ratios are close to 1 with standard deviations less than 1% confirms that shorter charging times are the result of higher average currents. The summary statistics in table 5.4 come from individually calculating

Cell	Method	Charge μ [Ah]	Charge σ [Ah]	Shapiro-Wilkes [p]	Welch's [p]
B1	with Lievre	1.06	0.022	0.598	0.330
	without Lievre	1.07	0.027	0.614	
B2	with Lievre	0.82	0.010	0.140	0.634
	without Lievre	0.83	0.019	0.274	
B3	with Lievre	0.82	0.009	0.290	0.499
	without Lievre	0.82	0.018	0.089	
B4	with Lievre	0.82	0.009	0.276	0.901
	without Lievre	0.82	0.019	0.373	

Table 5.3: Maximum change in cell charge during the two charging test sets

Method	Current μ [mA]	Charge μ [mAh]	Time μ [m]	Ratio μ	Ratio σ
With Lievre	-370	0.880	147	-1.03	0.00760
Without Lievre	-331	0.884	160	-0.998	0.00775

Table 5.4: Summary statistics for cell current, charging time and charge for all 30 tests. $Ratio = Current / \frac{Charge}{Time}$ (with corrected units)

the quantities for each cell in every test, and then taking the mean and standard deviation. Note that *Current* is negative to follow active convention, resulting in a negative value for *Ratio*.

The use of Lievre's method in the balancing algorithm changes the voltages compared to determine how shunts should be applied. It is difficult to interrogate exactly how this increased the average current, as the fundamental difference is simply if a shunt is applied. Some insight can be found by examining when the shunts are most likely to be applied in each test group. Figure 5.16 shows the probability density of the activation of shunts during charging for the two test sets. The density describes the chance that for any time picked, at least one shunt is active in any of the tests in the set. This plot shows that using Lievre's method results in shunts being applied earlier in the charging process.

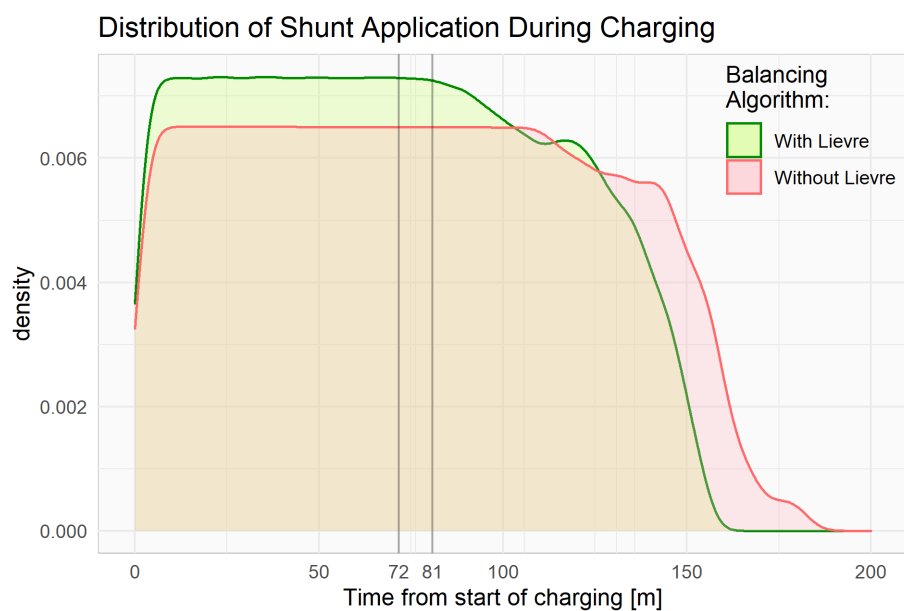


Figure 5.16: Probability density of shunt activation during charging, excluding during the calibration procedure and `termination_balancing`

Method	μ [m]
With Lievre	71.7
Without Lievre	80.8

Chapter 6

Discussion

6.1 System Design and Core Components

6.1.1 Measurement Systems

The measurement systems of the BMS are the foundation for all other functions. The design of the built system has been effective, it fulfilled its role without introducing a barrier for the subsequent systems.

In general, measuring voltages in multicell batteries is a problem with many imperfect solutions, as discussed in section 3.2.2. By its design, the system requires calibration. The only way to avoid such a problem would be by using costly low tolerance resistors. The calibration process is effective, but can also be time consuming. The calibration in this project required a laborious 806 manual measurements. Although, this could be automated with the right equipment.

Unfortunately, this system suffers from a deterioration in resolution as the number of cells increases. The worst resolution occurs for the highest cell from ground, its resolution can be calculated by: $Resolution_{worst} = Resolution_{ADC} \times n_{cells}$. One solution, that would provide a remedy to a degree, would be to implement a higher resolution ADC. While many higher resolution ADCs are available, they come at additional cost.

Another issue introduced by the standard resistors used to build the measurement circuit is a low common mode rejection ratio. In practice, the calibration appears to have satisfactorily increased the CMRR. The variation between the cell

voltage measured with the voltmeter and the ADC were within the normal ranges of fluctuation. Although the CMRR was determined for the uncalibrated system, it could not be determined after calibration without a more precise setup.

The limit for acceptable determination of measurements was not strictly determined during the design. The only limitation was a $\pm 50\text{mV}$ tolerance on cell voltage. In practice, the resulting uncertainties and resolutions have proven sufficient for charging and safety control. Only the balancing system and Lievre's method are noticeably affected by the uncertainty.

The output of Lievre's method, R_s , can be heavily affected by the large relative uncertainties in small changes in current and voltage. Due to this the method discards small current events. Decreasing the uncertainties would allow the method to make use of more, smaller, current events.

As shown through propagation of uncertainty, section 3.4, the relative uncertainty in cell voltages was less than 1%, e.g. $4\text{V} \pm 0.028\text{V}$ for cell B2. Similarly for current measurements above 200mA, the relative uncertainty was less than 1%. As stated before, the final resolutions were between 1.08mV and 4.33mV for voltage and 0.1mA for current.

The measurement with the most significant uncertainty was the cell temperatures, with $\pm 6\text{ }^{\circ}\text{C}$ at room temperature. This level of uncertainty has proven adequate with the cutoff temperature 20 $^{\circ}\text{C}$ above the normal operating temperature of 30 $^{\circ}\text{C}$. If stricter control of the temperature is required, the upper limit can be reduced.

6.1.2 Safety Systems and Charging Control

The safety and charging system performed nominally throughout the testing of the BMS. The choice of finite state machines in the design of charging and fault handling has proven effective. It allows strict and clear control over the response of the BMS.

In one instance, the fault condition could not be handled with the simple FSM logic, and required alteration of the fault condition logic. The situation occurs when the battery is fully discharged, an *under voltage* fault causes the battery to be isolated. Normally this type of situation would cause the MCU to shut down along with all other systems. Additionally, if the MCU was still powered on from external

power, i.e. during a test or if an application required it, the BMS would unisolate the battery after the cool-down period. This would develop because the overpotentials from the discharge current disappear, and the battery voltage increases back above the *under voltage* threshold.

To resolve this edge case, hysteresis was added in the form of a variable *under voltage* threshold. If an *under voltage* fault occurs, the voltage threshold is increased by 500mV. When the fault resolves, the original threshold is restored. This could have been implemented with additional states in the FSM, but the chosen approach proved simpler as it needed to handle only one edge case.

6.2 Balancing System

6.2.1 Comparison to Algorithms in the Literature

In this project, a new balancing algorithm was proposed and verified. As there exists little to no discussion of passive balancing algorithms in the literature much of the analysis techniques had to be constructed.

Practically the only passive balancing algorithm discussed in the literature is a system which only applied balancing shunts during the very final stage of charging [35]. The apparent motivation behind the system is that the charging current during that final stage is close to the current through a shunt, effectively disabling charging for the shunted cells.

The function `unbalancer 4.2` was developed to produce repeatable test conditions. Following work in the literature [35], the premise of the tests was to induce a set imbalance between the cells. The quantity *relative imbalance* 4.1 was developed to standardise this method. Although there are no similar values found in the literature, the quantity is based on previous discussion of cell imbalance being a function of the state of charge and capacities of the cells [3, 5]. Battery imbalance displays itself in the cell voltages, but is explained through the capacity and SoC of the cells. In the tests, the value of cell capacities were initialised at zero for fully charged cells. Therefore, *relative imbalance* represents the empty, or discharged, capacity.

The quantities which gave the most insight into the progress of the balancing system were the *relative imbalance* and the voltage difference (the difference between

the highest and lowest cell voltage). These two quantities are related through the assumption that cell open circuit voltage (OCV) is a function of SoC [3, 11, 12]. It is the *relative imbalance* and cell overpotentials, which are responsible for the voltage differences observed by the balancing algorithm.

The tests and analysis performed in this project were designed to: verify the function of the system across varying imbalance conditions, demonstrate the repeatability of the tests, determine the ability to correctly identify cells requiring shunting, and determine the affects of Lievre's method in the balancing algorithm.

The results in section 4.3.2 demonstrate how the balancing system handles varying levels of imbalance across different cells. The tests confirm that the system is able to restore balance to the battery for all cells. All nine tests in figure 4.7 finish with the voltage difference within the 50mV charging tolerance set by the manufacturer.

Surprisingly, the balancing tests revealed the unexpected behaviour of one cell as the cells were charged. When observing the voltage difference between the cells, the voltage of one cell increased more rapidly than the voltage of others during the final third of the tests, causing a second peak in voltage difference. This is shown clearly in figure 4.7 and 4.11. One seeming explanation would be that this is due to the cell being charged faster. However, this is not the case. The cell is, in fact, being shunted by the balancing system. The charging rate can be eliminated from the analysis by plotting the cell voltages against their capacity, as seen in figure 4.8. To give a clearer view, the cell overpotentials have been excluded from the figure. In this figure, it can be seen that the slope of the line for cell B4 is steeper than all other cells. This could be explained by some internal chemical mechanism, perhaps a different rate of ion diffusion, or that the cell simply has a different SoC ~OCV relationship. Nevertheless, the balancing system consistently handled the deviation.

The repeatability of the balancing system was confirmed by replicating a selection of tests. Ten tests targeting one cell for 30% *relative imbalance* were collected, their voltage difference and *relative imbalance* are displayed in figures 4.11 and 4.12. For all tests the final voltage difference was less than 26mV, even though they started with a range from 75mV to 150mV, as seen in table 4.1. The reason behind the large variation in initial conditions is that it is the *relative imbalance* which is set during setup, and the cell voltage is only indicative of that imbalance. The *relative*

imbalance shows all tests begin with exactly 30% imbalance. Variation can be seen in the plots from only around the 50 minute mark. The time corresponds with a local minimum in voltage difference, at this point the balancing system does not apply any shunts, in turn the *relative imbalance* remains constant, causing the plateau.

The principal behind passive balancing is that cells should be shunted until all cells have the same empty capacity as the cell with the greatest empty capacity [28, 29]. If the exact capacity and SoC of each cell is known, then this becomes trivial, the battery can be balanced by simply applying balancing shunts until the required capacity has been discharged from each cell. For example, using the test procedure in this project and assuming all cells are identical, the amount discharged through the shunts during the test should match the amount discharged through them during the setup period. This would be in the ideal case.

In the current project only the cell voltage and current was known. In order to test how well this system identified the cells that needed balancing and for how much, the charge through the shunt resistors during the setup and test was compared. Specifically, the comparison between the capacity discharged through the shunt resistors per targeted cell as opposed to the capacity discharged through the shunt resistors during the test. An example of these quantities and the formula are shown in figure 4.10 and equation 4.2. In the ideal case demonstrated above, this ratio would be 1.

Table 4.2 shows the ratios for the nine cases of relative imbalance and the cells targeted. The median of this set is 1.04, which suggests that the system only expended 4% more charge than was necessary in the ideal case, this is a very positive result.

6.2.2 Termination Balancing Function

When designing a passive balancing system, the resistance of the shunts is a compromise between the amount of current they can divert and the physical restrictions. With smaller, higher resistance shunts, there is an upper limit to the imbalance the system can rectify before charging is terminated. In the worst case scenario, this can lead to some cells still being overcharged due to the imbalance.

In order to extend effectiveness of the balancing system, a function named

`termination_balancer` was developed. As described in section 4.1.1, if the battery is isolated due to overcharging, it will shunt the highest charged cells. Additionally, once the cool-down period of the safety system has finished, the battery will continue to be charged and balanced as normal. The cycle can repeat many times until the battery is fully charged. An example is shown in figure 4.5.

By all accounts throughout the testing procedures, the system was highly effective and was able to resolve the highest levels of imbalance. This system satisfies the application requirement of fully charging the battery to maximise its energy density. No similar system for passive balancing could be found in the literature.

It can also be noted that although `termination_balancer` is only active during the cool-down period, the length of this period does not have a large affect on its performance. If the imbalance is large enough to not be resolved during the first cool-down period, this will simply lead the system to oscillate between the charging and `termination_balancer`. The net charging current will not change for varying cool-down times. This is comparable to the fact that the frequency of a PWM signal does not change its RMS voltage.

6.3 Lievre's Method

In this project Lievre's method for estimating cell resistance was implemented to improve the performance of the balancing system. It was extended by a system that automatically generates current events if needed. The selection of its internal parameters and its affect on the balancing algorithm were both analysed.

It was found that the use of Lievre's method reduced the charging and balancing time by 12.6%. The methods for measuring and verifying this result are discussed at length in section 5.3.2.

6.3.1 System Performance

Lievre et al. make the assumption that a Lithium-ion battery can be modelled with their equivalent circuit model, and that it can be simplified when only considering a limited sampling time of observations [2]. This assumption is confirmed by the results in figure 5.1. The plot shows that the differential resistance of the cells

measured fall on a straight line with a near perfect fit ($R^2 > 0.9$).

As Lievre et al. show, the sampling time dictates which components of a cell's impedance will be present in the final R_i value [2]. This is illustrated in practice in figures 5.9 and 5.10. The figures demonstrate that for varying sampling time, Δt , the differential resistance will also vary.

As was expected from the initial ECM presented by Lievre et al., the values in figure 5.9 progress with an exponential response. Lievre et al. show, it is the components with a time constant, τ , within the range $\Delta t/3 < \tau < \Delta t \cdot 10$ which will be detected. The time constants of the impedances were calculated and presented in figure 5.10 and table 5.2. The time constants were between 200ms and 750ms. As Lievre et al. showed, these will be detected by a sampling rate of $\min(3\tau) = 600\text{ms}$ and $\max(\tau/10) = 70\text{ms}$. Therefore, the regular sampling rate of 500ms will detect the impedances, but the rapid sampling of 17ms during the calibration sequence will not. Keep in mind that the τ values measured here are subject to change with cell state.

6.3.2 Self Induced Current Events

The system for generating self induced current events was successful, but could be improved in future work. The two limitations of it were the scale of the current events induced when using the balancing shunts, and the sampling period of the measurements.

Firstly, an issue with the use of balancing shunts occurs when the value of I_{min} is close to the current through a balancing shunt. If I_{min} is greater than the shunt current, then no usable observations will be made. If I_{min} is less than the shunt current, then it is possible to use multiple current events to compensate for the heavy weighting on the observations

As discussed before, the short sampling period results in different impedance components being measured during the regular polling cycle. The sampling period was kept to a minimum to reduce the impact on the battery, but this could simply be increased to capture a better picture of the impedances. A sampling period of 100ms would capture impedances with a time constant up to 1 second.

6.3.3 Selection of Weighting Parameters

A key criticism of Lievre's method in section 2.5 is that Lievre et al. do not give justification for their choices of I_{min} and I_{max} [2]. As discussed in section 5.2, the choice Lievre et al. make appear to be the maximum bounds of the values, not necessarily the optimum selection.

In section 5, the uncertainty in the final quantities R_i and V_{OCV} are calculated and presented. Figure 5.11 illustrates how R_i and its uncertainty progress during a charging cycle with varying I_{min} and I_{max} . There appears to be a pattern, where an increase in I_{min} will result in a lowering of the uncertainty, and an increase in I_{max} reduces the sensitivity and update rate of the system.

It appears there is no optimal choice for I_{min} or I_{max} . The selection will be a compromise of tolerable uncertainty and update frequency.

A compromise of $I_{min} = 100mA$ and $I_{max} = 500mA$ was selected in this project. Figure 5.13 compares the cell voltage to the estimated OCV. The clear difference between the two is that the cell voltage has large increases and decreases when the load and charger are connected and disconnected. These larger changes are not present in the OCV, as Lievre's method is used to estimate the changes, or overpotentials, and remove them.

As the purpose of Lievre's method in this project was to remove the overpotentials from cell voltage measurements, this was successful and shown in figure 5.7. The figure demonstrates that when the charger is momentarily disconnected, and the ohmic overpotential disappear, the cell voltage drops to the levels of the OCV.

In figure 5.14, the relationship between cell voltage and SoC can be seen. It confirms the assumption that cell voltage is indicative of SoC, and that the OCV will be a higher quality indicator [15]. If OCV was perfectly modelled, it would have no hysteresis between the discharging and charging paths, i.e. there would be no vertical space between the lines [13, 15].

Chapter 7

Conclusions

The goal of this project was to construct a battery and battery management system for an autonomous robot platform, with a focus on the balancing system algorithm and improving that algorithm through cell modelling.

The system was successfully delivered. In doing so, a low cost cell voltage measurement system was developed and implemented, along with control algorithms for safe fault handling and charging control. The measurement system was shown to be affecting, but having limitations when scaling to larger numbers of cells.

A balancing algorithm was developed by analysing the application's requirements and the behaviour of Lithium-ion batteries with justification from the literature. The algorithm successfully handled all conditions of cell imbalance it was presented with.

The goal of improving the balancing algorithm's ability to determine which cell required balancing, was accomplished with a method provided by the literature [2]. Notably, by employing a modelled cell open circuit voltage in the balancing algorithm, the time for charging and balancing the battery was reduced by 12.6%.

More tests across more diverse conditions of cell depletion and levels of imbalance could be done in the future, to further understand and quantify the positive affect of cell modelling in the balancing algorithm.

References

- [1] M. A. Hannan, M. M. Hoque, A. Hussain, Y. Yusof, and P. J. Ker, “State-of-the-Art and Energy Management System of Lithium-Ion Batteries in Electric Vehicle Applications: Issues and Recommendations,” vol. 6, pp. 19362–19378.
- [2] A. Lievre, A. Sari, P. Venet, A. Hijazi, M. Ouattara-Brigaudet, and S. Pelissier, “Practical Online Estimation of Lithium-Ion Battery Apparent Series Resistance for Mild Hybrid Vehicles,” vol. 65, no. 6, pp. 4505–4511.
- [3] Y. Miao, P. Hynan, A. von Jouanne, and A. Yokochi, “Current Li-Ion Battery Technologies in Electric Vehicles and Opportunities for Advancements,” vol. 12, no. 6, p. 1074.
- [4] J.-M. Tarascon and M. Armand, “Issues and challenges facing rechargeable lithium batteries,” vol. 414, no. 6861, pp. 359–367.
- [5] M. A. Manzo, J. C. Brewer, R. V. Bugga, E. C. Darcy, J. A. Jeevarajan, B. I. McKissock, and P. C. Schmitz, “NASA Aerospace Flight Battery Program,” p. 211.
- [6] C. Liu, Z. G. Neale, and G. Cao, “Understanding electrochemical potentials of cathode materials in rechargeable batteries,” vol. 19, no. 2, pp. 109–123.
- [7] D. Wang, Yun Bao, and Jianjun Shi, “Online Lithium-Ion Battery Internal Resistance Measurement Application in State-of-Charge Estimation Using the Extended Kalman Filter,” vol. 10, no. 9, p. 1284.
- [8] K. S. Ng, C.-S. Moo, Y.-P. Chen, and Y.-C. Hsieh, “Enhanced coulomb counting method for estimating state-of-charge and state-of-health of lithium-ion batteries,” vol. 86, no. 9, pp. 1506–1511.

- [9] R. Surampudi, "NASA Energy Storage Technologies for Future Planetary Science Missions."
- [10] P. A. Cassani and S. S. Williamson, "Significance of Battery Cell Equalization and Monitoring for Practical Commercialization of Plug-In Hybrid Electric Vehicles," in *2009 Twenty-Fourth Annual IEEE Applied Power Electronics Conference and Exposition*, pp. 465–471, IEEE.
- [11] W. Waag, C. Fleischer, and D. U. Sauer, "Critical review of the methods for monitoring of lithium-ion batteries in electric and hybrid vehicles," vol. 258, pp. 321–339.
- [12] W.-Y. Chang, "The State of Charge Estimating Methods for Battery: A Review," vol. 2013, pp. 1–7.
- [13] H. J. Bergveld, W. S. Kruijt, and P. H. L. Notten, *Battery Management Systems*. Springer Netherlands.
- [14] Jong Hoon Kim, Seong Jun Lee, Jae Moon Lee, and Bo Hyung Cho, "A new direct current internal resistance and state of charge relationship for the Li-ion battery pulse power estimation," in *2007 7th International Conference on Power Electronics*, pp. 1173–1178, IEEE.
- [15] S. Abu-Sharkh and D. Doerffel, "Rapid test and non-linear model characterisation of solid-state lithium-ion batteries," vol. 130, no. 1-2, pp. 266–274.
- [16] M. Einhorn, F. V. Conte, C. Kral, and J. Fleig, "Comparison, Selection, and Parameterization of Electrical Battery Models for Automotive Applications," vol. 28, no. 3, pp. 1429–1437.
- [17] H. Zhang, Z. Sun, and W. Gu, "Determination of the SOH estimation indicator and the temperature influence on the Lithium-ion battery in the EV/PHEV applications," in *2015 IEEE International Conference on Mechatronics and Automation (ICMA)*, pp. 464–468, IEEE.
- [18] H. Julien, S. Julien, S. Franck, and A. Philippe, "Development of an Electrochemical Battery Model and Its Parameters Identification Tool."

- [19] H. He, R. Xiong, and J. Fan, “Evaluation of Lithium-Ion Battery Equivalent Circuit Models for State of Charge Estimation by an Experimental Approach,” vol. 4, no. 4, pp. 582–598.
- [20] W. Waag, S. Käbitz, and D. U. Sauer, “Experimental investigation of the lithium-ion battery impedance characteristic at various conditions and aging states and its influence on the application,” vol. 102, pp. 885–897.
- [21] D.-I. Stroe, M. Swierczynski, A.-I. Stroe, and S. Knudsen Kær, “Generalized Characterization Methodology for Performance Modelling of Lithium-Ion Batteries,” vol. 2, no. 4, p. 37.
- [22] X. Wei, B. Zhu, and W. Xu, “Internal Resistance Identification in Vehicle Power Lithium-Ion Battery and Application in Lifetime Evaluation,” in *2009 International Conference on Measuring Technology and Mechatronics Automation*, pp. 388–392, IEEE.
- [23] G. Giordano, V. Klass, M. Behm, G. Lindbergh, and J. Sjoberg, “Model-Based Lithium-Ion Battery Resistance Estimation From Electric Vehicle Operating Data,” vol. 67, no. 5, pp. 3720–3728.
- [24] M. A. Roscher, O. S. Bohlen, and D. U. Sauer, “Reliable State Estimation of Multicell Lithium-Ion Battery Systems,” vol. 26, no. 3, pp. 737–743.
- [25] K. Uddin, S. Perera, W. Widanage, L. Somerville, and J. Marco, “Characterising Lithium-Ion Battery Degradation through the Identification and Tracking of Electrochemical Battery Model Parameters,” vol. 2, no. 2, p. 13.
- [26] A. E. Mejdoubi, H. Gualous, H. Chaoui, and G. Alcicek, “Experimental investigation of calendar aging of lithium-ion batteries for vehicular applications,” in *2017 IV International Electromagnetic Compatibility Conference (EMC Turkiye)*, pp. 1–5, IEEE.
- [27] T. R. Potteiger, K. W. Eure, and D. Levenstein, “Implementation of a Battery Health Monitor and Vertical Lift Aircraft Testbed for the Application of an Electrochemistry-based State of Charge Estimator.”

- [28] A. B. Ahmad, C. A. Ooi, D. Ishak, and J. Teh, “Cell Balancing Topologies in Battery Energy Storage Systems: A Review,” in *10th International Conference on Robotics, Vision, Signal Processing and Power Applications* (M. A. M. Zawawi, S. S. Teoh, N. B. Abdullah, and M. I. S. Mohd Sazali, eds.), vol. 547 of *Lecture Notes in Electrical Engineering*, pp. 159–165, Springer Singapore.
- [29] S. W. Moore and P. J. Schneider, “A Review of Cell Equalization Methods for Lithium Ion and Lithium Polymer Battery Systems,” pp. 2001–01–0959.
- [30] M. Daowd, M. Antoine, N. Omar, P. van den Bossche, and J. van Mierlo, “Single Switched Capacitor Battery Balancing System Enhancements,” vol. 6, no. 4, pp. 2149–2174.
- [31] M. Daowd, N. Omar, P. Van Den Bossche, and J. Van Mierlo, “Passive and active battery balancing comparison based on MATLAB simulation,” in *2011 IEEE Vehicle Power and Propulsion Conference*, pp. 1–7, IEEE.
- [32] “PNGV Battery Test Manual.”
- [33] “MAX11612–MAX11617 Low-Power, 4-/8-/12-Channel, I₂C, 12-Bit ADCs in Ultra-Small Packages.”
- [34] J. R. Taylor, *An Introduction to Error Analysis: The Study of Uncertainties in Physical Measurements*. University Science Books, 2nd ed ed.
- [35] M. Daowd, N. Omar, P. Van Den Bossche, and J. Van Mierlo, “Passive and active battery balancing comparison based on MATLAB simulation,” in *2011 IEEE Vehicle Power and Propulsion Conference*, pp. 1–7, IEEE.
- [36] E. W. Weisstein, “Least Squares Fitting.”
- [37] E. W. Weisstein, “Matrix Inverse.”

Appendix A

3D Least Squares Uncertainties

Propagation of Uncertainty in 3D Least Squares Linear Regression

The least squares linear regression in n dimensions produces a linear model in the form of $n + 1$ parameters. The propagation of uncertainty from the observations to the model parameters requires determining the partial derivatives of the functions which produce the parameters, as shown in equation 3.7.

A least squares model is one where the sum of square of the residuals, the distance between the observations and model, are minimised.

The equations for calculating the parameters in two dimensions can be found in the literature, but not for three dimensions [36].

$$y = a + bx + cz \quad (\text{A.1})$$

$$R^2(a, b, c) = \sum_{i=1}^n [y_i - (a + bx_i + cz_i)]^2 \quad (\text{A.2})$$

Equations A.1 and A.2 show a linear model in 3 dimensions and the sum of squares of that model. Note that y_i , x_i and z_i are observations from a group of n observations. For the sake of readability, from this point on all summations are across all observations, $i \in [1, n]$, and unless otherwise specified, all instances of x , y and z represent the i^{th} observation.

$$\begin{aligned}\frac{\partial}{\partial a} R^2 = 0 &\implies \sum y_i = na + b \sum x_i + c \sum z_i \\ \frac{\partial}{\partial b} R^2 = 0 &\implies \sum x_i y_i = a \sum x_i + b \sum x_i^2 + c \sum x_i z_i \\ \frac{\partial}{\partial c} R^2 = 0 &\implies \sum y_i z_i = \sum z_i + b \sum x_i z_i + c \sum z_i^2\end{aligned}\tag{A.3}$$

The best fit of the model is found by finding the minimum and turning point of R^2 as shown in A.3, and in matrix form in A.4

$$\begin{bmatrix} n & \sum x_i & \sum z \\ \sum x & \sum x^2 & \sum xz \\ \sum z & \sum xz & \sum z^2 \end{bmatrix} \begin{bmatrix} a \\ b \\ c \end{bmatrix} = \begin{bmatrix} \sum y \\ \sum xy \\ \sum zy \end{bmatrix}\tag{A.4}$$

To solve equation A.4 for a , b and c requires the inverse of the (3×3) matrix A , as shown in A.5 [37].

$$\begin{bmatrix} a \\ b \\ c \end{bmatrix} = \begin{bmatrix} n & \sum x_i & \sum z \\ \sum x & \sum x^2 & \sum xz \\ \sum z & \sum xz & \sum z^2 \end{bmatrix}^{-1} \begin{bmatrix} \sum y \\ \sum xy \\ \sum zy \end{bmatrix}\tag{A.5}$$

$$A^{-1} = \begin{bmatrix} n & \sum x_i & \sum z \\ \sum x & \sum x^2 & \sum xz \\ \sum z & \sum xz & \sum z^2 \end{bmatrix}^{-1} = \frac{1}{|A|} \begin{bmatrix} \textcircled{a} & \textcircled{b} & \textcircled{c} \\ \textcircled{d} & \textcircled{e} & \textcircled{f} \\ \textcircled{g} & \textcircled{h} & \textcircled{i} \end{bmatrix}\tag{A.6}$$

$$|A| = \begin{vmatrix} n & \sum x_i & \sum z \\ \sum x & \sum x^2 & \sum xz \\ \sum z & \sum xz & \sum z^2 \end{vmatrix} = \begin{aligned} &n \sum x^2 \sum z^2 - n(\sum xz)^2 - (\sum x)^2 \sum z^2 \\ &+ 2 \sum x \sum xz \sum z + \sum x^2 (\sum z)^2\end{aligned}\tag{A.7}$$

Where the components $\textcircled{a} \rightarrow \textcircled{i}$ in equation A.6 are shown in equations A.8, and the determinant is shown in equation A.7.

$$\begin{aligned}
\textcircled{a} &= \sum x^2 \sum z^2 - (\sum xz)^2 & \textcircled{b} &= \sum z \sum xz - \sum x \sum z^2 \\
\textcircled{c} &= \sum x \sum xz - \sum z \sum x^2 & \textcircled{d} &= \sum xz \sum z - \sum x \sum z^2 \\
\textcircled{e} &= n \sum z^2 - (\sum z)^2 & \textcircled{f} &= \sum z \sum x - n \sum xz \\
\textcircled{g} &= \sum x \sum xz - \sum x^2 \sum z & \textcircled{h} &= \sum x \sum z - n \sum xz \\
\textcircled{i} &= n \sum x^2 - (\sum x)^2
\end{aligned} \tag{A.8}$$

This gives the final equations for a , b and c shown in A.9

$$\begin{aligned}
a &= \frac{\textcircled{a} \sum y + \textcircled{b} \sum xy + \textcircled{c} \sum yz}{|A|} \\
b &= \frac{\textcircled{d} \sum y + \textcircled{e} \sum xy + \textcircled{f} \sum yz}{|A|} \\
c &= \frac{\textcircled{g} \sum y + \textcircled{h} \sum xy + \textcircled{i} \sum yz}{|A|}
\end{aligned} \tag{A.9}$$

To calculate the uncertainty requires the partial derivatives of a , b and c with respect to each of the observations x_j , y_j and z_j , where $j \in [1, n]$. The large number of terms in each equation means differentiation by hand will be tedious and prone to errors. To expedite the process, a program to perform the algebraic manipulations on the equations was written.

The system operated on strings representing the equation and was given a library of derivatives of terms with respect to variables, as shown in A.10. The operations were separated into five functions: tokenization, quotient rule, product rule, chain rule and differentiator.

$$\begin{aligned}
\frac{\partial}{\partial x_j} \sum x &\mapsto 1 & \frac{\partial}{\partial x_j} \sum x^2 &\mapsto 2x_j \\
\frac{\partial}{\partial x_j} \sum xy &\mapsto y_j & \frac{\partial}{\partial x_j} \sum xz &\mapsto z_j
\end{aligned} \tag{A.10}$$

The tokenizer separated equations into multiplied terms, addition and subtraction operators, as in A.11.

$$\sum x \sum y - \sum z \mapsto \left\{ +, \sum x \sum y, -, \sum z \right\} \quad (\text{A.11})$$

Each term was further separated into sub-terms, as in [A.12](#).

$$\sum x \sum y \mapsto \left\{ \sum x, \sum y \right\} \quad (\text{A.12})$$

Once a term was separated, if it contained more than one instance of the variable of interest it was given to the product rule function, otherwise it was given straight to the chain rule function. With the least square equations, the chain rule function is specifically for the case of summations squared. It calls the differentiator to find the derivative of the summation and returns the full derivative according to the chain rule, shown with respect to x_j in [A.13](#)

$$\left(\sum xy \right)^2 \mapsto 2y_i \sum x \quad (\text{A.13})$$

The product rule function replaced sub-terms containing the variable of interest with the product rule equivalent, shown with respect to x_j in [A.14](#), finding the derivatives using the chain rule function.

$$n \sum z \sum x \sum xy \mapsto n \sum z \left(\sum xy + y_i \sum x \right) \quad (\text{A.14})$$

To simplify handling of equations, a , b and c were separated into their numerator and the common $|A|$ denominator. The quotient rule function takes the derivatives according the the previous functions and assembles with the original equations according to the quotient rule, shown with respect to x_j in [A.15](#)

$$\frac{n \sum z \sum xy}{\sum x} \mapsto \frac{ny_i \sum z \sum x - n \sum z \sum xy}{(\sum x)^2} \quad (\text{A.15})$$

Once the final equation for the partial derivative has been calculated, it is passed to the the system parser and evaluated for each of the $3n$ observations. According to equation [3.7](#), the vectors of observation uncertainties $\{\delta x_1, \delta y_1, \delta z_1, \dots, \delta x_n, \delta y_n, \delta z_n\}$ were element wise multiplied with the corresponding partial derivative, squared and summed to find the absolute uncertainty in the parameter

The final nine partial derivatives, with three parameters (a , b and c) differentiated across three dimensions (x , y and z), comprised of up to 84 sub-terms each.

Appendix B

System Schematic

A

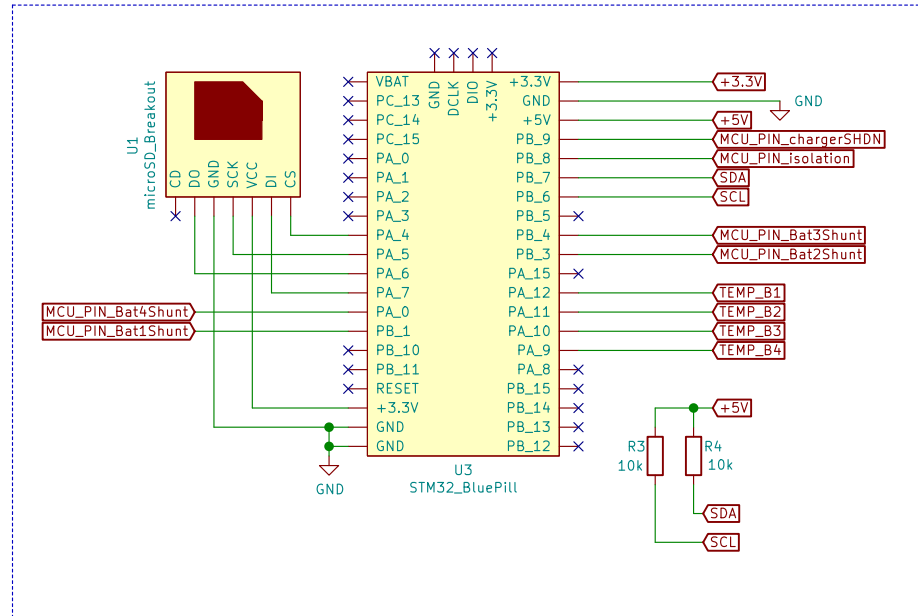
A

B

B

C

C



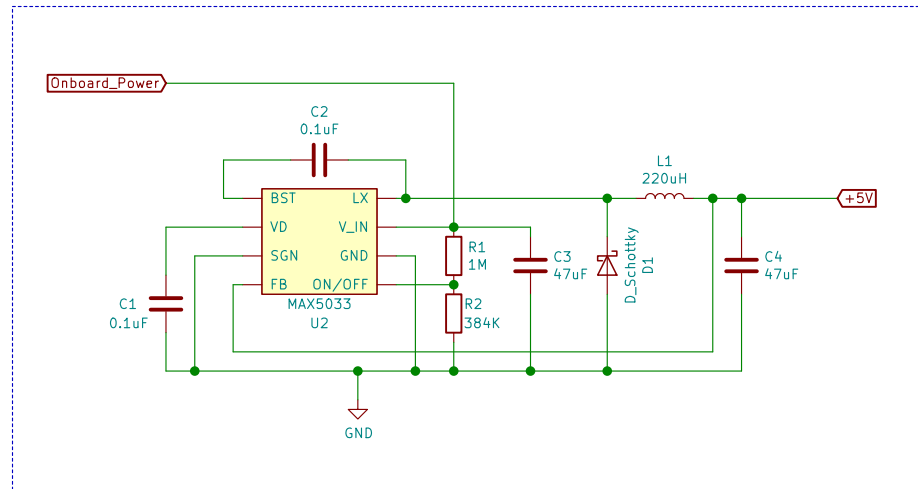
Microcontroller and SD Card

D

D

E

E



Onboard Power

Sheet: /BMS diagram – MCU and Onboard Power/
File: BMS diagram – MCU and Onboard Power.sch

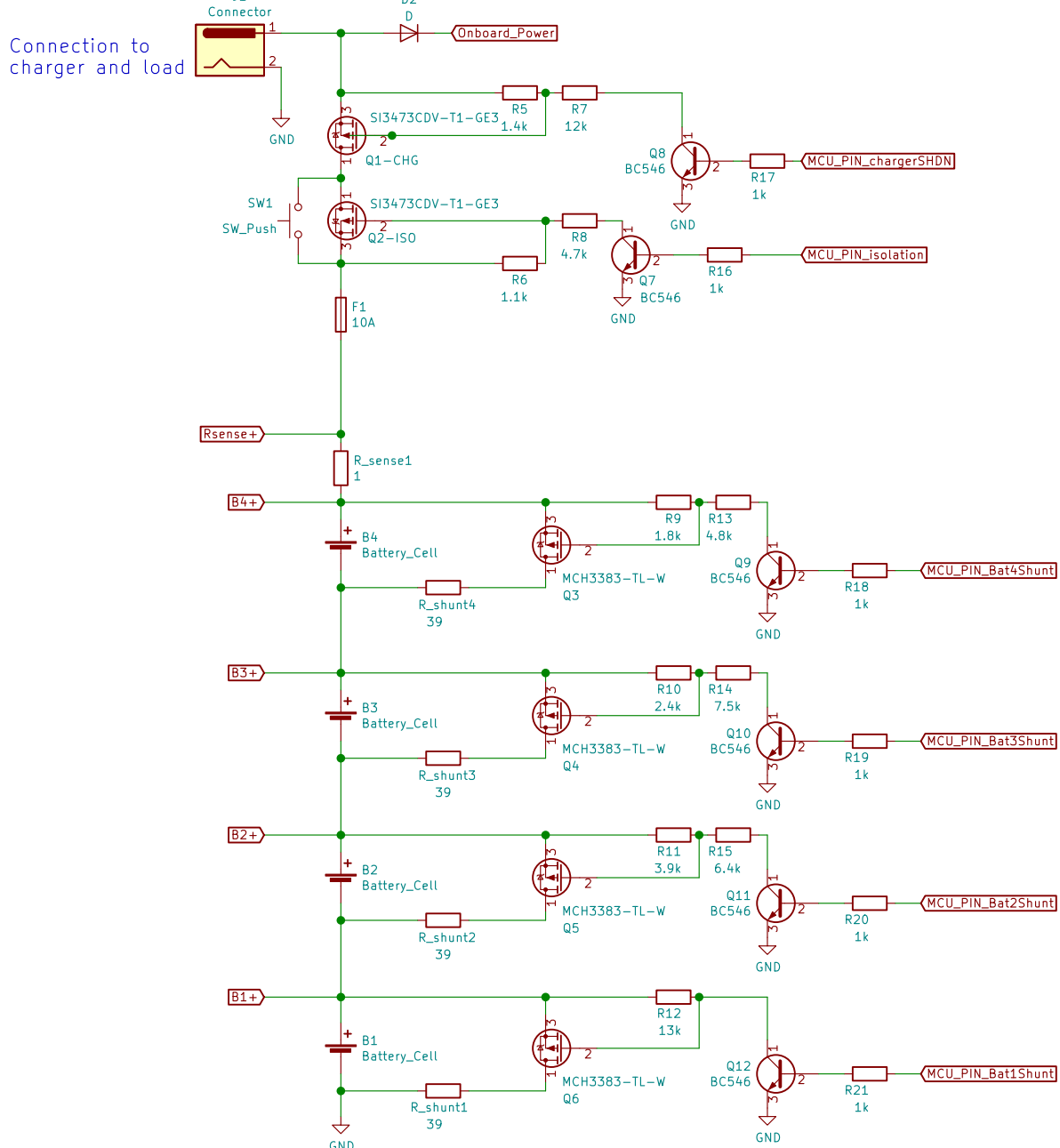
Title: BMS – MCU and Onboard Power

Size: A4	Date:
KiCad E.D.A. eeschema (5.1.5)-3	Rev:

Id: 2/5

A

A

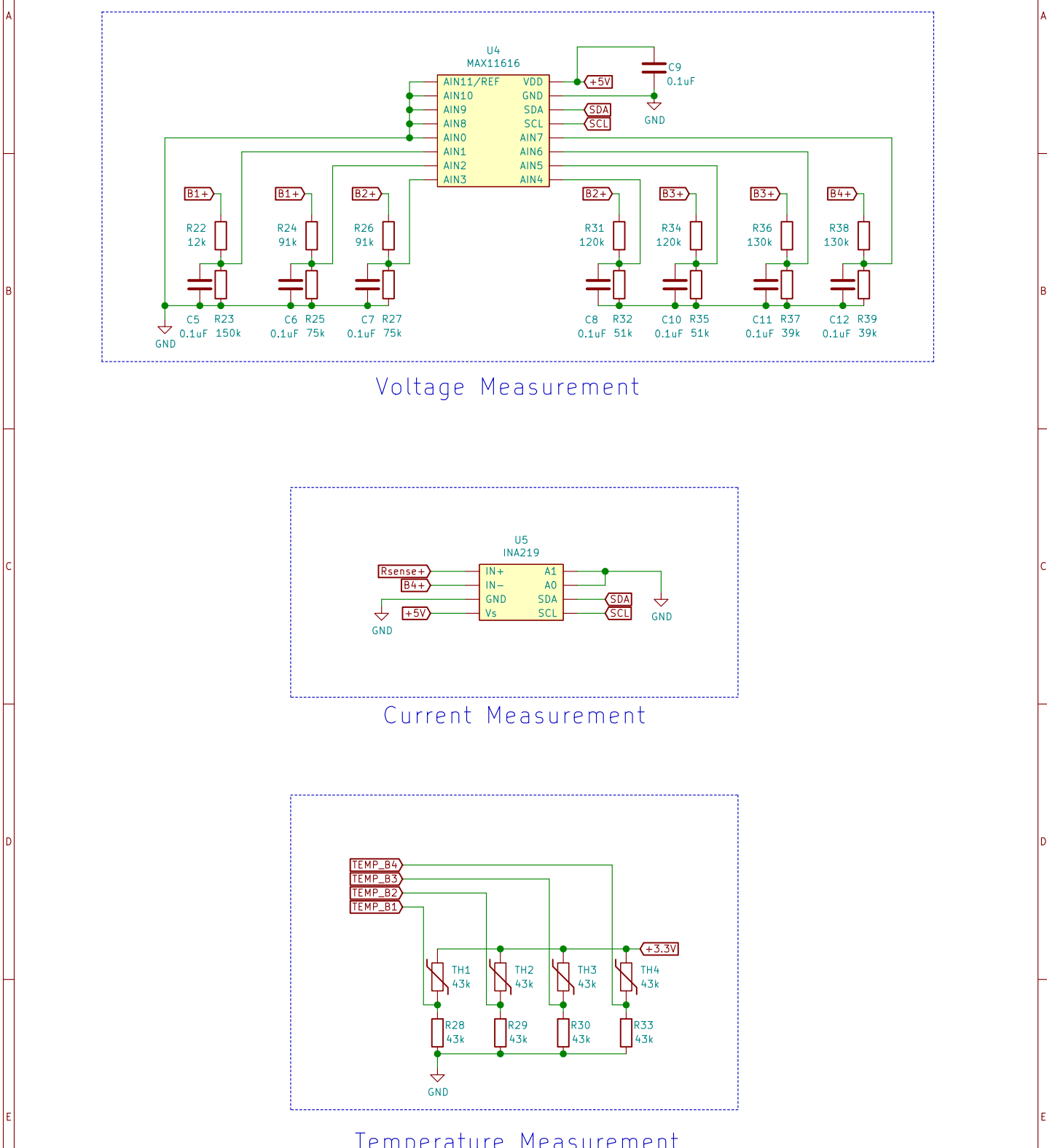


Sheet: /BMS diagram – Cells, Shunts and Isolation/
File: BMS diagram – Cells, Shunts and Isolation.sch

Title: BMS – Cells, Balancing Shunts, Charging and Isolation

Size: A4 Date:
KiCad E.D.A. eeschema (5.1.5)-3

Rev:
Id: 3/5



Sheet: /BMS diagram – Measurement/
File: BMS diagram – Measurement.sch

Title: BMS – Voltage, Current and Temperature Measurement

Size: A4 Date:
KiCad E.D.A. eeschema (5.1.5)-3

Rev:
Id: 4/5